UNIVERSIDADE DE LISBOA
FACULDADE DE CIÊNCIAS
DEPARTAMENTO DE FÍSICA

Determination of $^{118}Sn(p,\gamma)^{119}Sb$ cross-section at astrophysical energies from X-ray emission yields

Manuel António Tavares Xarepe

Mestrado Integrado em Engenharia Física

Dissertação orientada por:
Prof. Dr. Jorge Miguel de Brito Almeida Sampaio
Prof. Dr. Daniel Galaviz Redondo

2020

Acknowledgments

I would like to start by expressing my deepest gratitude and appreciation to my advisors, Jorge Sampaio and Daniel Galaviz, for accepting me as their student and for their support and guidance during this dissertation. The countless meetings and discussions we had were crucial for the elaboration of this thesis

Secondly, I would also like to thank my research group, NUC-RIA, for stimulating my interest in the field and providing very useful feedback and company in these last few months.

During these past five years at FCUL, I met incredible people and I am lucky to call some of them friends. A special thank you to ”Luz I Ta’nos”, Pedro Gabriel and Tomás Sousa, for their friendship and academic support over the years. I was also part of NFEF-FCUL, where I had the opportunity of working with wonderful people on projects of which I am very proud.

Finally, I would like to thank my family, especially my grandmother, Fátima, and my girlfriend, Leonor, for supporting me throughout all these years.

Last but not least, to FCUL, which provided me with many tools, not only professionally but also personally and has been more than a home in the last five years.

Resumo

Neste trabalho é determinada, experimentalmente, a secção eficaz da reação ^{118}Sn(p,γ)^{119}Sb através do Método da Ativação. Neste método são, normalmente, medidos os espetros de emissão-γ do declínio radioativo do produto da reação, determinando-se a partir da intensidade dos picos a sua atividade. Estes, por sua vez, relacionam-se diretamente com a secção eficaz. No entanto, nem sempre é possível aplicar este método, uma vez que alguns produtos de reação decaem, por captura eletrónica, diretamente para o estado fundamental do isótopo descendente, sem nenhuma emissão-γ associada ou então decaem para estados nucleares excitados com baixa probabilidade de emissão. Para estes casos foi proposto, recentemente, a medição de emissão de raios-X resultante da desexcitação atómica associada ao processo de captura eletrónica (que cria uma lacuna nas camadas atómicas internas). O objetivo principal deste trabalho é validar o Método de Ativação com base na análise da espetrometria de raios-X.

O produto de reação, o isótopo ^{119}Sb, tem a propriedade de decair por captura eletrónica, dando origem à emissão-γ de $\sim$23.9 keV e emissões de riscas Kα e Kβ com energias de $\sim$25.1 keV e $\sim$28.4 keV, respetivamente. Isto permite obter simultaneamente os espetros de emissão-γ e das riscas atómicas K com detetores calibrados para a mesma região de energias. Assim, comparando a secção eficaz obtida pela medição das intensidades dos picos de emissão-γ e das riscas K, podemos validar ou não o método.

Tendo este objetivo em mente, o trabalho foi dividido em quatro etapas: a produção e caracterização de um alvo de estanho natural, a ativação dos alvos com um feixe protões, a aquisição dos espetros do decaimento radioativo dos alvos, e a análise dos dados.

Na primeira etapa foram produzidos varios alvos de estanho natural utilizando a técnica de evaporação em vácuo, no laboratório NUC-RIA do LIP, situado na FCUL. Este estudo foi de grande importância, pois foi a primeira vez que foram produzidos alvos de estanho neste laboratório e era necessário validar a metodologia, de forma a garantir a produção futura de alvos altamente enriquecidos com ^{118}Sn. Alvos finos (com aproximadamente 45 μg/cm^2) foram evaporados sobre um suporte de alumínio e alvos mais grossos (com aproximadamente 432 μg/cm^2) sobre um suporte de cobre. Ao variar a quantidade de estanho no "barco" da evaporadora era possível controlar a espessura. Os resultados são promissores, uma vez que foi possivel produzir alvos homogéneos de varias espesssuras.

Os alvos foram caracterizados através de duas técnicas distintas: a medição da perda de energia de partículas-α ao atravessarem o alvo e a retrodispersão de Rutherford (RBS) de protões. Os espetros de perda de energia das partículas-α foram medidos numa câmara de vácuo associada a um detetor PIPS, existente no laboratório de Física Nuclear da FCUL. Os resultados obtidos mostram que o sistema permite medir a espessura de alvos finos, mas as incertezas associadas são demasiado elevadas. De facto, os valores obtidos são da mesma ordem de grandeza dos obtidos por RBS, utilizando o Van de Graaff do Laboratório de Aceleradores e Tecnologias de Radiação (LATR) do CTN/IST.

Na segunda etapa, os alvos foram depois activados usando o Tandem de 3 MV do LATR. O alvo no suporte de alumínio foi activado com um feixe de protões com energia nominal de $E_p = 3.66$ MeV e o alvo no suporte de cobre foi activado com um feixe de protões com energia nominal de $E_p = 3.29$ MeV. Em ambos os casos a ativação foi bem sucedida: o feixe manteve-se estável durante cerca de 11 horas e a espessura do alvo constante. Em ambas as irradiações adquiriram-se espetros de RBS utilizando dois detetores PIPS existentes na câmara de irradiação.

Na terceira etapa procedeu-se à aquisição dos espetros recorrendo a dois detetores SDD, comumente utilizados na espetroscopia por fluorescência de raios-X. Os alvos foram transportados do CTN para a estação de medição na FCUL e procedeu-se à aquisição dos espetros em intervalos de 30 minutos, durante 10 dias. O processo de aquisição de dados foi totalmente automatizado.

Na quarta etapa começou-se por fazer uma caracterização da função de resposta dos detetores SDD. Para isso determinou-se a resolução em função da energia dos dois detetores utilizados nas aquisições e implementaram-se simulações de Monte Carlo para determinar as respetivas eficiências. Estas simulações tiveram em conta as características físicas dos vários componentes dos detetores (dimensões e materiais) bem como da fonte: primeiro fontes pontuais e depois fontes extensas num suporte, representativas dos alvos ativados. Os espetros de contagens acumuladas em função do tempo foram corrigidos, com as funções de resposta simuladas, de modo a obtermos a intensidades dos picos de emissão.

Uma grande desvantagem da utilização de emissões de raios-X no método de ativação é que estes são característicos do átomo. Assim, um alvo de estanho natural consiste em vários isótopos estáveis deste elemento, que dão origem a diferentes produtos com as mesmas emissões de raios-X característicos. No entanto, se os limiares de reação para os diferentes isótopos ou se os tempos de semi-vida dos produtos radioactivos forem suficientemente diferentes, é possível distinguir o contributo de cada uma delas.

Depois de feita alguma análise, concluiu-se que para estanho natural a única componente não desejada seria a contribuição do decaimento de ^{117}Sb que, por ter um tempo de semi-vida bastante diferente do decaimento de ^{119}Sb, é possível corrigir. Após remover a contribuição do decaimento de ^{117}Sb calcularam-se as razões de intensidades Kα/Kβ e Kα/γ, que foram comparadas com os valores tabelados na literatura. Relativamente à razão Kα/γ, obtiveram-se os valores de 3.6 ± 0.3 para ambas as ativações, o que está de acordo com o valor tabelado de 3.6 ± 0.1.

As secções eficazes foram determinadas através do método absoluto e do método relativo. No método absoluto consideram-se os valores medidos experimentalmente do fluxo de protões incidentes, da densidade superficial do alvo, e da intensidade dos picos de emissão. No método relativo eliminou-se a dependência no fluxo dos protões incidentes e na densidade superficial do alvo, utilizando as contagens de protões obtidas a partir dos espetros de RBS adquiridos durante as irradiações.

Para a reação ^{118}Sn(p,γ)^{119}Sb obtivemos, pelo método absoluto, os valores de 1.6 ± 0.3 mbarn para a ativação de $E_p = 3.66$ e de 0.27 ± 0.01 mbarn para a ativação de $E_p = 3.29$ MeV. Os resultados obtidos, a partir da análise dos picos de emissão-γ e das riscas Kα, são idênticos dentro da barra de incerteza. No método relativo, para a energia de $E_p = 3.66$ MeV, obtivemos os valores de 1.3 ± 0.1 mbarn, a partir do pico de emissão-γ e de 1.31 ± 0.08 mbarn, a partir das riscas Kα. Para a energia de $E_p = 3.29$ MeV, os valores obtidos foram de 0.27 ± 0.02 mbarn para o pico de emissão-γ e idêntico, dentro da incerteza, para o cálculo utilizando a risca Kα.

A consistência entre os valores obtidos mostra que, mesmo utilizando estanho natural, o Método de Ativação pode ser aplicado medindo o espetro de raios-X. No entanto, para a energia de $E_p = 3.66$ MeV, obteve-se uma diferença significativa das secções eficazes determinadas pelos dois métodos. Esta diferença pode ser justificada pelo cancelamento das dependências no fluxo incidente de protões e na espessura dos alvos quando se aplica o método relativo. Esses dois parâmetros foram particularmente afetados pelas incertezas de medição a esta energia. Este resultado mostra que o método relativo é mais robusto a erros nas medições do fluxo incidente e da espessura dos alvos, resultando em menores incertezas do que o método absoluto. Os métodos absoluto e relativo não são exclusivos, pois é possível aplicar os dois métodos na mesma irradiação, desde que os espetros de RBS sejam adquiridos.

No nosso estudo também analisámos a reação ^{116}Sn(p,γ)^{117}Sb que ocorre na irradiação do estanho natural às energias utilizadas. Ao contrário da reação ^{118}Sn(p,γ)^{119}Sb, a secção eficaz desta reação já foi medida anteriormente, o que nos permitiu validar as nossas medidas e análise dos dados. De facto, a secção eficaz desta reação obtida pelo método relativo a $E_p = 3.66$ MeV, é de 0.7 ± 0.1 mbarn, o que está em muito bom acordo com os valores obtidos por N. Özkan et al em 2002 e Famiano et al. em 2008.

Dando continuação a este trabalho, propomos que as próximas etapas a realizar sejam o estudo da

ativação com um alvo altamente enriquecido em ^{118}Sn. Neste estudo, várias outras melhorias deverão ser consideradas, nomeadamente, correções no detector colocado no interior da câmara que mede o fluxo de protões incidentes, a produção de um suporte para o alvo activado durante a aquisição e melhoraramentos no sistema de medição de espessura por perda de energia no alvo. A ativação do alvo deve também ser realizada para mais pontos de energia, a fim de extrair a dependência energética da secção eficaz e consequentemente do fator-S astrofísico.

Palavras-chave: Método de activação, Espetroscopia de raio-X, Espetroscopia de retrodispersão de rutherford, Simulações de Monte Carlo, Reação de captura radiativa

Abstract

The stellar synthesis of elements heavier than Fe is explained by slow (s) and rapid (r) neutron capture processes, involving explosive events (e.g. supernovae and kilonovae). However, about 35 proton-rich naturally occurring isotopes between Se and Hg cannot be produced by neutron capture processes. The reaction network for the production of the so-called p-nuclei combines (γ, n) and (p, γ) reactions on preexisting s- and r-process seed nuclei.

In this work, the Activation Method is used to measure for the first time the cross-section of the radiative proton capture reaction ^{118}Sn(p,γ)^{119}Sb. The γ-emission associated to the electron capture to the excited state of ^{119}Sb will be used to validate the method.

To do this, several targets of natural tin of various thicknesses were produced using different backings. This targets were characterized using two different methods, Rutherford Backscattering Spectrometry (RBS) and Energy-Loss Transmission method. Two of the characterized tin targets were then activated using different proton beam energies (3.66 MeV and 3.29 MeV).

The decay acquisition was done at FCUL using two SDD detectors, placed in close geometry. The response functions of the detectors were fully characterized by means of Monte Carlo simulations, and the data acquisition and analysis was fully automatized. The detector response was also simulated using as input the emission spectrum of the Sn K-lines from MCDF method calculations.

The contribution of ^{117}Sb, produced in the proton capture reaction on ^{116}Sn, was deconvoluted from the reaction of interest in the accumulated spectra. The ^{117}Sb decay was the only contribution from other isotopes that was not negligible. This resulted in Kα/γ intensity ratios from the decay in agreement with the literature value.

The cross-sections for both ^{118}Sn$(p, \gamma)^{119}$Sb and ^{116}Sn$(p, \gamma)^{117}$Sb reactions were calculated using two methods: the absolute method and the relative method. In the absolute method, it is necessary to know precisely the incident proton flux and the target thickness, while in the relative method, the number of backscattered protons was measured, eliminating the dependence on these two parameters.

In both methods, the difference between the cross-sections obtained using the Kα-line and the γ-emission yields was negligible. Concluding this way that it is valid to use X-ray yields to calculate the ^{118}Sn$(p, \gamma)^{119}$Sb. However, there is a difference of about 16-18 % between the calculated values with absolute and relative methods at 3.66 MeV. This difference can be justified by the fact that the relative method cancels out any dependencies in the incident proton flux and thickness.

The cross-section values obtained using either method are in the same order of magnitude as the ones given by TALYS code calculations, and the ^{116}Sn$(p, \gamma)^{117}$Sb reaction cross-sections are in good agreement with the experimental values obtained by N. Özkan et al. in 2002 and M. Famiano et al. in 2008. These results imply that even using a natural tin target, the calculated cross-section values for the ^{118}Sn$(p, \gamma)^{119}$Sb reaction are close to the real values.

All these results are of extreme importance as they showed that it will be possible to produce and activate a highly enriched target of ^{118}Sn to calculate the Cross-section.

Keywords: Activation method, X-ray spectroscopy, Rutherford backscattering spectrometry, Monte Carlo simulation, Radiative capture reactions

Contents

List of Tables

List of Figures

List of symbols

d - Source-detector distance

$\frac{dN_D}{dt}$ - Decay Rate of N_D

$\left(\frac{d\sigma}{d\Omega}\right)_{Ruth}$ - Differential cross-section for Rutherford backscattering

$\left(\frac{d\sigma}{d\Omega}\right)_{scat}$ - Differential cross-section of a scattering reaction

e - elementary charge

F - Fano factor

N_A - surface density of an isotope A

N_D- Number of Produced nuclei

N_D^{irr} - Total number of existing radioactive nuclei

N_D^{max} - saturation value of produced nucleus

N_{decay} - Total number of decays

$N_{detected}$ - Number of events counted by the detector

$N_{emitted}$ - Number of particles emitted by the source

N_p^i - Total number of protons scattered

N_{peak}^{part} - Peak area of the relevant decay particle

$M(X)$ - Nuclear mass of X

Q - Reaction Q value

r - Radius of the detector active area

R- detector Resolution

R_c - Reaction generation rate

$r(\theta, \phi)$ - Coefficient of moment.

S/ρ - mass stopping power

t_{acqui} - Acquisition time

t_i - RBS acquisition time interval

t_{irr} - Irradiation time

t_{transp}- Transportation time

$t_{1/2}$ - Radioactive nucleus half-life

z - Atomic mass of the backscattered particle

Z_A - Atomic mass of the target

λ - Decay constant of the radioactive nucleus

ΔE - Transmission energy loss

Δx_X - thickness of X in nm

ϵ - energy needed to create an electron-hole in a material

ϵ_D - Detector efficiency

ϵ_g - Detector geometrical efficiency

ϵ_i - Detector intrinsic efficiency

$\epsilon_{\mathrm{K}\alpha}$ - Detector efficiency at the Kα energy

$\epsilon_{\mathrm{K}\beta}$ - Detector efficiency at the Kβ energy

ϵ_p - PIPS detectors' efficiency

ϵ_0 - Vaccum permittivity

ϵ_γ - Detector efficiency at the γ energy

η - Relative intensity of the decay particle emission

θ - center-of-mass angle at which the particles are scattered

$\theta_l ab$ - laboratory angle at which the particles are scattered

ρ - Element density

$\rho \Delta x_X$ - thickness of X in μg/cm^2

σ - Reaction cross-section

σ_{det} - Standard deviation

σ_{noise} - electronic noise contribution to σ_{det}

ϕ_b - Incident particle flux

Acronyms

B^2FH - synthesis of the elements in Stars by E. Margaret Burbidge et al.

CTN/IST - Campus Tecnológico e Nuclear do Instituto Superior Técnico

CAD - Computer-aided Design

DPPMCA - Digital Pulse Processor Multi-Channel Analyser

FCUL - Faculdade de Ciências da Universidade de Lisboa

FWHM - Full Width at Half Maximum

HPGe - High-Purity Germanium

IBA - Ion Beam Analysis

ITN - Instituto Tecnológico e Nuclear

LATR - Laboratory of Accelerators and Radiation Technologie

LIP - Laboratório de Instrumentação e Física Experimental de Partículas

MCDF - multi-configuration Dirac-Fock

MCDFGME - Multi-configuration Dirac-Fock and general matrix elements

NUC-RIA - Nuclear Reaction Instrumentation and astrophysics

NRA - Nuclear Reactions Analysis

PIPS - Passivated Implanted Planar Silicon

PIXE - Proton Induced X-ray Emission

QED - Quantum electrodynamics

RBS - Rutherford Backscattering Spectroscopy

RIB - Radioactive Ion Beam

SDD - Silicon Drift Detector

Chapter 1

Introduction

The abundance of elements in the Universe is a rather well-understood topic, however, significant uncertainties still exist. Stellar nucleosynthesis is a theory that has evolved over the years [1], and tries to explain the processes behind nuclei production. Light elements from H to Li are produced in the Big-Bang. Heavier elements, up to Fe are produced in chains of nuclear reactions inside massive stars in a sequence of burning stages, starting with the H fusion and ending in the Si-burning stage. The synthesis of elements heavier than Fe requires neutron-rich environments, where slow and rapid neutron captures processes (known, respectively, as the *s*- and *r*-process) can occur. These two processes can explain the existence and abundance of most of the nuclei heavier than iron. However, about 30 to 35 proton-rich naturally occurring isotopes between Se and Hg cannot be produced via β^- decay, which means they cannot be produced via neutron capture processes.

1.1 p-Process nucleosynthesis

In 1957, it was proposed by Cameron [2] and by Burbidge *et al.* in the famous B^{2}FH paper [3] that these nuclei are produced in the hydrogen layers of core-collapse Type-II supernovae. More recently, the production of these isotopes has been described in the Ne-O layers of Type-II SNa [4] or in Type-Ia SNA [5]. There, a combination of photodisintegration (γ, n) and proton capture (p, γ) reactions on preexisting neutron-rich s-process seed nuclei can produce a set of nuclei that are shielded from the production by neutron capture (see figure 1.1 on the right). Because of the dominant role played by proton reactions, B^{2}FH named these p-process nuclei. Figure 1.1 on the left gives the decomposition of the solar abundances of heavy nuclides into *s*-, *r*-, and p-process contributions.

One of the main uncertainties of nucleosynthesis based on p-processes is associated with the origin of the light Mo, Ru, In, and Sn p-nuclei, as they have an abundance much larger than expected in the framework of the standard p-processes. Processes such as the rapid proton capture rp-process [6] and the antineutrino capture on free protons νp-process have been proposed to explain the missing elements. The rp-process is a reaction network of successive proton captures on seed nuclei that drives the nuclei near the proton-drip line before β^+ decays can occur. The evolution of the network is limited by the competing α-decay processes that remove protons from nuclei. The νp-process [7] considers the antineutrino capture on the free protons to produce neutrons that are immediately captured by neutron-deficient nuclei. This allows to overcome the β^--decay bottlenecks in the *r*-process in type-II supernova nucleosynthesis, producing heavier seed nuclei for the synthesis of nuclei with mass numbers $A > 64$.

However, until now, there are no direct or indirect observations that elements beyond Fe are produced in type-II supernovae. Moreover, despite several decades of stellar core-collapse modeling, simulations

fail to produce the expected abundances of these elements in a consistent way. Recently, it has become more evident that one of the most likely scenarios for the formation of (part of) elements beyond Fe is in the ejected material after a neutron star merger – the so-called kilonova nucleosynthesis [8].

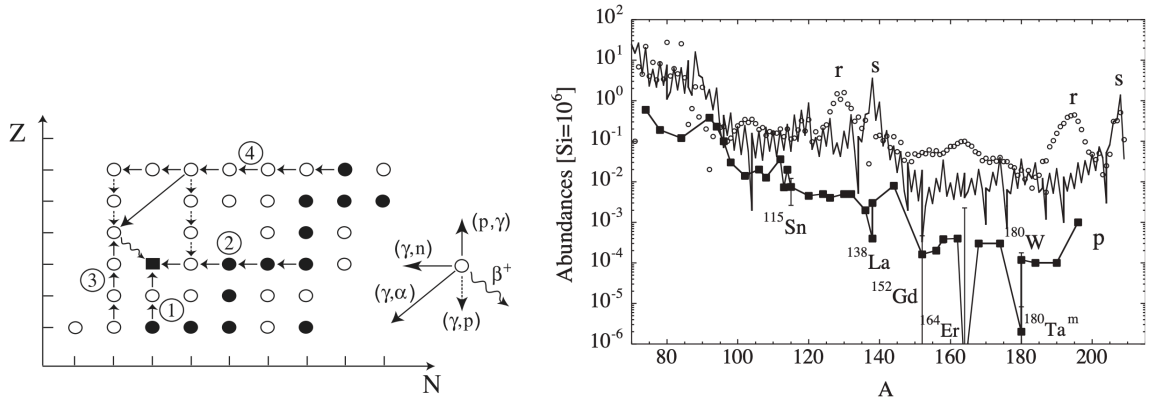

Figure 1.1: Left: Schematic representation of some simple possible nuclear routes through which seed *s*-nuclide or *r*-nuclide (black dots) can be transformed into a p-nuclide (black square). Unstable nuclei are represented by open dots. Right: Decomposition of the solar abundances of heavy nuclides into s-process (solid line), *r*-process (open circles) and p-process (squares) contributions. The uncertainties on the abundances of some nuclides due to a possible *s*-process contamination are represented by vertical bar. Image taken from [4].

Predicting stellar abundances depends upon complex reaction network calculations within a given astrophysical environment that may involve 10^5 reactions on 2000 stable and unstable nuclei [9]. In view of the huge number of reactions, p-process studies will always have to rely on reaction cross-sections obtained with theoretical models. In figure 1.2, we have an example of the reaction flux generated by a type-II supernova. Every line needs to be accounted for in the simulations if we want to predict the abundance of nuclei produced in this type of explosions. Nevertheless, it is of utmost importance to base these calculations on a grid of experimental cross-sections spread over the entire reaction network. Such data are crucial since the calculated cross-sections exhibit uncertainties of several hundred percent even for stable isotopes [10].

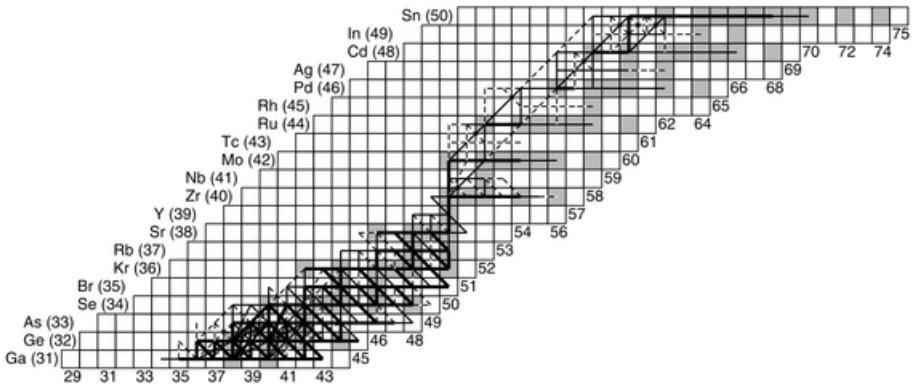

Figure 1.2: Integrated reaction flux during the first second of a Type II SN explosion in the Ne/O layer. Image adapted from [9].

Among the light p-nuclei, several reaction cross-sections have already been studied for several isotopes of Sn. For example, for the ^{112}Sn the (α,γ), the (α,n), the (α,p) and the (p,γ) cross-sections have all been measured [11, 12, 13]. The focus of the present Master Thesis will be on the determination of the $^{118}\mathrm{Sn}(p,\gamma)^{119}\mathrm{Sb}$ reaction cross-section using the Activation Method. This reaction is particularly

interesting because opens the possibility of a new mechanism to produce ^{119}Sn through the decay of ^{119}Sb (see figure 1.3).

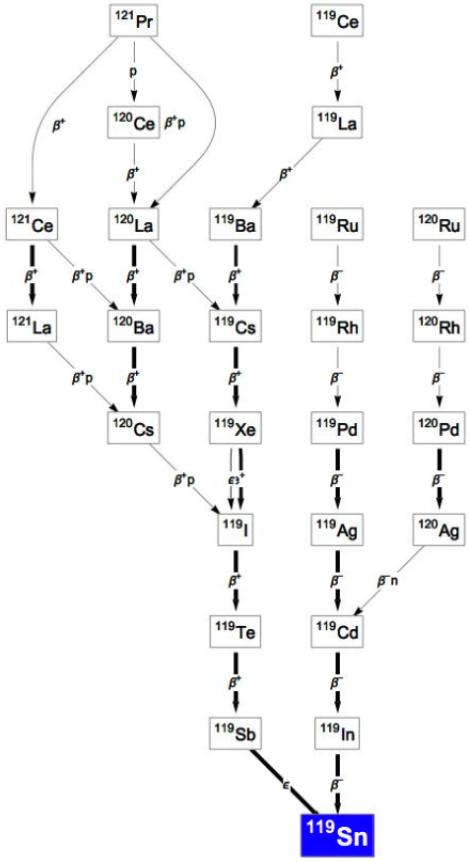

Figure 1.3: Decay chain to the ^{119}Sn isotope. The $^{118}\mathrm{Sn}(p,\gamma)^{119}\mathrm{Sb}$ opens a new mechanism to produce ^{119}Sn.

1.2 Scientific objectives

In this work, the Activation method is going to be used to measure the cross-section of the reaction $^{118}\mathrm{Sn}(p,\gamma)^{119}\mathrm{Sb}$, which has a Q-value of

$$Q = [M(^{118}\mathrm{Sn}) + M(p) - M(^{119}\mathrm{Sb})]c^2 = 5.112\ \mathrm{MeV}, \tag{1.1}$$

where $M(^{118}\mathrm{Sn}) = 109799.256\ \mathrm{MeV}/c^2$, $M(p) = 938.272\ \mathrm{MeV}/c^2$, and $M(^{119}\mathrm{Sb})c^2 = 110732.416\ \mathrm{MeV}/c^2$, are the nuclear masses of ^{118}Sn, proton and ^{119}Sb [14] .

The main objective is to benchmark this method using the X-ray emission associated to the electron capture decay of ^{119}Sb. This reaction is an optimal candidate to test the method proposed by G.G.Kiss and his team [15], since it is possible to apply the Activation Method simultaneously to the γ-emission and X-ray emissions of the ^{119}Sb decay, in the same experiment. To do this, tin targets with different backings were irradiated with 3–4 MeV protons using the Tandem accelerator at the Nuclear and Technological Campus (CTN/IST) in Sacavém, Portugal. These energies lie in the astrophysical energy region of interest known as the Gamow window [16]. The decay spectra were measured using two commercial silicon drift detectors (SDDs) widely used in X-ray analysis. The work was divided into the following steps:

- SDDs' response characterization (chapter 3): Experimental determination of the detectors' energy

resolution and Monte Carlo simulation of their efficiencies using the Geant4 toolkit [17, 18, 19].

- Target production and characterization (section 4.1): Design and construction of a new support for the evaporator, production of targets and backing by vacuum evaporation process, and measurement of the target thicknesses by α-particles energy loss method and Rutherford Backscattering Spectrometry (RBS).
- Proton irradiation and decay acquisition (chapter 4): Irradiation with a proton beam at the 3 MV Tandem at CTN/IST and acquisition of the prompt RBS spectra for target and beam monitoring. Acquisition of γ-decay and X-ray emission spectra at FCUL using the SDDs.
- Data analysis (Chapter 5): Peak analysis of the prompt and γ- and X-ray emission spectra as a function of the decay time, *ab initio* simulation of the X-ray emission spectra based on relativistic atomic structure calculations [20], and determination of the reaction cross-sections using the Activation Method (for the γ- and X-ray emissions) as well as the in-beam RBS spectra.

In the next chapter we give a brief introduction to the RBS formalism and a more in-depth explanation of the Activation Method.

Chapter 2

Measurement of reaction cross-sections

A typical nuclear reaction is denoted by $A(b,c)D$, where a target containing the nucleus A, usually stationary, with a known surface density, N_A atoms/cm^2, that is bombarded by a controllable flux, ϕ_b particles/s^{-1}, of beam particles b. This bombardment will generate a reaction at a rate R_c atoms/s^{-1}, from which c and D are the products. By measuring R_c, it is possible to calculate the cross-section, σ, for this reaction [21].

$$\sigma = \frac{R_c}{N_A \cdot \phi_b}. \tag{2.1}$$

We will focus on radiative capture reactions that are reactions where the light outgoing particle c is a γ-photon. The remaining heavy nucleus, D, can be stable or radioactive. The activation method can only be applied if D is unstable.

2.1 In-beam cross-section measurements

There are different methods to determine R_c. As the nuclear reaction occurs in very short periods of time, the detection needs to be done at the same time as the irradiation (in-beam), as is shown in figure 2.1 for the specific case of radiative capture reactions through the detection of the prompt γ-emission.

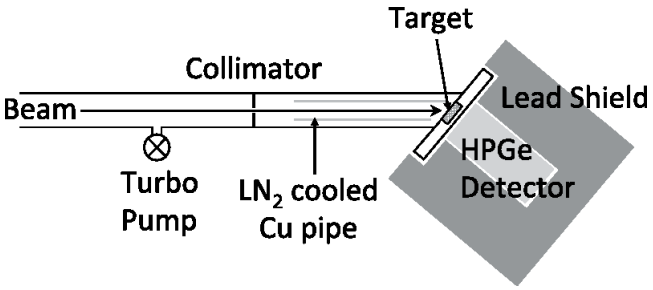

Figure 2.1: Sketch of the experimental setup used for the prompt γ-ray detection, consisting of a HPGe detector placed in close geometry to the target, tilted at an angle of 55^o with respect to the beam axis. Image taken from [22].

There are several disadvantages in using this method. For example, in a radiative capture reaction, $A(b,\gamma)D$, the decay of D to the ground state can involve the emission of one to several γ-photons through intermediate levels. To determine the total reaction cross-section, the complete decay scheme of the compound nucleus must be followed by the detection of all possible γ-transitions. If some transitions remain undetected, it results in an underestimation of the measured cross-section.

Other disadvantages are connected to the fact that the reaction is instantaneous and the measurement has to be made at the same time as the irradiation. For example, while irradiating, the beam will interact with materials other than the target. It can hit the beamline and produce undesired radiation that will also be detected. Another problem is the fact that the measurement of low cross-sections requires a high beam intensity. However, if the beam current is too high, the particle rate arriving at the detector is going to be also high, increasing the detector's dead time. Often time is not easy or even possible to accommodate the detector inside the chamber since it has a fixed geometry. That said, the in-beam method is often a valuable complementary approach to the activation method, described below, as it allows to measure partial cross-sections and to examine reactions where the reaction product is not suitable for activation experiments.

Another way to measure R_c is to determine the number of heavy particles, D, produced in the reaction, but contrary to the light outgoing particles, the heavy product carries a relatively small amount of kinetic energy and cannot leave the target. To overcome this problem, it is possible to use inverse kinematics, where a radioactive ion beam (RIB) of particles A is accelerated towards a target of b atoms, and the recoil D is produced with enough kinetic energy to be detected. However, this is a sophisticated technique that requires a RIB facility and a recoil separator to select the desired reaction products [23].

2.1.1 Backscattering measurements

If the experimental setup allows, it is useful to consider the measurement of the backscattered beam particles, using a charged particle detector located at backward angles. The advantages are two-fold: one can monitor the stability of the target and it is possible to use the measured spectrum and deduce the cross-section, independently of the number of atoms present in the target and of the total charge measured during the irradiation process.

This can be done by considering the differential cross section, since only particles in a solid angle $d\Omega$ are detected and, therefore, only a fraction dR_b of backscattered particles are actually counted. The backscattered beam particles will not, in general be emitted uniformly in all directions, but will have an angular distribution. Considering an arbitrary angular distribution of the particle rate represented by r(θ,ϕ), then $dR_b = r(\theta, \phi)d\Omega/4\pi$, where $d\Omega/4\pi$ represents the fraction of the total solid angle covered by the detector. Thus, the differential cross-section is,

$$\left(\frac{d\sigma}{d\Omega}\right)_{scat} = \frac{r(\theta, \phi)}{4\pi \cdot N_A \cdot \phi_b} \tag{2.2}$$

Using equation 2.1, we can write the total reaction cross-section as

$$\sigma = \left(\frac{d\sigma}{d\Omega}\right)_{scat} \left[\frac{4\pi R_c}{r(\theta, \phi)}\right] \tag{2.3}$$

Since the interaction between the protons and the target material, at the studied energy is dominated by Rutherford backscattering, we can assume that,

$$\left(\frac{d\sigma}{d\Omega}\right)_{scat} = \left(\frac{d\sigma}{d\Omega}\right)_{Ruth} = \left(\frac{zZ_A e^2}{4\pi\epsilon_0}\right)^2 \left(\frac{1}{4E}\right)^2 \left[\frac{1}{\sin^4(\frac{\theta}{2})}\right], \tag{2.4}$$

where Z_A is the atomic mass of the target, z is the atomic mass of the backscattered particle, the E is the energy of the proton, ϵ_0 is the vaccum permittivity, and θ is the center-of-mass angle at which the particles are scattered.

2.2 Activation method

Another standard method used for cross-section measurements is the activation method [24]. By irradiating the target, radioactive nuclei are created in most cases and even though they are still trapped in the target, their decay radiation has enough kinetic energy to escape. By measuring the number of escaping particles, it is possible to indirectly measure the number of produced nuclei, N_D, and from that, one can calculate the cross-section. Since the decay times usually are much larger than the reaction times, the detection does not need to be executed at the same time as the irradiation. This means that many of the problems we have with the In-Beam Method can be overcomed by using the activation method. Although some of the considerations are common to the In-Beam Method, we can identify three main aspects that need to be covered by an activation experiment: target production and characterization, irradiation, and decay measurement.

2.2.1 Target characteristics

The production and characterization of the target are two of the most important steps in cross-section measurements with the activation method. Not only because we need to know the surface density, N_A, of the target to calculate the cross-section, but because there are other physical properties that we have to take into account.

When a charged particle passes through matter, it loses energy very quickly, and if the target is thick enough, it will eventually stop. Thus, in reaction experiments using thick targets, reactions will occur at different energies ranging from the nominal beam energy down to 0, and not at a well-defined energy, resulting in the measurement of an integrated cross-section. On the contrary, if we want to study a reaction at a specific energy, we need to use thin targets, as the energy loss of the beam is small compared to the variations of the cross-section. For example, considering a target of tin with $\Delta x_{Sn} = 600$ nm, the expected energy loss is related to the stopping power of that material,

$$\Delta E = \left(\frac{S}{\rho}\right) \rho \Delta x_{Sn}, \tag{2.5}$$

where $S/\rho = 40.23$ MeV cm^2/g is the mass stopping power for a 4 MeV proton in tin [25] and $\rho = 7.265$ g/cm^3 is the natural tin density. Taking into account these values, the calculated energy loss is $\Delta E \approx 17$ keV for a surface density of $\rho \Delta x_{Sn} = 435$ μg/cm^2 $\approx 2 \times 10^{18}$ atoms/cm^2.

The production of this type of thin layer usually requires vacuum evaporation (see subsection 4.1.1) or sputtering onto a supporting material (backing). The backing supports the irradiated material and can be either a thin or a thick layer of material. A thick backing stops the beam while a thin backing lets it go through without losing much energy. If the backing is thick, then the beam will deposit all its energy in the target, which will heat up and can lead to target degradation and even breaking. To avoid this, we would need a cooling system connected to the sample, which adds more technical challenges to the experiment.

Using a thin backing also poses its own problems, since there is a probability for the radioactive reaction products to escape from the target. For the In-Beam Method, this is not too relevant, as we are measuring the light outgoing particle. However, for the activation method, this becomes a crucial issue. If the produced radioactive nuclei escape the target, we will be measuring less radioactive decays and, consequently, the value of the cross-sections will be underestimated. This is not a problem if the reaction products have low kinetic energies, however, it is something that should be evaluated, in particular, if we are considering using a very thin backing.

Another issue related to the backing is that it can react with the beam and produce particles that will increase the background in both In-Beam and activation methods. To minimize this problem, the backing material needs to be chosen in a way that there are no reaction channels open at the desired energy or, in the case there are, we must assess that they do not influence the measurement of the cross-section in the energy range of interest.

The last consideration is that we need to use a highly enriched target to study specific reactions, otherwise a larger background due to undesired reactions in the target will be produced and less signal due to the lower relative content of the element under study.

2.2.2 Target activation

Focusing on the particular case of activation reactions, when the target is irradiated by a beam with a constant flux of b particles, ϕ_b, with energy above the reaction threshold, radioactive nuclei are produced at a rate $R_c = \sigma \cdot \phi_b \cdot N_A$. While radioactive nuclei are being produced, they are also decaying. The rate at which the number of nuclei, N_D, decay is given by

$$\frac{dN_D}{dt} = R_c - \lambda \cdot N_D, \tag{2.6}$$

where λ [s^{-1}] is the decay constant of the radioactive nucleus, which is related to the half-life through $\lambda = ln(2)/t_{1/2}$. The competition between production and decay eventually reaches an equilibrium ($dN_D/dt = 0$) at the saturation value $N_D^{max} = R_c/\lambda$. This evolution is represented in figure 2.2 .

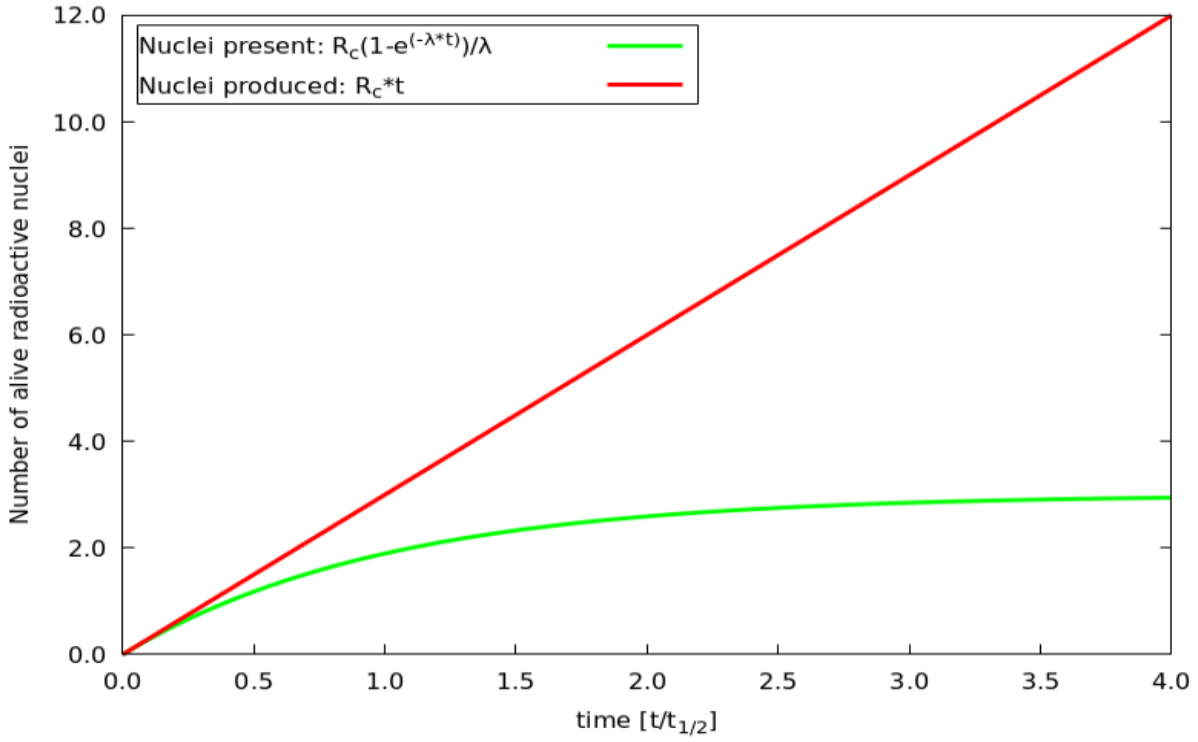

Figure 2.2: Arbitrary representation of the number of produced nuclei in the target during irradiation and the number of present nuclei in the target due to nuclei decay;

Solving this differential equation, we get that the number of produced nuclei, N_D, at any time, t, during the irradiation,

$$N_D(t) = R_c \frac{1 - e^{-\lambda t}}{\lambda} + N_D(0) \cdot e^{-\lambda t}, \tag{2.7}$$

where $N_D(0)$ is the number of produced nuclei at the beginning of the irradiation. In our case, this number is zero and so we can rewrite this equation as,

$$N_D(t) = \sigma \cdot N_A \cdot \phi_b \cdot \frac{1 - e^{-\lambda t}}{\lambda}, \tag{2.8}$$

Therefore, by measuring the number of nuclei, $N_D(t_{irr})$, existing after some irradiation time $t = t_{irr}$, knowing well the beam flux and target thickness, and taking the decay constant from the literature, it is possible to determine the reaction rate and, hence, the cross-section.

One important aspect is the measurement of the total charge collected during the activation of the target, which can be converted into the beam flux. In most cases, the beam current is not constant during the entire irradiation period. It is thus useful to register the beam current as a function of time, allowing for the discretization of the irradiation period in several intervals of time, where ϕ_b can be considered constant. Considering n equal time intervals, equation 2.8 can be rewritten as,

$$N_D(t_{irr}) = \sigma \cdot N_A \cdot \frac{1 - e^{-\frac{\lambda t_{irr}}{n}}}{\lambda} \cdot \sum_{i=1}^{n} \phi_b^i \cdot e^{-\frac{\lambda t_{irr}(n-i)}{n}}, \tag{2.9}$$

where the last factor takes into account the decay during the intervals. If we cannot consider equal intervals of times the equation becomes slightly more complex (see section 5.2).

2.2.3 Decay acquisition

Once the irradiation is over, the production of the radioactive nuclei of interest stops, reaching a value $N_D^{irr} = N_D(t_{irr})$, resulting in a pure exponential behaviour of the number of existing isotopes N_D:

$$N_D(t) = N_D^{irr} e^{-\lambda \cdot t}, \tag{2.10}$$

where t is the time after irradiation. In figure 2.3, we can see a representation of the variation of the produced nuclei during and after the irradiation.

In practice, we can express the number of decays, N_{decay} measured, such that they are 0 when the irradiation stops and are N_D^{irr} at infinite time,

$$N_{decay} = N_D^{irr}(1 - e^{-\lambda \cdot t_{acqui}}), \tag{2.11}$$

where t_{acqui} is the acquisition time.

If the number of decays occurred over a period of time t_{acqui} are measured, it is possible to calculate N_D^{irr} and from that the cross-section, σ, using equation 2.8. This equation considers that the acquisition starts as soon as the irradiation stops, which might not be true most of the time. Thus, one needs to correct the number of atoms present at the start of acquisition after a period t_{trans} of transport of the irradiated target to the measuring station,

$$N_{decay} = N_D^{irr} \cdot e^{-\lambda \cdot t_{trans}} \cdot (1 - e^{-\lambda \cdot t_{acqui}}) \tag{2.12}$$

To calculate the number of decays, N_{decay}, we will measure the peak areas in the spectrum of detected particles. If the peak area of the relevant decay is N_{peak}^{part}, the number of decays is, w

$$N_{decay} = \frac{N_{peak}^{part}(t_{acqui})}{\eta \cdot \epsilon_D}, \tag{2.13}$$

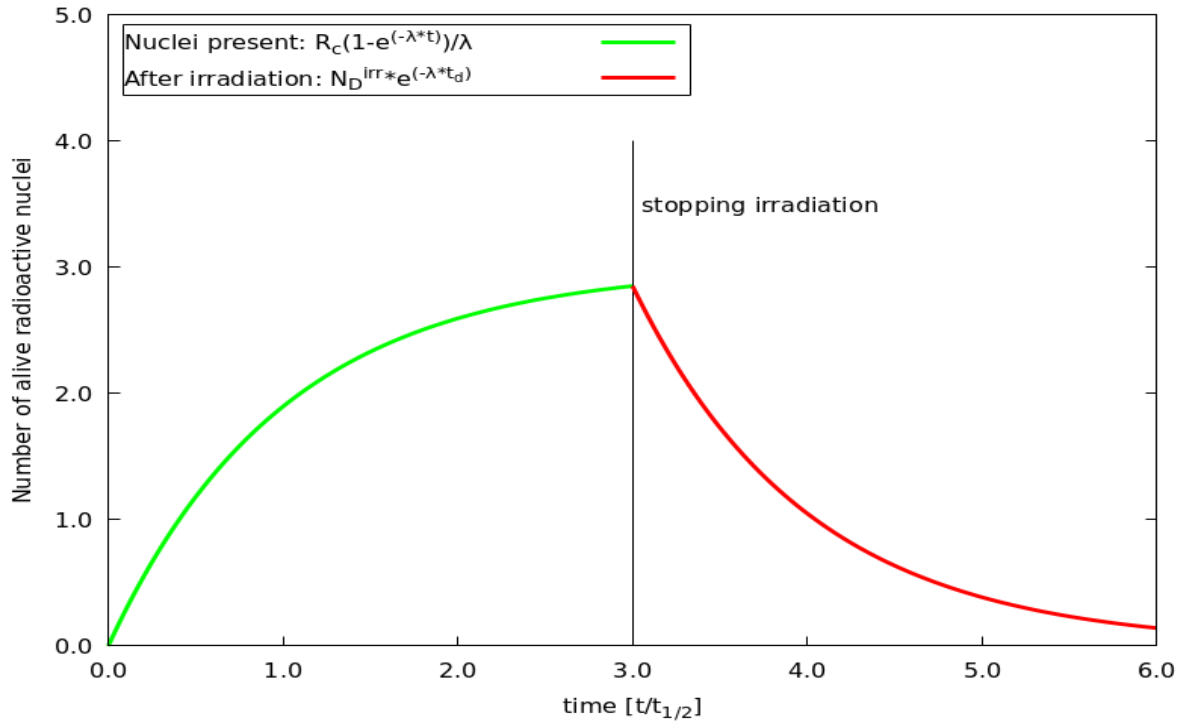

Figure 2.3: Arbitrary representation of the Number of produced nuclei during and after irradiation, where $t_d = t - t_{irr}$. Red - Nuclei number, during irradiation; Green - Nuclei number, after irradiation

where ϵ_D is the detector efficiency and η the relative intensity of the decay, corresponding to the particle emission probabilities.

Using equations 2.13, 2.12, and 2.8 we can write the cross-section as

$$\sigma = \left(\frac{N_{peak}^{part}}{\eta \cdot \epsilon_D}\right) \cdot \left(\frac{e^{\lambda \cdot t_{trans}}}{1 - e^{-\lambda \cdot t_{acqui}}}\right) \cdot \left[\frac{\lambda}{N_A \cdot \phi_b \cdot (1 - e^{-\lambda t_{irrad}})}\right]. \tag{2.14}$$

Several reaction cross-sections have been measured over the years using the activation method: (p, γ) reactions on ^{102}Pd, ^{116}Sn, and ^{76}Ge [26]; (α, γ) on ^{112}Sn [27], (p,n) on ^{76}Ge [16].

However, this method has some limitations. For instance, both t_{irr} and t_{acqui} are set by the value of $t_{1/2}$. If the half-life is too long, then the irradiation time needs to be longer as well, otherwise, the number of produced radioactive nuclei might be too low and we will not have enough signal to allow measuring the cross-section. The same happens with the detection time. If the half-life is long, then a longer detection time is needed to compensate for the low activity. A long half-life also has some advantages, as the number of decays that occur during the transport is minimal and not much signal is lost during the transport to the measuring station.

The main limitation is that the activation method can only be applied to radioactive products, and only in the case that the emitted particles can be detected. For example, it can not be applied when the emitted particles are neutrinos solely. That is the case for radioactive isotopes that only decay via electron capture with no γ-emission associated. However, it was proposed by G.G.Kiss and his team [15] that one might be able to measure these types of decays by measuring the X-rays that are emitted in the atomic cascade after electron capture.

2.3 Activation method using X-rays

For unstable proton-rich nuclei, the available decay modes are positron emission and electron capture. We are going to focus on the latter, as positron emission can be measured easily using the two γ-photons from positron annihilation. Quite often, the electron leaves the daughter nucleus in an excited state, decaying to the ground state by γ-emission. In these cases, one can apply the activation method using the emitted γ-emission peak of the reaction product. However, for isotopes where electron capture proceeds directly to the ground state of the daughter nuclei or the γ-emission exists but with a very low intensity, this method can not be applied. In these cases, we can only apply the activation method by measuring the X-ray emission from the atom after electron capture.

In figure 2.4, we can see a representation of the electron capture decay. In this decay, an electron from an inner atomic shell, K or L, will be absorbed by the nucleus. This leaves a vacancy in an inner shell of the atom that will be filled by an outer shell electron, emitting a characteristic X-ray. Atomic relaxation proceeds through a series of X-ray and Auger electron emissions, propagating the inner-shell vacancy to the outer shells. This process occurs right after the electron capture decay. Thus, by measuring the intensity of the characteristic X-rays emitted by the reaction product as a function of time, and using equation 2.13 it is possible to determine the number of radioactive nuclei created in the irradiation.

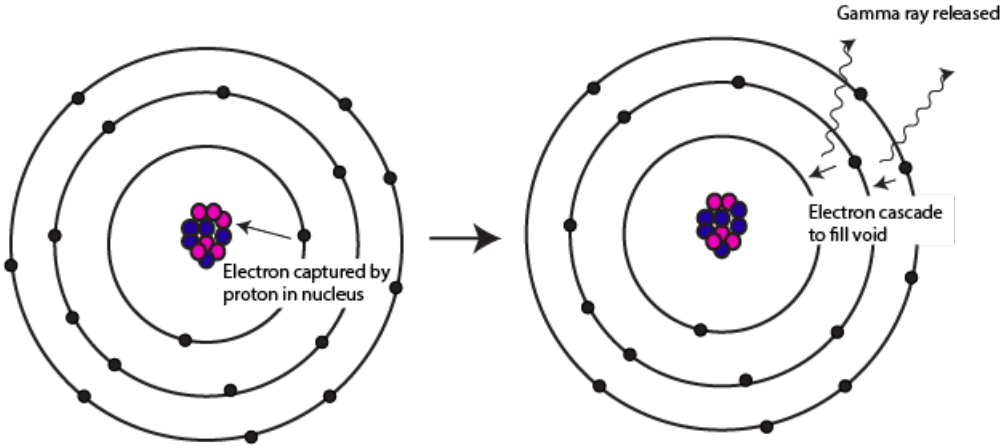

Figure 2.4: Scheme of the X-ray emission resulting from electron capture. The inner-shell electron capture (left) is followed by an atomic transition leading to a X-ray emission (right).

As mentioned before, it is desirable to have a highly enriched target and that becomes crucial when applying the activation method with X-rays. Since nuclear effects on the atomic energy levels (hyperfine splitting and mass shift corrections) are small, a major disadvantage of using X-ray emissions is that they are characteristic of the atom and not of the isotope.

If the target consists of several stable isotopes of the same element, then the beam will induce various reactions, most of them leading to different isotopes of the same element, emitting the same X-rays and increasing the systematic uncertainty of the measurement. Eventually, if the half-lives of the produced isotopes are different enough, the decay will be described by a superposition of different individual decays. For example, considering two isotopes, the number of decays will be $N_{decay} = N_{decay}(1) + N_{decay}(2)$, where each term is given by the corresponding equation 2.11. The only free parameters will be $N_D(1)$ and $N_D(2)$ that can be determined by fitting the experimental data.

2.3.1 Activation method applied to ^{118}Sn$(p,\gamma)^{119}$Sb reaction

We now apply the activation method to the reaction ^{118}Sn$(p,\gamma)^{119}$Sb. ^{119}Sb decays 100 % by electron capture into an excited state of ^{119}Sb, located at an energy of 23.9 keV, as shown in Fig. 2.5. This excited state decays into the ground state by two competing decays: internal conversion, emitting atomic electrons of energies around 20 keV (B_e(L-shell) = 4 keV); and by γ-emission of 23.9 keV photons.

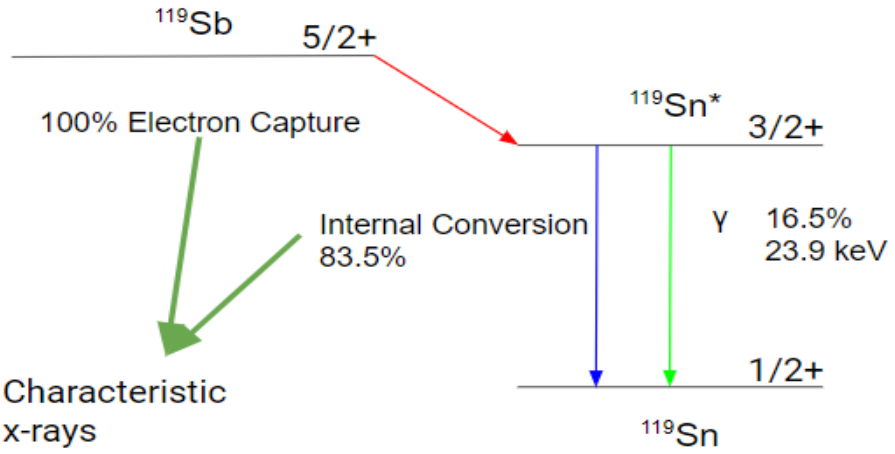

Figure 2.5: Decay scheme of the ^{119}Sb decay to ^{119}Sn

Following the electron capture, the atomic deexcitation proceeds by the emission of Auger electrons and characteristic X-rays of the element, in this case Sn. The K- and L-lines of Sn can be found in table 2.1. The energy range of interest to acquire the spectra is between 20 and 30 keV, including the γ-emission and the Kα and Kβ lines.

Table 2.1: Characteristic X-ray lines of ^{119}Sb taken from [28]

X-ray	Energy [keV]	Relative X-ray intensity per decay [%]
Lα_1	3.444	11.8 $\pm$ 0.4
Kα_2	25.044	21.0 $\pm$ 0.5
Kα_1	25.271	38.9 $\pm$ 0.9
Kβ_3	28.444	3.5 $\pm$ 0.8
Kβ_1	28.486	6.80 $\pm$ 0.15
Kβ_2	29.111	1.86 $\pm$ 0.40

Knowing the intensity of each peak and the detector efficiency for that energy, it is possible to calculate the number of decays, N_{decay} using the γ-emission and X-ray lines. If the relation between the yields of both peaks is the same as in the literature, then the cross section calculated from them will be the same and the method is validated.

Chapter 3

Detector response characterization

For our acquisition, we used two similar solid state detectors widely used in X-ray fluorescence analysis: the XR-100SDD from Amptek [29] and the SXD15M-150-500 from Canberra [30], both Silicon Drift Detectors. The XR-100SDD detector can provide an energy resolution of 125 eV FWHM at the Mn Kα line, at 5.9 keV,(electronic noise of 4.5 electrons rms), a peak to background of 20000:1, an output count rate over 500 kcps, and can detect X-rays down to the Be Kα line (110 eV). For the SXD15M-150-500, we have an energy resolution of 145 eV FWHM at the Mn Kα line.

Since the manufacturer presents the resolution only for one energy, we start by determining the resolution as a function of energy using X-ray sources with characteristic energies. To determine the response of the detectors in the geometric conditions of acquisition, we implemented a Monte Carlo simulation to compute their efficiencies that takes into account the parameterization of the energy resolution.

3.1 Energy calibration and detector resolution

The energy calibration and resolution of the detectors was obtained using a variable X-ray source. This source has two components, a source of ^{241}Am and several targets of different elements mounted on a wheel. By rotating the wheel, the different targets can be exposed to the 59.6 keV gamma rays emitted by the source, ionizing them and producing X-ray emission characteristic of those elements. In our source the targets were made of barium, silver, copper, terbium, and molybdenum.

The detectors were placed at 5 mm from the variable source and the spectra were acquired for several minutes until we had enough statistics, usually the acquisitions took from 10 to 15 minutes.

The calibration was done with a ROOT script that fits a Gaussian to the peaks to obtain the centroid channel and the σ_{det} value, which is the standard deviation. The energy calibration line is shown in 3.1 and the resolution dependence on energy is presented in figure 3.2 for both the detectors. The resolution was fitted with both a linear and a quadratic function of the form,

$$R = \frac{\text{FWHM}}{E} \approx 2.355\frac{\sigma_{det}}{E} = \frac{a}{E} + \frac{b}{\sqrt{E}} + c, \tag{3.1}$$

where a, b, and c are the fit parameters ($a = 0$ in the linear fit).

We note that Kα or Kβ sum peaks were not included in the fits, since they would artificially decrease the resolution. The resolution of the detectors for the relevant emission energies in this work can be found in table 3.1. As we can see the energy resolution is not enough to separate the fine splitting K$\alpha_{1,2}$ lines, but should suffice to separate four peaks: the Kα = Kα_1 + Kα_2 line, the K$\beta_{1,3}$ = Kβ_1 + Kβ_3 line, Kβ_2 line, and the γ-emission.

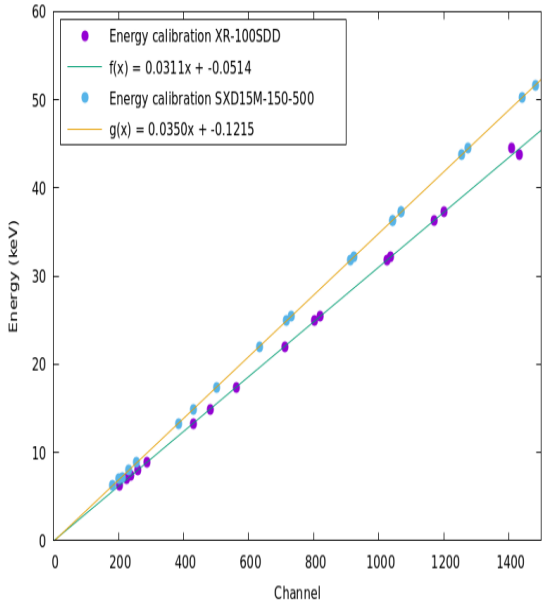

Figure 3.1: Graphic representation of the calibration curve for both detectors. A linear regression was applied to the measured values.

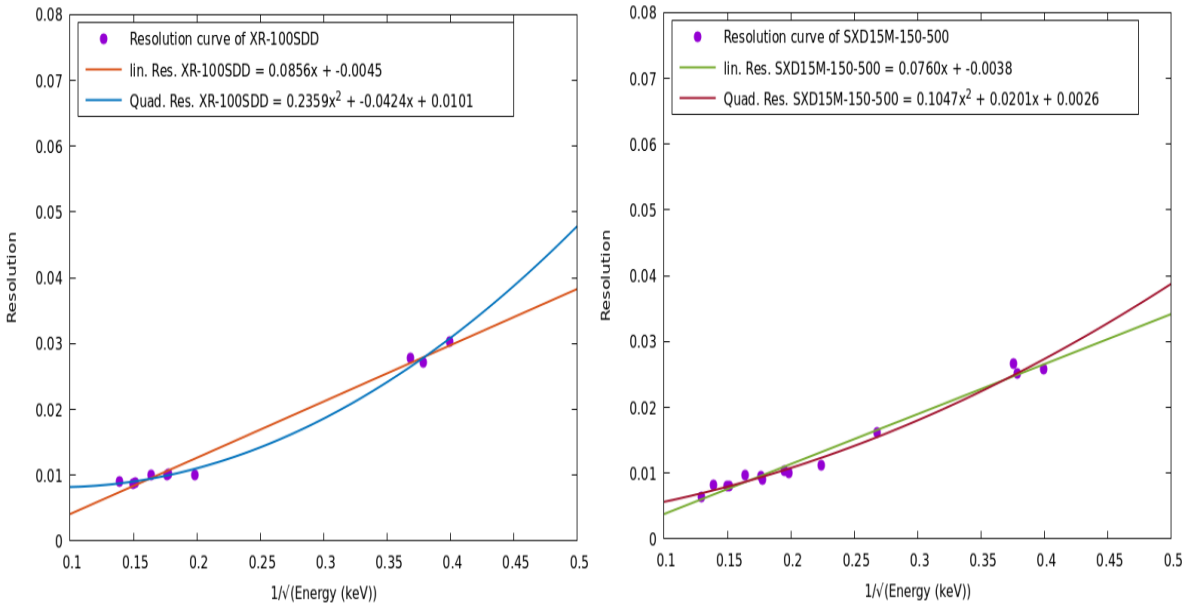

Figure 3.2: Graphic representation of the resolution curve for both detectors. Linear and quadratic regressions were applied to the measured values.

Table 3.1: Detectors resolution for the energies of interest in our work.

X-ray	Energy [keV]	XR-100SDD	SXD15M-150-500
γ	23.8	0.415	0.367
Kα_2	25.044	0.426	0.377
Kα_1	25.271	0.428	0.378
K$\beta_{1,3}$	28.465	0.454	0.402
Kβ_2	29.111	0.460	0.406

3.2 Simulation of the detector efficiency

The efficiency of the detector, ϵ_D, is a fundamental parameter to determine the cross-section, as can be seen in equation 2.14. This quantity is defined as,

$$\epsilon_D = \frac{N_{detected}}{N_{emitted}}, \tag{3.2}$$

where $N_{detected}$ is the number of events counted by the detector and $N_{emitted}$ is the number of particles emitted by the source. The experimental determination of the detectors' efficiencies is rather difficult, because it requires calibrated sources with very well-known activities, emitting in the energy range of interest. Monte Carlo simulations provide a more practical, inexpensive, and accurate way to determine the efficiency of a detector. Therefore, we implemented a Monte Carlo simulation of both detectors in Geant4 [17, 18, 19], using the G4EmStandardPhysics physics list that considers the photoelectric and Compton effects, and pair conversion.

To simulate the detector efficiency, one needs to implement the detector geometry and the particle source. The electronic components were not included in the geometry, since only the energy deposition in the detector is considered. The simulation can not model the electronic noise, although it can be important in the peak shaping. Both detectors are very similar, unless said otherwise the simulation approaches are the same.

3.2.1 Detector geometry

The geometry of the detector implemented in the simulation was based on the technical drawings of the detector presented by the manufacturer (see figure 3.3). The geometry included the detector cover, the beryllium window, the multilayer collimator, and the silicon detector. Behind the detector there is also a substrate that can contribute to the dispersion of photons inside the detector and increase noise. However, it was not included because the material composition of the substrate was unknown and we found that it was not necessary to reproduce the measured spectra.

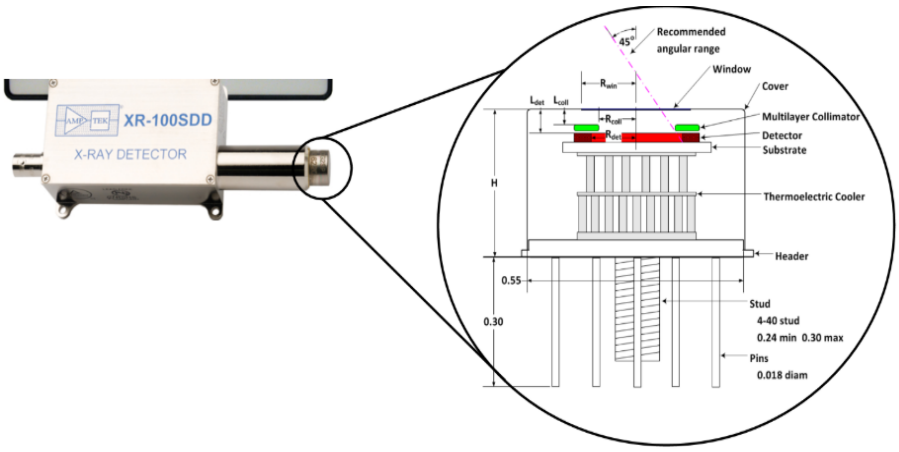

Figure 3.3: Detector geometry, image adapted from [31]

The physical characteristics of the geometry components are shown in table 3.2 and the full geometry of the detector is shown in figure 3.4. The multilayer collimator is made of several materials, tungsten, chromium, titanium, and aluminum.

The geometry was positioned using the distances given by the manufacturer:

Table 3.2: Main physical characteristics of the detector's components.

Component	Internal radius [mm]	External radius [mm]	Thickness [mm]	Material
Cover	3.5	15.24	0.254	Ni
Window	–	3.5	1.2×10^{-4}	Be
Collimator	2.33	2.82	0.225	Multilayer
Detector	–	2.82	0.500	Si

- For the XR-100SDD
  - Cover and beryllium window are in the same plane;
  - Colimator is 0.9 mm from the interior face of the cover;
  - Si Detector is 1.4 mm from the interior face of the cover.
- For the SXD15M-150-500
  - Cover and beryllium window are in the same plane;
  - Colimator is 1.6 mm from the interior face of the cover;
  - Si Detector is 2.1 mm from the interior face of the cover.

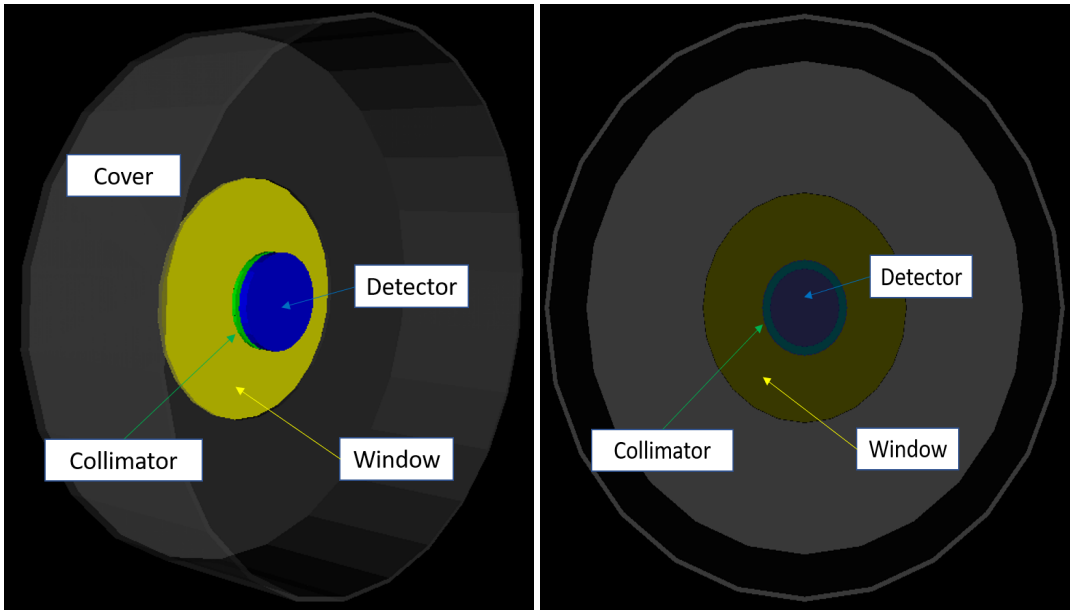

Figure 3.4: XR-100SDD geometry implemented in Geant4.

3.2.2 Sources definition

The simulations were carried out in such a way as to distinguish both intrinsic, ϵ_i, and geometric, ϵ_g, efficiencies, according to,

$$\epsilon_D = \epsilon_g \cdot \epsilon_i, \tag{3.3}$$

To determine the intrinsic efficiency, we defined a point source of monochromatic photons emitted in vacuum in the direction perpendicular to the detector plane. In this configuration, equation 3.2 gives the value of ϵ_i, as the geometrical efficiency is 1. Figure 3.5 shows the simulated spectrum obtained

with $N_{emitted} = 2 \times 10^6$ monodirectional 15 keV photons generated from a point source. The histogram shows the well-defined photopeak at the right energy bin and the Compton edge structure around 1 keV (the Compton edge of a 15 keV photon is 0.83 KeV). The area under the photopeak gives the number of detected photons, $N_{detected} = 1.35 \times 10^6$, with 15 keV, and hence an efficiency of $\epsilon_i = (1.35 \times 10^6/2 \times 10^6) = 0.68$.

To simulate the geometrical efficiency of a point source, we need to change from the monodirectional emission to an isotropic emission. In this case, the result is well-known:

$$\epsilon_g = \frac{\Omega}{4\pi} = \frac{\pi r^2}{4\pi d^2}, \tag{3.4}$$

where r is internal radius of the detector's collimator and d is the source-detector distance. Considering $r = 2.33$ mm and $d = 5 + 1.4$ mm, where 5 mm is the distance from the source to the detector and 1.4 mm is the distance from the face of the detector to the front of the detector, the geometrical efficiency is $\epsilon_g = 0.033 \pm 0.001$.

The efficiencies were simulated in both configurations for 500 photon energies in the range 1-2 keV in intervals of 0.05 keV and in the range 2-50 keV in intervals of 0.1 keV. These are represented in the top panel of figure3.6, where the simulated geometrical efficiency was obtained by $\epsilon_g = \epsilon_D/\epsilon_i$. It can be seen that, the intrinsic efficiency dominates in the whole energy range, and that, the geometric efficiency is well described by the point-source approximation. The simulations for the SXD15M-150-500 detector give almost identical efficiencies to the XR-100SDD detector as it can be seen in the bottom panel of figure 3.6. The difference between the two detectors efficiency comes from the geometrical efficiency as the collimated area and the distance of the silicon to the window are different as we saw previously.

It is important to note that in order to accurately simulate the photon energy deposition process in the detector, it is necessary to activate the atomic deexcitation cascade that is not present by default in the StandartEMphysics list. Without this option, the energy deposited in the photoelectric absorption is always given by the difference of the incident photon energy minus 1.84 MeV, corresponding to the K-shell electron ionization potential in silicon. However, after ionization it is necessary to consider the loss of energy due to the emission of X-rays that escape from the detector and will decrease the efficiency and increase the energy broadening.

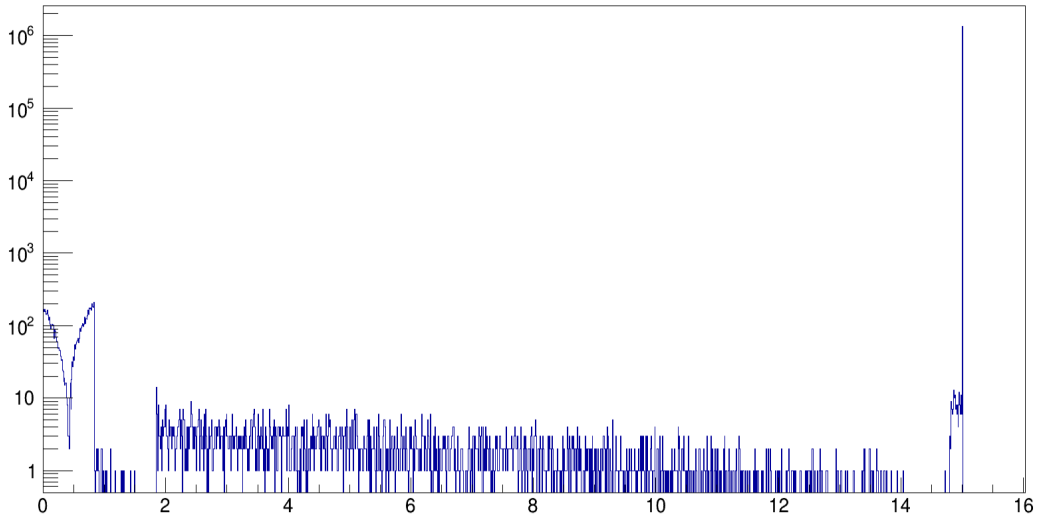

Figure 3.5: Histogram of energy deposited in the silicon volume by a monodirectional beam of 15 keV photons from a point-source.

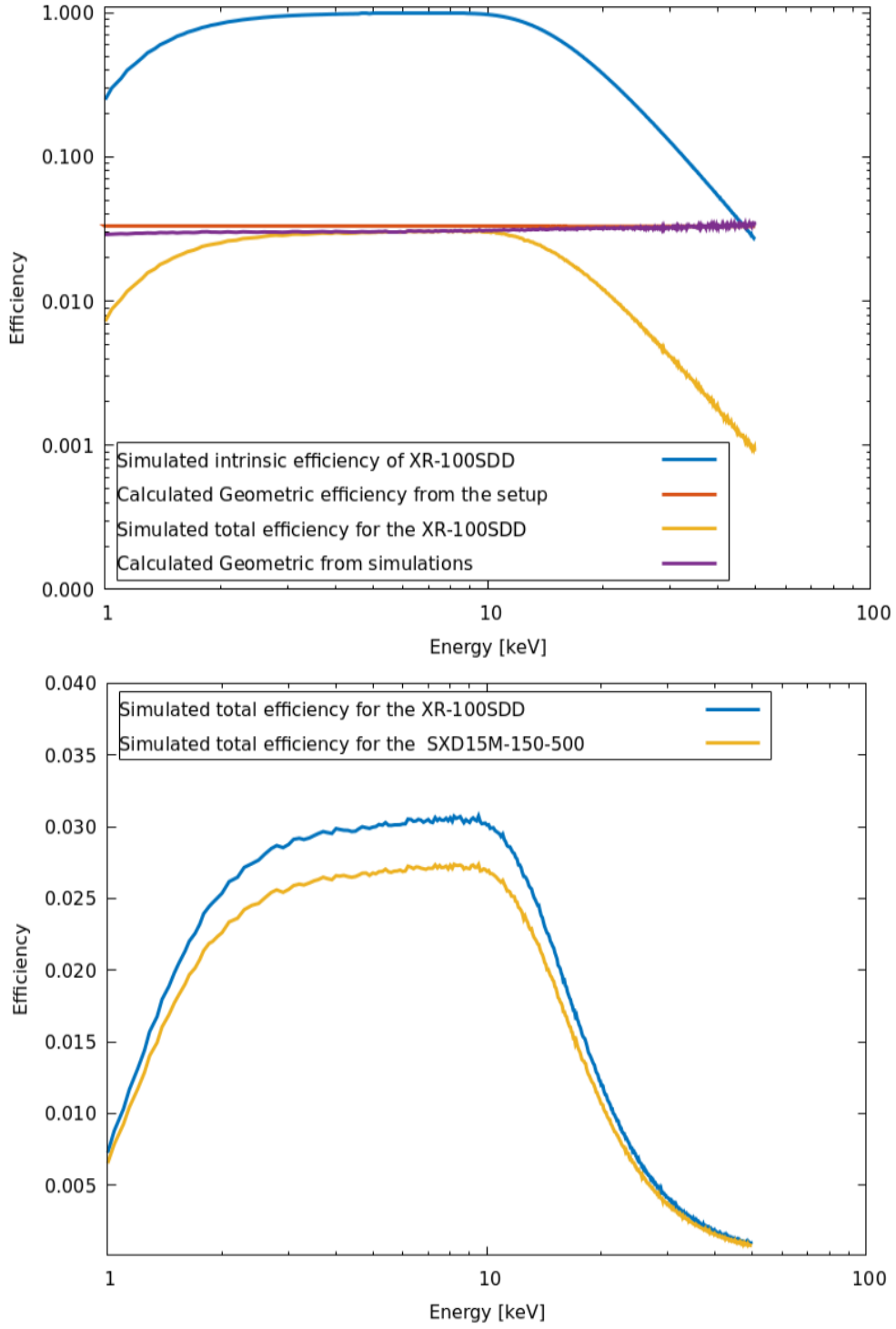

Figure 3.6: Simulated efficiency curve of the detectors. Top panel: comparison of the geometrical and intrinsic efficiencies for the XR-100SDD detector. Bottom panel: comparison of the total efficiencies of the XR-100SDD detector and the SXD15M-150-500 detector.

In the real situation, we do not have a point source, but a cylindrical volume of emission with a base radius of about 0.2 mm, corresponding to the area of the beam spot on the target, and a height equal to the target thickness. Therefore, the efficiency of our detector should have that into account, this will be presented in chapter 5.

3.3 Detector response simulation

To check the quality of the detector response model, the spectra for different X-ray sources were compared with simulations taking into account the energy resolution determined previously. The histogram of the primary photon spectra for the different sources was constructed from available X-ray emission tables [28]. In our simulation, the source energies were sampled from this histogram using ROOT libraries in the PrimaryGeneratorAction class of Geant4.

The result of this simulation is a spectrum of energy deposited in the detector with a resolution equal to the peaks natural linewidths or equal to the user-defined energy binning. The inclusion of the detector resolution can be done in two ways: i) convoluting the simulated spectrum with a peak broadening function that takes into account the σ_{det} value for each energy or ii) using this function within the simulation to randomly sample the energy deposited around the mean value, corresponding to the centroid of the peak.

Figure 3.7 shows the comparison between the Ba spectra measured with the XR-100SDD detector and the simulated spectra with and without peak broadening. The broadening was included using method ii) with a Gaussian function. The simulation is able to reproduce the emission peaks of barium at the right energies as well as the nickel and tungsten emissions from the cover and from the collimator, respectively (see table 3.3). Zooming in the barium Kα peaks region (see the right plot of figure 3.7), it is possible to observe that the quadratic fit produces a better description of the measured peak separation.

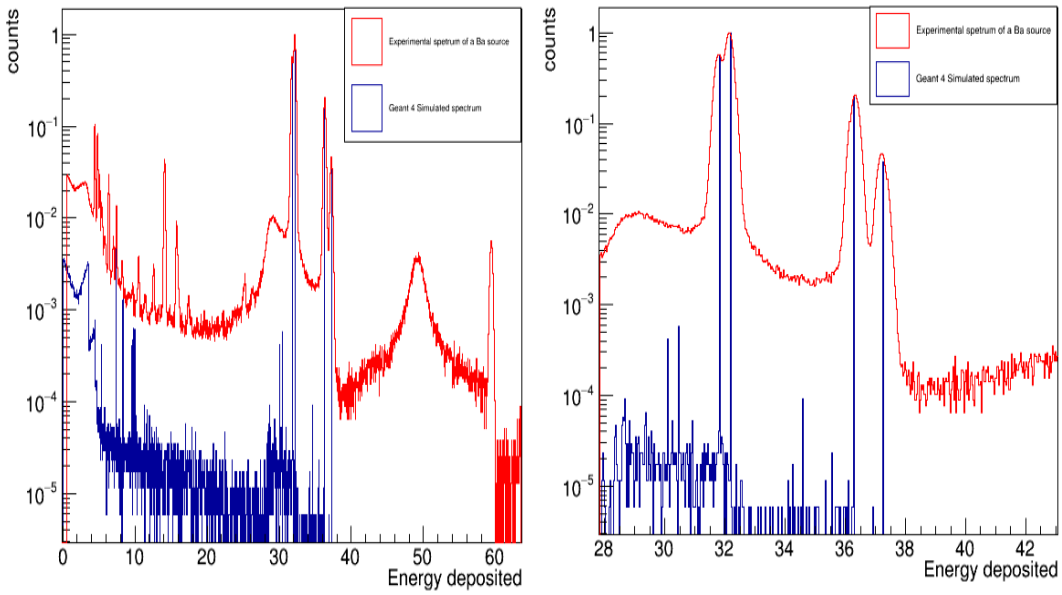

Figure 3.7: Histogram of the Ba spectrum with both the experimental data (red), and simulated data (blue). Both the experimental and the simulated histograms are normalized to the highest peak.

The detector's resolution is the cumulative result of several effects such as statistical fluctuations of charge creation in the sensitive volume, incomplete charge collection, and electronic noise. These effects can be parametrized as,

$$\sigma_{det} = \sqrt{\epsilon F E + \sigma_{noise}^2}, \tag{3.5}$$

where $F = 0.11$ is the Fano factor for silicon, $\epsilon = 3.63$ eV is the energy needed to create an electron-hole pair in silicon [32], and σ_{noise} is a fit parameter that accounts for the increase in σ_{det} due to the electronic noise. The resolution calculated in this way with $\sigma_{noise} = 0$ allows to obtain the separation of the Ba Kα

Table 3.3: X-ray emission energies and intensities for Ba, Ni, and W taken from [28].

Peak	Energy (keV)	Intensity (%)
Ba Kα_2	31.817	25.8
Ba Kα_1	32.194	47.6
Ba Kβ3	36.304	4.46
Ba Kβ_1	36.378	8.61
Ba Kβ_2	37.255	2.72
Ni Kα_1	7.478	24.9
Ni Kβ_3	8.265	1.53
Ni Kβ_1	8.265	2.99
W Lβ_1	9.672	10.82
W Lβ3	9.819	1.33
W Lβ_2	9.955	2.253
W Lγ_1	11.285	2.03
W Lγ_6	11.538	0.078
W Lβ_2	11.608	0.049

peaks closest to the measured spectrum, as it can be seen in figure 3.8.

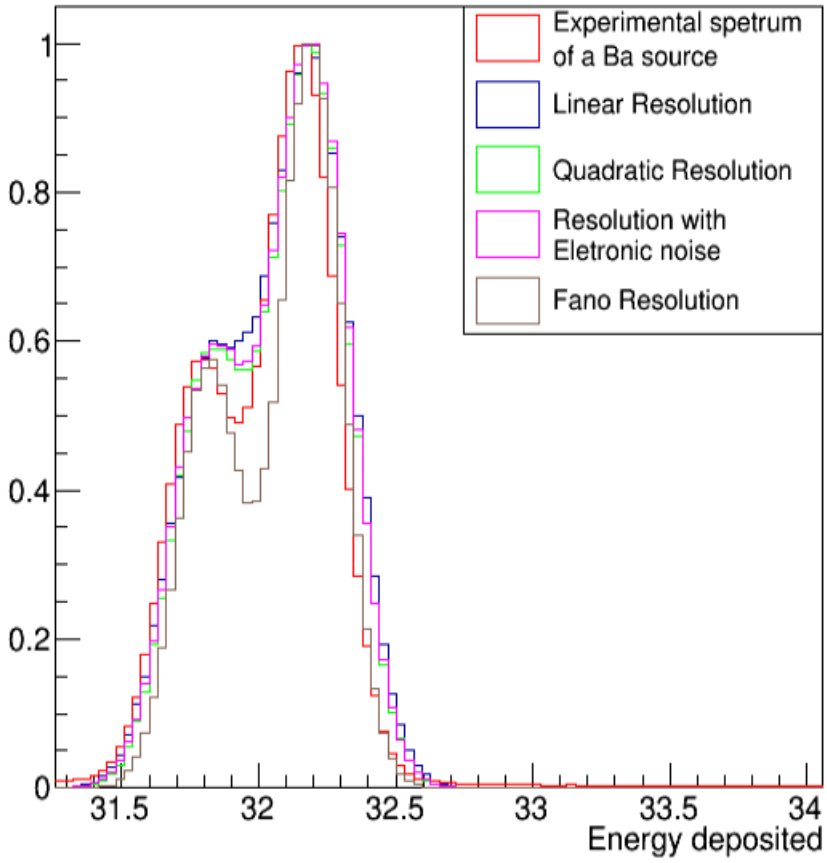

Figure 3.8: Histogram of the measured Ba spectrum (red) in the Kα peaks region compared with the simulated ones for different parametrizations of the resolution profile: linear (blue), quadratic (green), equation 3.5 with fitted noise term (pink), equation 3.5 with no noise term (grey). Both the experimental and the simulated histograms are normalized to the highest peak counts.

Even though the resolution using only the term from the Fano statistics gives us a good approximation, we have to take into account that it is purely theoretical and does not have any influence from the measured

spectrum.

3.3.1 Silver spectrum

The response function was applied to the silver spectrum, since this element emits X-rays in the same energy region of tin. The Kα_1 (22.16 keV), Kα_2 (22.00 keV), and Kβ_1 (24.94 keV) emissions of silver were simulated.

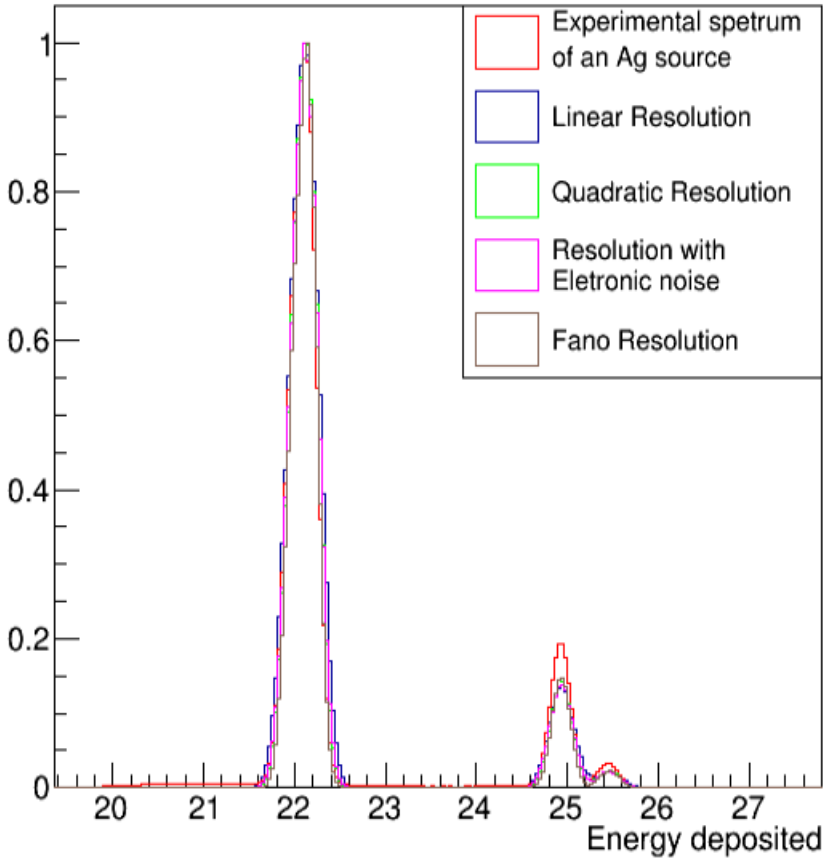

Figure 3.9: Histogram of the measured Ag spectrum (red) in the Kα and Kβ peaks region compared with the simulated ones for different parametrizations of the resolution profile: linear (blue), quadratic (green), equation 3.5 with fitted noise term (pink), equation 3.5 with no noise term (grey). Both the experimental and the simulated histograms are normalized to the highest peak counts.

In this case, the measured spectrum is simulated rather well. This might be because our parametrization curve is optimized for these energies or most likely because the detector can not separate the fine structure of Kα emissions.

Chapter 4

Experimental procedures

In addition to the characterization of the detector response, the work involved three experimental stages: the production and characterization of the targets, the irradiation of the targets with the proton beam, and the acquisition of the decay spectra. For the production of the targets, it was necessary to design and build a new support to be used in the evaporator. The thicknesses of the targets were determined using the RBS method and by measuring α-particles energy loss.

4.1 Target production and characterization

The targets were produced at LIP's NUC-RIA laboratory in FCUL using the vacuum evaporation method. In this method, the backing and the layers are evaporated over a glass cover-slip mounted on a support placed inside the evaporator.

Since the available support was old and fragile and did not have all the features required, we designed in CAD a new support that was constructed at LIP´s Mechanical Workshop (see figure 4.1). All parts of the support were made of stainless steel.

For example, the new support allows changing the height of the glasses, so one can evaporate at different heights if needed. For that, the main piece has holes where a bar can be introduced to choose the height of evaporation as shown on the left picture of figure 4.1. Another feature was the possibility to remove the glass holder so that the glasses could be changed without having to move the support. By having a removable holder, it is also possible to use other types of holders for different types of glasses, without the necessity of having a new support.

4.1.1 Target production

The vacuum evaporation process involves two basic stages: the evaporation of the material required to make the film and the condensation of that material onto a substrate. To evaporate the material, either electrical or electron beam heating are used. These processes are made in high vacuum, around 10^{-6} mbar, since by reducing the pressure, we also reduce the temperature needed to change the state, so it is possible to evaporate at lower temperatures. To heat up the material, a sample is positioned in a boat, usually made of tungsten, molybdenum, or tantalum [33]. The boat is then heated electrically until the material sample evaporates. This vapor travels to the surface of the substrate and gradually cools down, forming a thin film layer.

In this work, an evaporator device from the company Balzers (shown in figure 4.2) was used to produce the target films. The quality of the films will depend on various aspects: on the temperature

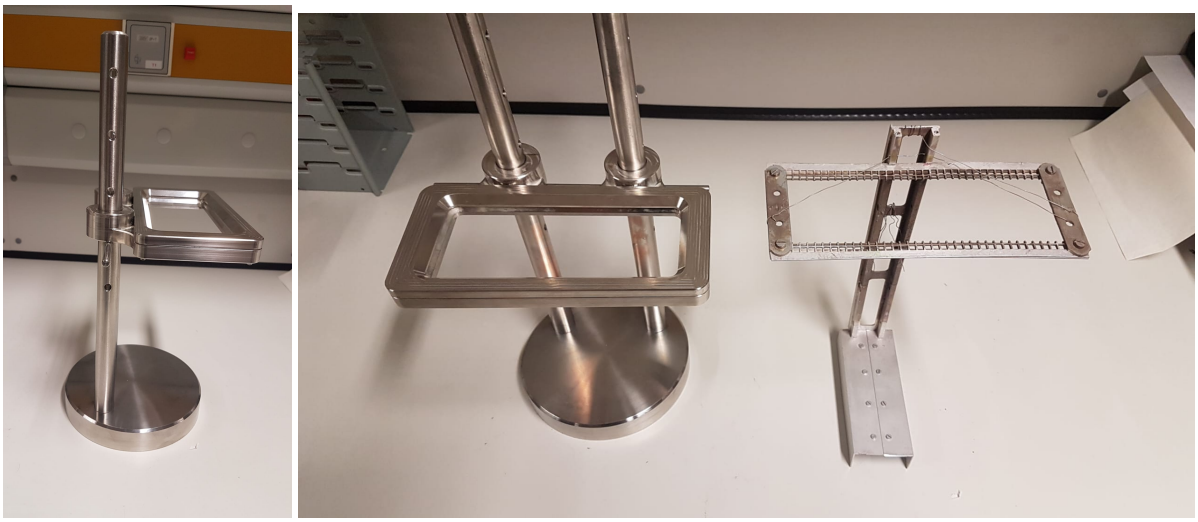

Figure 4.1: Comparison of the new and old evaporation supports used to produce the target. Left picture: side view of the new support. Right picture: front view of the new (left) and old (right) supports.

of the boat, which is proportional to the applied current; on the evaporation time, since evaporating at a constant temperature for a long period of time produces more homogeneous targets; and on the quality of vacuum. High vacuum not only allows for the evaporation to be possible at lower temperatures but also allows the vapor particles to deposit directly on to the substrate without suffering collisions with air particles [34]. Typical vacuum values were of the order of 10^{-7} mbar prior to the evaporation and 10^{-6} mbar during the evaporation.

The Sn targets produced in the framework of this Master Thesis were evaporated onto two different kinds of backing materials: a manufactured Al film, and a self-produced Cu backing.

Al backing

The first target produced was of natural Sn evaporated over a backing of Al film with 0.8 μm from Goodfellow. This was the first test to confirm if we could evaporate a thin layer of Sn, but thick enough to result in a significant yield of the reaction under study.

This evaporation was still done using the old evaporator support. We prepared six target holders and a glass slide with an aluminium layer and evaporated over them. The target holders were fixed on to a slide with a metallic Cu tape. After the evaporation, we noticed that three of the targets fell before the evaporation started, so the method used to tape the targets needed to be improved.

We used a molybdenum boat with 99.99 % of purity from Goodfellow, where 87.1 ± 0.1 mg of natural Sn were placed. The initial mass of the boat+Sn was of 518.4 ± 0.1 mg. The evaporation process started with a pressure of 2.5×10^{-6} mbar and steadily, the current applied to our boat was increased, while controlling the pressure to keep it close to the initial value. We used a thickness monitor detector to estimate the amount of Sn that was evaporating. This detector has a crystal that vibrates at different frequencies depending on the amount of material on its surface and converts this vibration differences into evaporated thickness. Since there was no previous calibration of the detector crystal, it was not possible to assess how much Sn was evaporating, but one could check whether the evaporation process was taking place or not.

The evaporation started at a pressure of 6.3×10^{-6} mbar, being kept at this pressure for about 10 minutes. The current was increased after that, with an initial increase of the pressure (8.5×10^{-5} mbar), but only an additional increase in the current resulted in a significant feature of the evaporation, with a

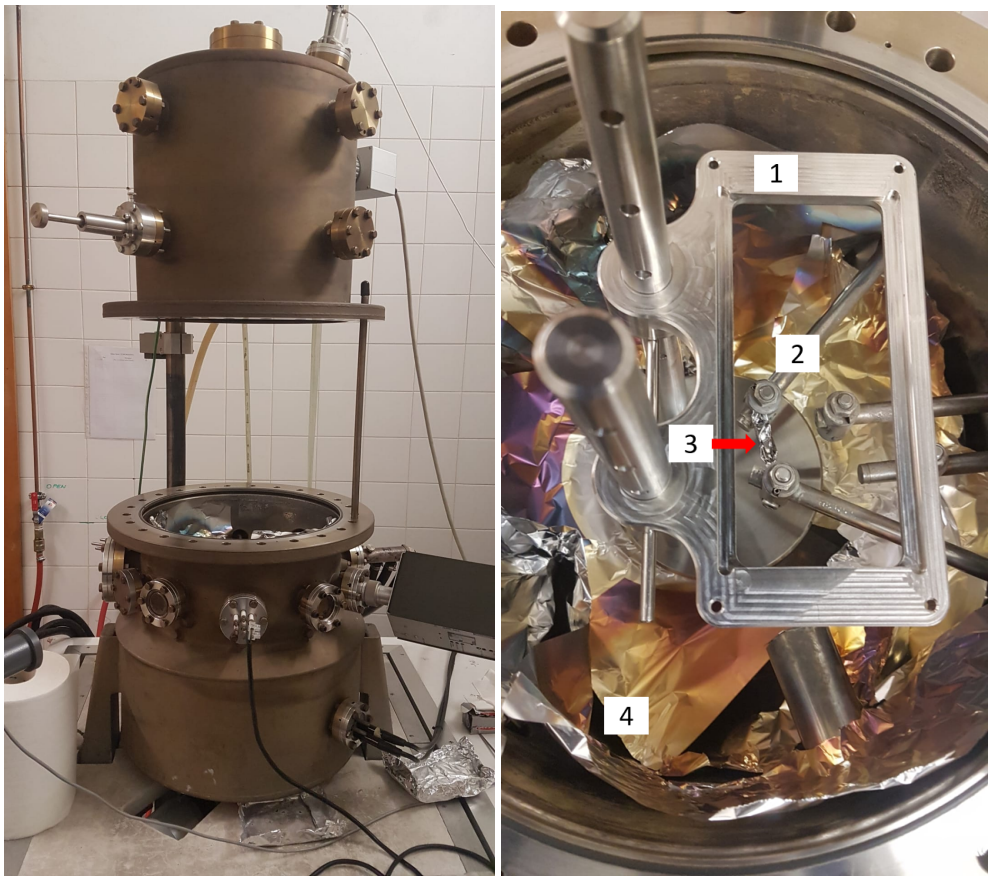

Figure 4.2: Left picture: Balzer evaporator opened. Right picture: Inside of the Balzer evaporator showing the (1) new evaporator support, (2) electrical heater, (3) boat with material, and (4) evaporator chamber.

worsening of the pressure up to 10^{-4} mbar, staying there for about 23 minutes. After that, the evaporation was stopped.

The final result can be seen in 4.3. After the evaporation we weighted the boat, which had a mass of 472.4 ± 0.1 mg, which meant we evaporated 36.0 ± 0.1 mg of natural Sn.

Figure 4.3: Picture of the targets produced with an aluminium backing.

Cu backing

The second target produced was of natural Sn evaporated over a backing of a Cu film. Both backing and target materials were produced in sequential evaporations: first the backing material was evaporated on top of the glass cover-slip with soap uniformly distributed over it (see figure 4.4), and in the second evaporation, the target was deposited over that backing. This created a structure with four layers as shown in figure 4.5. After evaporation, the targets were carefully placed inside distillate water to dissolve the soap, releasing the backing plus target from the glass. The produced films are left floating at the surface of the water, then with a target holder, we ”fished” the two layers as shown in figure 4.6 (left picture). The target has a hole to let the beam pass through (see right picture on figure 4.6).

Figure 4.4: Before (left picture) and after (right picture) of Cu over glass covered with with soap.

Figure 4.5: Figure representing the layer composition before fishing the targets

The previous target production with Al backing showed that the evaporation of a target onto an already existing backing better guaranteed the physical integrity of the target+backing than the sequential evaporation of the backing and the target in the evaporator. To verify this, we ”fished” some Cu layers into target holders and then evaporated the natural Sn over ”fished” and not ”fished” backings. We prepared three targets and two glasses with a layer of Cu (see figure 4.7). This evaporation was done with the new support, which worked as intended and proved to be an improvement to the overall stability

Figure 4.6: Left picture: target ”fishing”. Right picture: target holder.

of the evaporation process. A molibdenium boat with 99.99 % purity from Goodfellow was used with 98.6 ± 0.1 mg of natural Sn inside. The initial mass of boat+Sn was of 515.2 ± 0.1 mg.

Since there was a problem with the crystal detector, we were unable to monitor the start of evaporation this time. Therefore, we assumed that it would start at the same current value as in the case of the Al backing. The evaporation started at a pressure of 1.1×10^{-6} mbar. In this evaporation, after every increase in current, the pressure value rose up but quickly dropped back down, this continued until a pressure value of 4.3×10^{-6} mbar was reached, where it stayed for near to 15 minutes. After a decrease of pressure back to 2.8×10^{-6} mbar, the current was increased again, but no change in the pressure was observed and the process was stopped, since it was concluded that most of the natural Sn was already evaporated.

After the evaporation, the boat had a mass of 374.6 ± 0.1 mg, meaning that 140.6 ± 0.1 mg of natural Sn was evaporated. Of the 3 targets, one was destroyed while breaking the vacuum, but the other two were in good condition. It was still possible to produce five more targets from the glasses, however these targets were much harder to fish then the Cu alone.

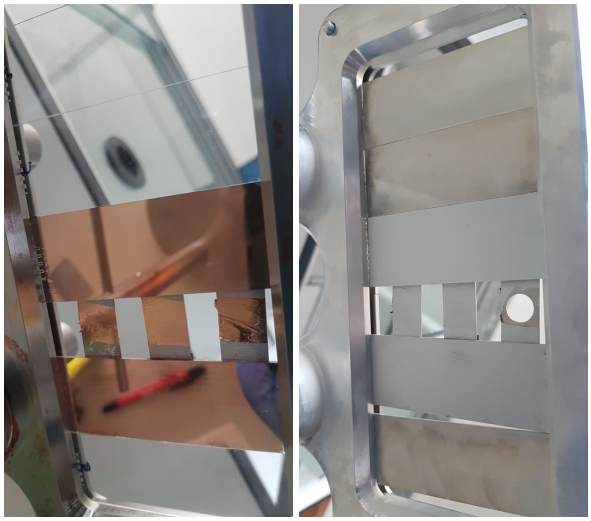

Figure 4.7: Before (left picture) and after (right picture) evaporation of natural Sn on Cu backing.

4.1.2 Target thickness characterization

There are several ways of measuring the target thickness after it has been produced. If the target is made from a single element or from a known material composition, one can weight the backing before and after the deposition of the target layer and from these values estimate the number of atoms produced and divide it by the surface area, which will give us an approximation for the thickness, N_A.

Ion beam techniques like Rutherford Backscattering Spectroscopy (RBS), Particle Induced X-ray Emission (PIXE), and Nuclear Reaction Analysis (NRA) are more robust methods to determine the target thickness. These methods are usually applied before target irradiation. Complementary, the energy lost by α particles from radioactive sources can also be considered to obtain a rough estimate of the thickness of the targets.

Energy loss method

Close to the target evaporation laboratory, we had the chance to first measure the thickness by determining the energy lost by the α-particles in the target. Using this technique, we measured the spectra from a ^{232}U source that emits several high energy α-particles in its decay chain. The experimental setup is made of a vacuum chamber with a PIPS (Passivated Implanted Planar Silicon) detector attached to the hood and a support for a radioactive source that is aligned with the detector at a distance of 1.2 cm from it. This setup is available at FCUL (see figure 4.8) and has been used to measure the thicknesses of targets with several μm, which are much larger than the ones produced in this work.

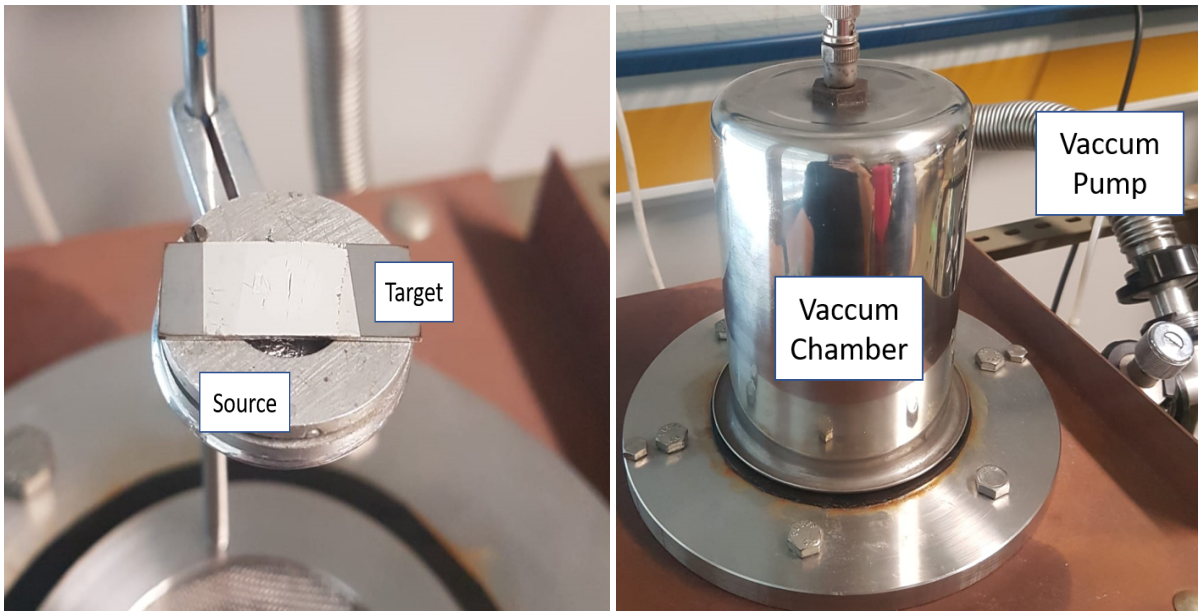

Figure 4.8: Left: View of the target placed in front of the ^{232}U source at the laboratory. Right: External view of the vacuum chamber where the measurements were performed.

A spectrum of the source was acquired in vacuum without the target. This spectrum was used to make the energy calibration using the energies of a few known α-emissions in the decay of ^{232}U. After that, another spectrum was acquired, also in vacuum, with the target placed 5 mm over the source (between the source and the detector). Due to the energy loss of the α-particles in the target, the spectrum peaks are shifted towards lower energies (see figure 4.9). By measuring this energy shift, ΔE, one can determine the target thickness, Δx, using equation 2.5.

It should be noted that in the energy calibration, the effect of the presence of the detector's gold window was also taken into account. For this, the energy values were corrected using the approximation of equation 2.5 for a window thickness of 50 nm and the stopping power in gold for each energy of the emitted α particles.

For the targets evaporated on Al backing, we assumed the thickness value given by GoodFellow of 800 nm and adjusted the total thickness, using the stopping power of Sn until the energy loss was equal

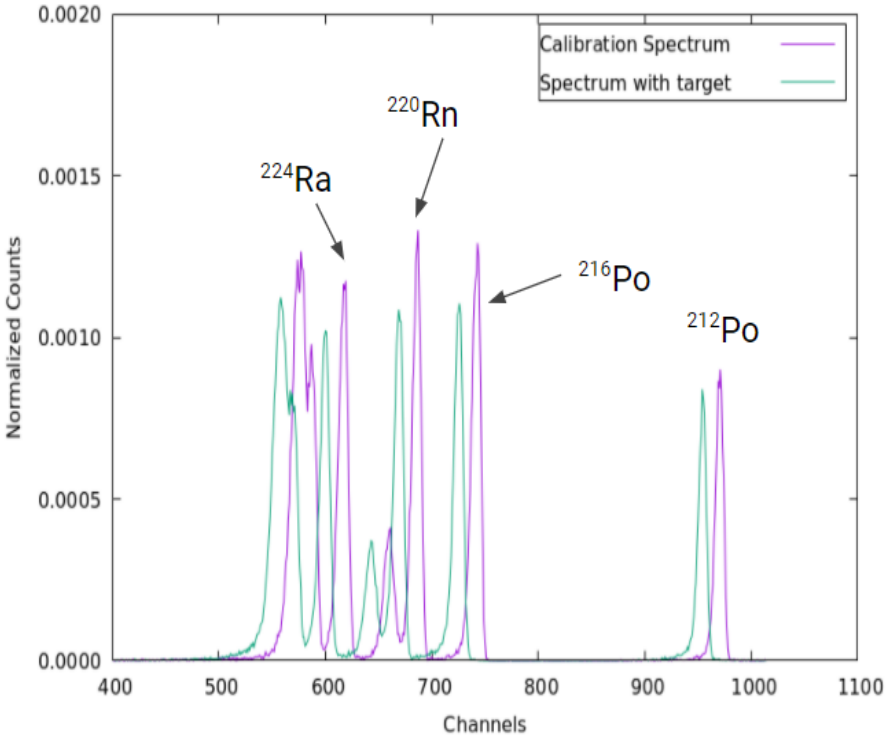

Figure 4.9: Spectra of the ^{232}U decay with and without target between the detector and the source. The α-emissions of the decay products used for the calibration are shown.

to the one measured experimentally. To verify that the linear approximation for the energy loss in the target was applicable, we performed a Monte Carlo simulation using Geant4. For the α-emission of 8.785 MeV, we obtained an energy loss of 0.091 MeV while the simulation resulted an energy loss of 0.087 MeV. This difference is much smaller than the uncertainty of our method, so the approximation is valid. The thickness of the target was determined as the average of the adjusted thicknesses obtained considering the better resolved four α-emissions and the associated uncertainty as the largest difference from this average. The results are shown in table 4.1.

Table 4.1: Thicknesses obtained with the ^{231}U source for the main energies of the α-decay products and for two targets with Al Backing. ΔE is the measured energy loss and Δx is the thickness of Sn in the target.

		Target 1		Target 2	
Source	E_α [MeV]	ΔE [MeV]	$\rho\Delta x_{Sn}$ [μg/cm^2]	ΔE [MeV]	$\rho\Delta x_{Sn}$ [μg/cm^2]
^{224}Ra	5.684	0.15 ± 0.03	15.26	0.14 ± 0.03	14.53
^{220}Rn	6.287	0.15 ± 0.03	45.04	0.14 ± 0.03	36.33
^{216}Po	6.777	0.15 ± 0.03	71.20	0.14 ± 0.03	66.11
^{212}Po	8.785	0.14 ± 0.02	152.6	0.15 ± 0.02	116.24
Average			$(7 \pm 8)\times 10$	Average	$(6 \pm 6)\times 10$

Rutherford backscattering method

Since the uncertainties obtained with this method were too large, a more precise method was needed to measure the very thin targets produced in the evaporator. The RBS (Rutherford Backscattering Spectrometry) method was used with the Van de Graaff accelerator available at the LATR (Laboratory of Accelerators and Radiation Technologies) facility of the CTN/IST. The targets produced with the Al

backing were studied with both protons and α-particles. We studied the scattering of 2 MeV protons and α-particles at a backward angle of 165º. Two of the obtained spectra can be seen in figure 4.10.

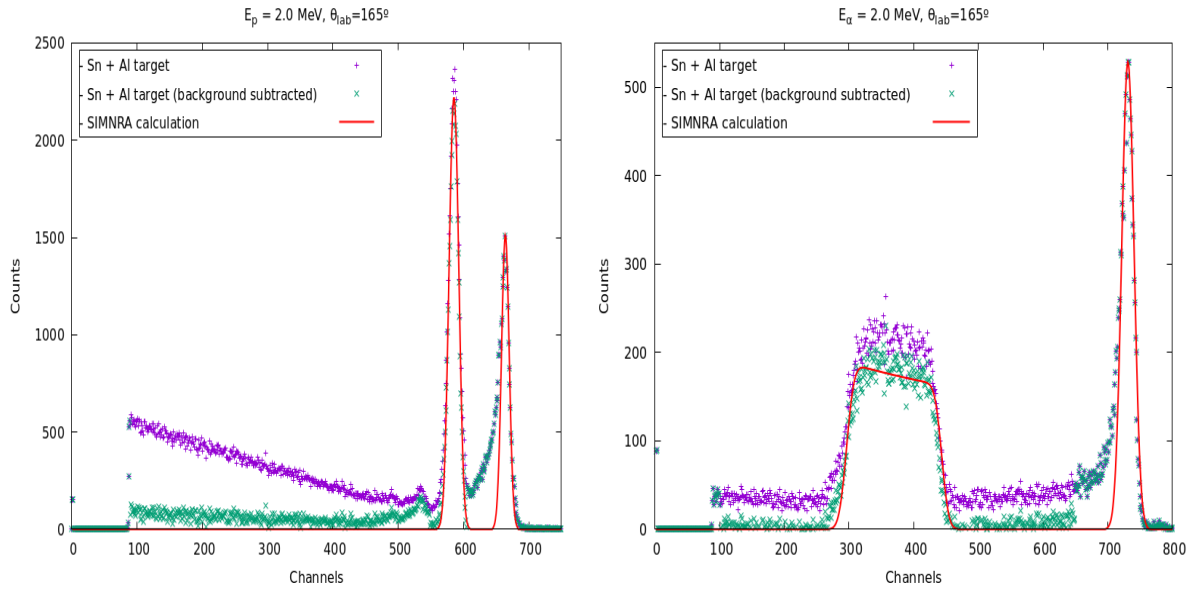

Figure 4.10: Spectra obtained with RBS using protons (left) and α-particles (right) for the same position in the same target.

Using the SIMNRA code [35, 36], the thicknesses of both the Al and Sn were fitted until the theoretical curve described the experimental data. No beam energy spread was considered as the detector has a resolution of $\sim$ 40 keV, which dominates its response. Rutherford cross sections were considered for the interaction of α particles with the target ions. Similar criteria were adopted for the interaction of protons with the Sn nuclei. However, for the description of the signal from the backscattered protons on aluminium, the cross-section measured by M. Chiari et al. [37] was used instead. Table 4.2 shows the thickness values obtained from the RBS analysis.

Table 4.2: Thicknesses obtained with RBS spectra using protons and α-particles for the considered Sn targets with Al backing. The position along the y-axis is given relative to the center of the target.

		p-RBS		α-RBS	
Target	Relat. y [mm]	$\rho\Delta x_{Sn}$ [μg/cm^2]	$\rho\Delta x_{Al} \times 10$ [μg/cm^2]	$\rho\Delta x_{Sn}$ [μg/cm^2]	$\rho\Delta x_{Al} \times 10$ [μg/cm^2]
1	-3	-	-	29 ± 9	20 ± 1
1	-1	39 ± 9	20 ± 1	30 ± 9	18 ± 1
1	1	37 ± 9	20 ± 1	30 ± 9	20 ± 1
1	3	37 ± 9	20 ± 1	-	-
2	-2	45 ± 9	20 ± 1	-	-
2	0	45 ± 9	20 ± 1	-	-
2	2	45 ± 9	20 ± 1	-	-

Two of the produced targets were analyzed using protons, whereas only one of the targets was exposed to an α particle beam. The results are summarized in table 4.2. The targets were analyzed in several positions along the vertical axis. The direct comparison between protons and α-particles was used to estimate an upper limit for the uncertainty in target thickness. This resulted in 9 μg/cm^2 for the Sn targets

and (1×10) μg/cm^2 for the Al backing. The comparison using p-RBS for both analyzed targets, indicated a slight higher content (20% higher) in Sn for the second target. Based on this analysis, we decide to use this target for our first measurement of the ^{118}Sn$(p,\gamma)^{119}$Sb reaction.

Due to time limitations at the Van der Graaff accelerator of the CTN facility, the targets produced with Cu backing could not be characterized with low-energy RBS. However, it was possible to measure the backscattered protons during the activation experiments.

4.2 Activation experiments

The radiative proton capture reactions were performed using the 3 MV Tandem accelerator of the LATR at the CTN/IST. A picture of the accelerator laboratory is shown in figure 4.11. A schematic drawing of the various beam lines present nowadays is shown in figure 4.12.

Figure 4.11: Overview of the 3 MV Tandem accelerator at the time it was installed (picture done before the roof was constructed). Image taken from [38]

Several Faraday cups are positioned at various points of the available beam lines, allowing for an analysis of the current at several key points. In our particular case, the useful Faraday cups are positioned at the entrance of the accelerator (L.E. Switching Magnet), at the exit of the accelerator, after the 90º bending magnet, and at the entrance of our experimental line (after the switching magnet). A comparison of the beam current at various points through the beam line allows us to control the beam properties and maximize the proton flux arriving to the target.

The activation experiments were done in the reaction chamber of the NRA line, as shown in figure 4.12. The targets were placed on a target ladder connected to the chamber header (see figure 4.13). This ladder also allows to change the position of the target inside the chamber.

In the chamber, there are two movable PIPS detectors PD-50-12-100 RM with an active area of 50

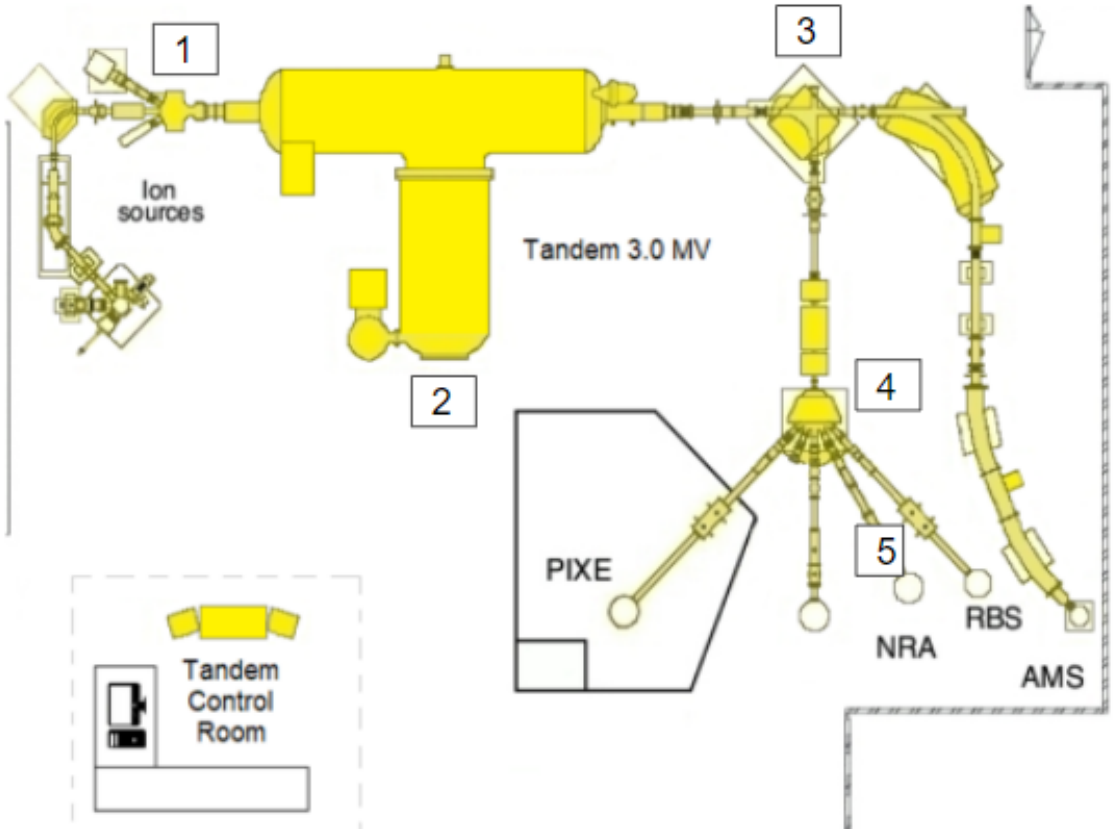

Figure 4.12: Image adapted from [38]. 1- Low energy switching magnet, 2 - high voltage terminal (3 MV Cockcroft-Walton), 3 - 90 º analysing magnet, 4- High energy switching magnet, 5 - NRA chamber line

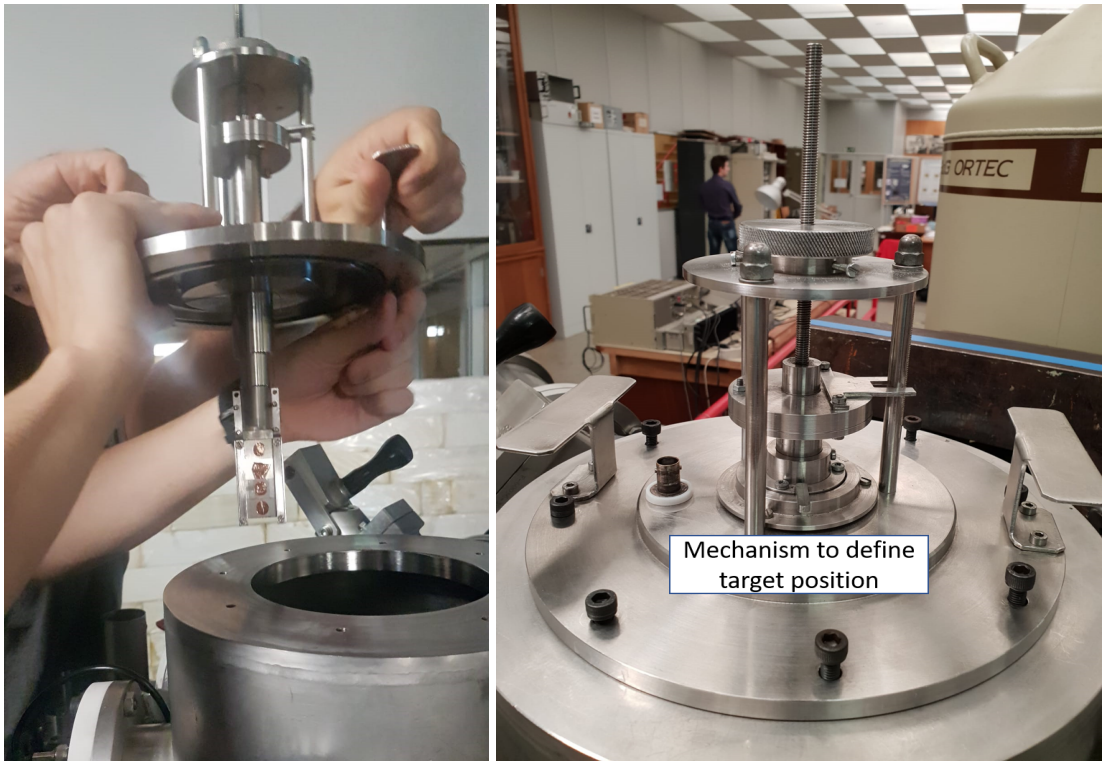

Figure 4.13: left - Picture of the target holder being removed from inside the chamber. Right - Target holder placed inside the chamber.

mm^2, a thickness of 100 μm and a resolution of 12 keV for a α particle with 5.486 MeV of the decay chain of ^{241}Am. The detectors are named from here onwards as MOVD and MOVE. These detectors are placed at a distance of 88 ± 1 mm from the beam spot (see figure 4.14). The angle of the detectors in relation to the beam can be varied and they move jointly, forming a fixed angle of 21º between them. The minimum angle, so as not to interfere with the beam, is $\theta_{lab} = 150$º and this was the angle chosen since it is the one where the RBS peak separation will be maximum. This geometry will provide us with an solid angle of $\Omega = 3.65 \pm 0.08$ msrad, which is equivalent to an geometric efficiency, $\epsilon_g = (2.91 \pm 0.01) \times 10^{-4}$.

Additionally, a HPGe (High-Purity Germanium) detector is placed inside the chamber to measure the prompt γ-emissions. This detector has a cover of aluminium with a thickness of 1 mm, an active area of 128 cm^2, a thickness of 62.6 mm and a resolution of 1.36 MeV keV respectevly for the 1.33 MeV γ decay of ^{60}Co . These detectors are placed at a distance of 88 ± 1 mm from the beam spot (see figure 4.14)

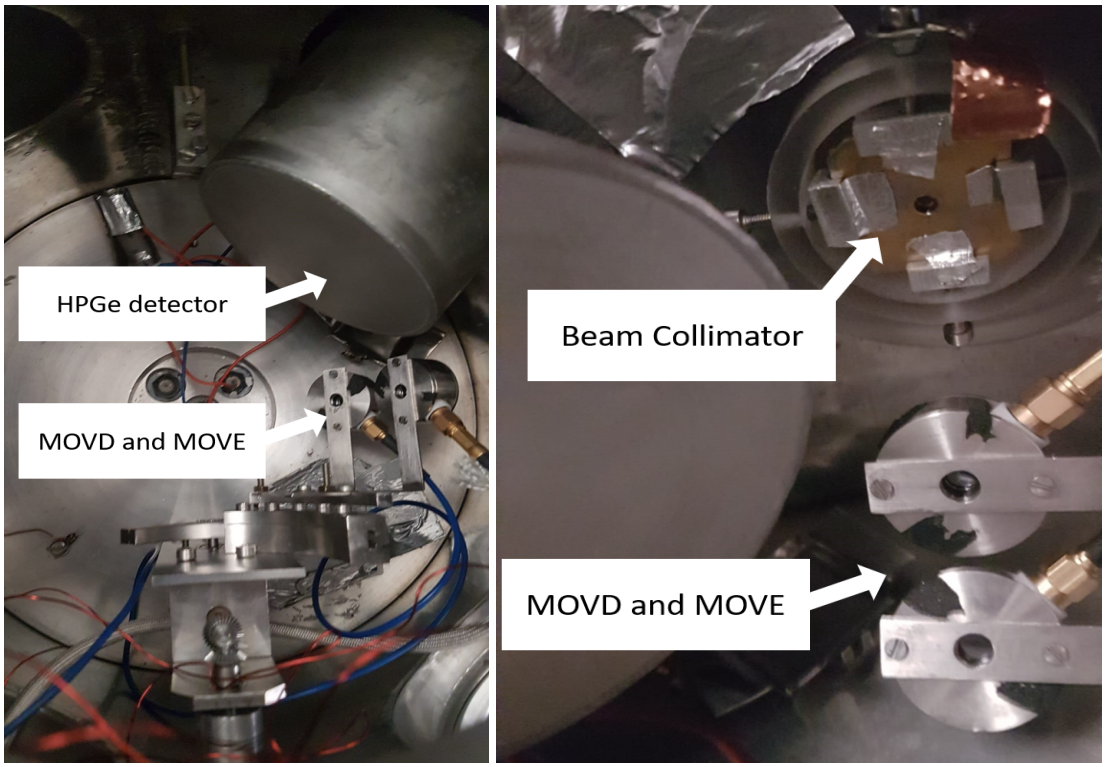

Figure 4.14: Pictures of the inside of the irradiation chamber.

4.2.1 ^{118}Sn activation at E$_p$ = 3.66 MeV

The first activation occurred on August 7, 2020. The Tandem was operated at a stable voltage of $V = 1.8299 \pm 0.0001$ MV. The energy calibration of the tandem considered reads $1.99 \cdot V + 0.015$ [MeV] [39], hence the energy of the proton beam was 3.6555 ± 0.0002 MeV. However, this value only takes into account the uncertainty in the measurement of the Tandem voltage, but due to the optics of the beamline, the beam will also have an energy spread that we need to take into account. This was calculated using the SIMNRA fit of the in-beam RBS spectra and will be discussed in section 4.2.3, for this activation the value obtained was 6 keV. Consider, additionally, that the energy at which the activation occurs is not the same as the beam energy. This is due to the fact that there is energy loss in the target, the activation energy will not be given by a well defined energy but by a range of energies, starting at the beam energy

and ending at the beam energy minus the energy loss. That being said, we will consider the activation energy to be given by the mean value of that energy range and the uncertainty of the energy spread of the beam. For a beam energy of 3.6555 ± 0.0002 MeV and a Sn thickness of (45 ± 9) μg/cm^2 the energy loss will be 2 keV. For this activation, we will then consider an activation energy of $E_p = 3.66 \pm 0.01$ MeV.

Four targets were introduced simultaneously in the support that is calibrated for that chamber (see figure 4.15).

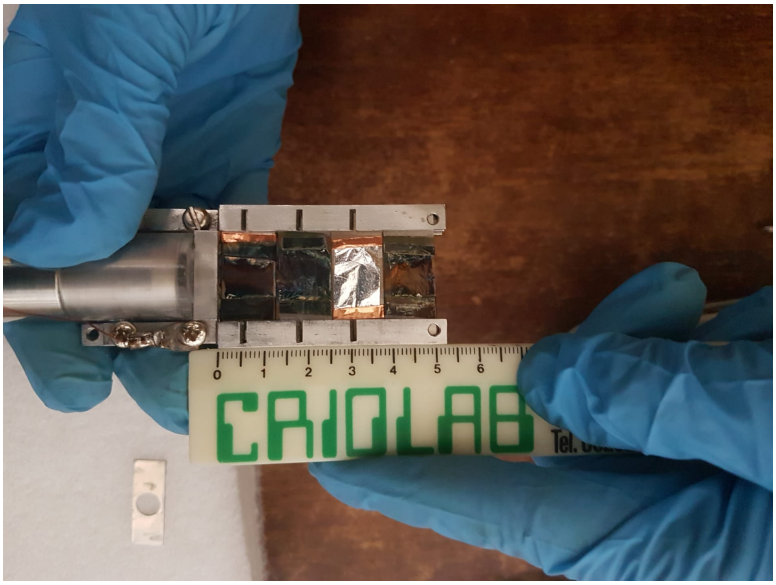

Figure 4.15: Calibrated support for the chamber with 4 targets, 3 of them are natural Sn on an Al backing and one is a target with only Al.

The PIPS detectors were used to perform in-line RBS, allowing the normalization of the measured current. Simultaneously, they also made it possible to control the thickness of the target during the irradiation and allowed the monitoring of the correct position of the beam. By looking at the RBS spectrum, it was possible to check if the beam was hitting the target or the frame. For instance, in the left panel of figure 4.16, we can see the in-beam spectrum when the target holder was placed at 1.1 mm. The measured spectrum shows two peaks coming from the Al backing and Sn target, but the high left-hand tail also shows that the beam is hitting some other thick material, for instance, the target holder. If the position is changed to 0.5 mm, we can see in the right panel of figure 4.16 that now the tail is much smaller, indicating that the beam is only hitting the target+backing.

The irradiation was performed for 11 hours, which is approximately one-third of the half-life of ^{119}Sb and, hence, translates into a production yield around 79 % of the maximum (see equation 2.8).

The current measured before the 90º bending magnet and at the high energy switching magnet was about 125 nA whereas in the chamber only 25 nA were measured, indicating significant beam losses. A high neutron flux was also observed, which corroborates the existence of poor beam alignment in this first irradiation. Nevertheless, the current was relatively constant during the 11 hour period (see figure 4.17, left panel), yet we also divided the irradiation in 3 intervals of constant flux, to verify how it would affect the cross-section calculation, see table 4.3.

After the activation, the target was transported by car about 12 km from CTN/IST to the acquisition setup at FCUL. The transport and positioning of the target took $t_{trans} = 97.93 \pm 0.01$ minutes.

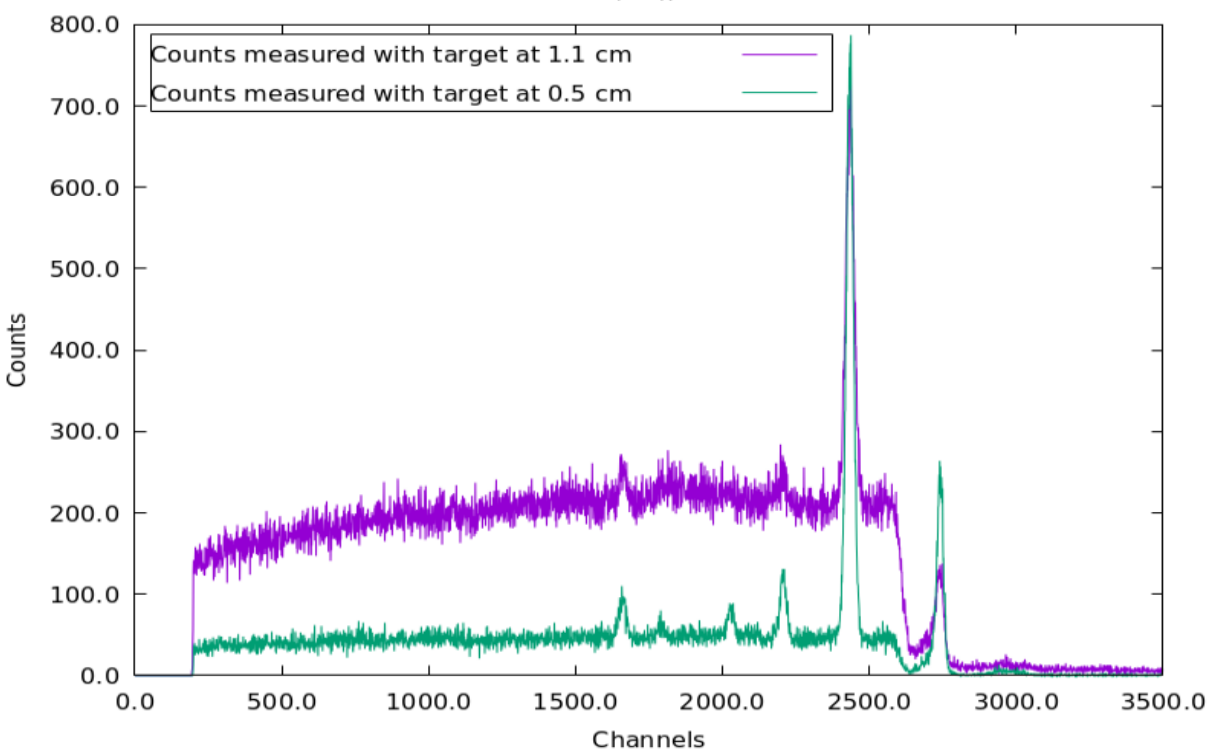

Figure 4.16: In-line RBS spectra when the target holder is at 1.1 mm (purple) and when it is at 0.5 mm (green).

Table 4.3: mean current values considering the total irradiation, and 3 time intervals.

Interval	Time [s]	Current [nA]	Flux [proton$\times 10^{11}$/s]
Total	39681 ± 1	26 ± 2	1.6 ± 0.3
1	12848 ± 1	28 ± 1	1.74 ± 0.09
2	13104 ± 1	27 ± 3	1.7 ± 0.2
3	12705 ± 1	24 ± 5	1.5 ± 0.3

4.2.2 ^{118}Sn activation at E_p = 3.29 MeV

For the second activation, the beam was realigned by the LATR team to correct the problem found in the first irradiation. A week prior to the irradiation, the new alignment was checked at an energy of approximately 1 MeV. For a current of 100 nA at the beamline entrance, a 50-60 nA current was measured at the chamber. Despite part of the beam still being lost, we were confident to increase the current and the irradiation time without producing too many neutrons. In addition, to minimize the risks, the irradiation was carried out during the weekend, with a very small number of people.

This irradiation occurred on October 23 2020, with a setup similar to the one used in the first irradiation experiment. The Tandem was operated at a stable voltage of 1.6545 ± 0.0001 MV, which corresponds to an energy of 3.3065 ± 0.0002 MeV, the beam spread for this irradiation was of 17 KeV. With this beam energy and a Sn thickness of 432 μg/cm^2 the energy loss on the target will be 20 KeV. For this activation, we will then consider an activation energy of $E_p = 3.29 \pm 0.02$ MeV.

Although we expected a higher current for this irradiation, due to the beam being aligned, we noticed that our beam had only a current of 300 nA in the low energy Faraday cup, much less than the usual 10 μA we saw in previous irradiations.

We also detected a possible problem on the charge collection in the chamber, since it was measuring a current of 100 nA, while at the entrance of the beamline the value was 50 nA (see figure 4.17, right

panel). Since we could not be sure of the current value measured at the target, the RBS spectrum was used instead to determine the proton flux.

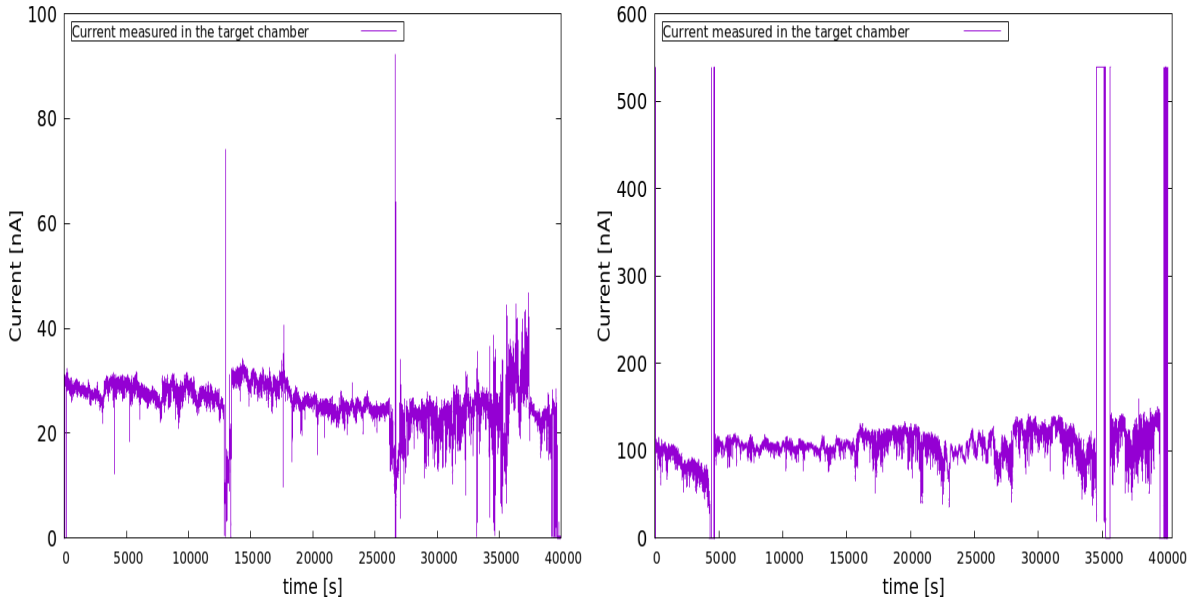

Figure 4.17: Current value measured in the target for the ^{118}Sn activation at E_p = 3.66 MeV (left panel) and at E_p = 3.29 MeV (right panel).

4.2.3 High-Energy p-RBS monitoring

As was explained in the previous section, the in-line RBS allows us to control the thickness of the target during the irradiation. Having that in mind, several spectra were acquired during each irradiation, with time intervals of approximately two hours. Table 4.4 summarizes the spectra acquisition times.

Table 4.4: Acquisition time for all proton backscattered spectra measured during both irradiations.

	Δt [s]	
Run	E_p = 3.29 MeV	E_p = 3.66 MeV
1	9411	3290
2	5573	4254
3	966	7660
4	6144	7240
5	6673	7204
6	6655	7383
7	1686	1295
8	1701	4055
9	2341	

Two of the measured spectra are shown in figure, 4.18, one for the target with aluminium backing (left panel) and the other for the target with Cu backing. In both it is possible to observe distinctively the Sn peaks and the Al and Cu peaks, respectively, as well as backscattered protons from oxygen and carbon. At low energies it is also possible to observe in the left panel spectrum, the peaks corresponding to the (p, p') reaction in aluminium.

To evaluate the behavior of the target during the irradiation, all RBS spectra were analyzed. First, the spectra were normalized to the integral of the aluminium peak or Cu peak, depending on the activation.

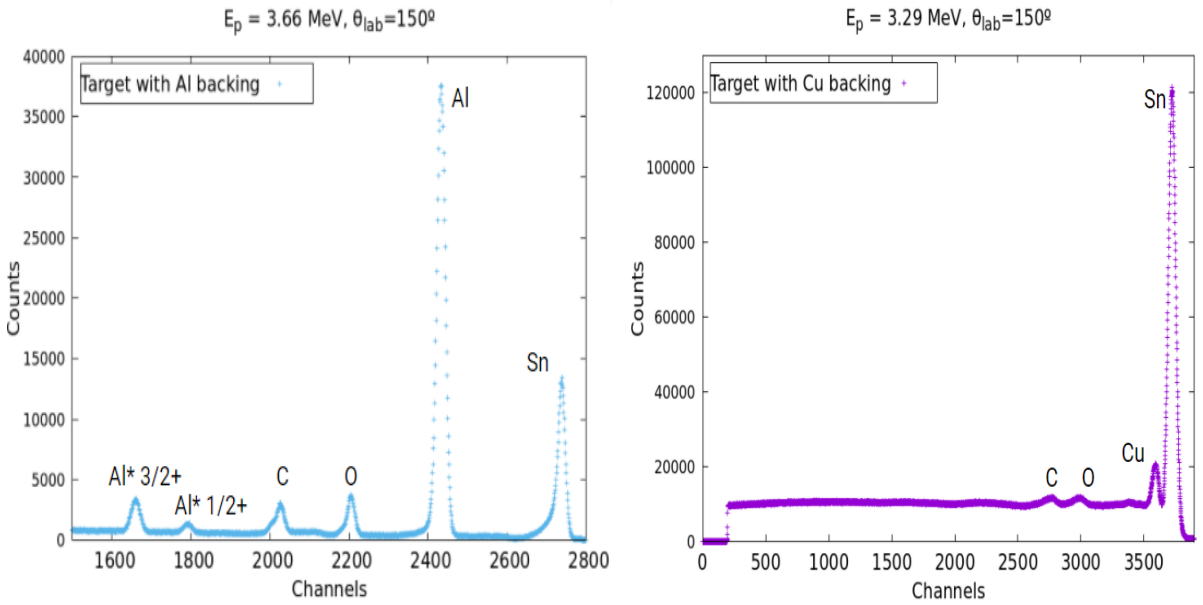

Figure 4.18: Spectra measured at θ_{lab} = 150^o for E$_p$ = 3.29 MeV and Al backing (left) and for E$_p$ = 3.66 MeV and Cu backing (right).

In this way, we could eliminate the dependency in the total charge and check how the thickness of the target changed over the irradiation. Next, the normalized spectra were overlapped, as shown in figure 4.10 to visually compare them. For the aluminium backing, the spectra did not change much, except for the eighth spectrum, this is due to an increase in the beam energy spread, so it was not a change in the target thickness. This is a strong indication that the thickness of the target with Al backing did not change significantly during the irradiation.

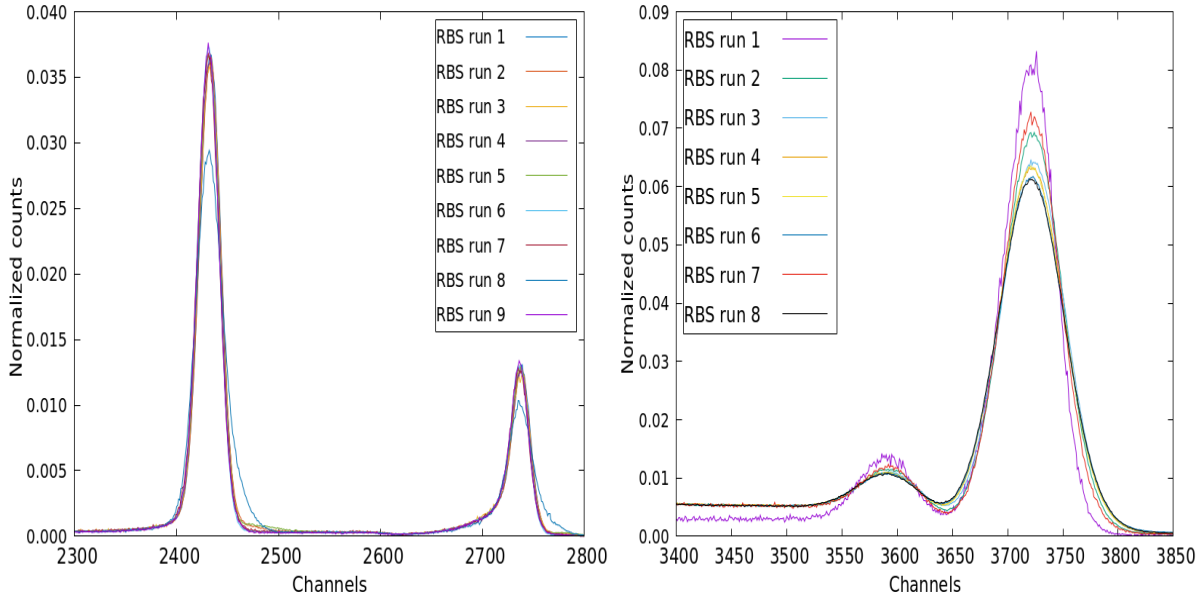

Figure 4.19: All the In-beam RBS spectrum acquired during the first irradiation with Al backing (left) and for the second irradiation with Cu backing (right). The spectra are normalized to the integral of the Al peak and the Cu peak, respectively.

For the Cu backing, the spectra do not overlap again due to different runs having different energy spreads, and not because the thickness of the target changed. This can be concluded because the integral

of the Sn peak does not change significantly over the irradiation time (see table 4.5), which is an indication that the target thickness stays constant.

Table 4.5: Table showing how the integral of the normalized experimental Sn peak does not change significantly over time.

RBS run	$\text{Yield}_{Sn}/\text{Yield}_{Cu}$	$\text{Yield}_{Sn/Cu}/\text{Yield}^{run\#1}_{Sn/Cu}$
1	4.87	1
2	4.78	0.98
3	4.74	0.97
4	4.73	0.97
5	4.71	0.97
6	4.67	0.96
7	4.77	0.98
8	4.68	0.96

With this study, we guarantee that for both the 3.66 MeV and 3.29 MeV activations, the target thickness was constant.

Thickness determination using high energy p-RBS

Additionally, we can consider the measured spectra to estimate the thickness of the irradiated targets, in particular the one produced on a Cu backing. As a first step, we will validate the method using the already measured thickness of the target produced on a Al backing.

The RBS spectra acquired during the 3.66 MeV activation were fitted using the SIMNRA code, assuming a fixed thickness of 45 ± 9 μg/cm^2 and considering a detector's resolution of 25 keV and a contribution from the beam energy spread of 12 keV of FWHM for all runs, except the eighth were it was considered 25 keV. With this FWHM, it is possible to calculate the energy spread of the beam, that will be used for the energy uncertainty, $\sigma_{beam} = FWHM/2.355 \sim 6$ keV, considering the mean value of the FWHM.

From the SIMNRA fit, the incident proton flux was calculated and then compared with the value obtained from the measured data.

The incident particle flux in a time interval t_i can be obtained from equations 2.2 and 2.4,

$$\phi_b^i = \frac{r_i(\theta,\phi)}{4\pi \cdot N_A} \cdot \left(\frac{d\sigma}{d\Omega}\right)^{-1}_{ruth}, \tag{4.1}$$

where the scattered proton rate during a time interval t_i is given by

$$r_i(\theta,\phi) = \frac{N_p^i}{\epsilon_p t_i}, \tag{4.2}$$

where ϵ_p is the PIPS detectors' efficiency and N_p^i is the total number of protons scattered at the angular position of these detectors in the time interval t_i.

Then the incident proton flux is related to the number of backscattered protons by,

$$\phi_b^i = \frac{N_p^i}{\epsilon_p \cdot t_i \cdot 4\pi \cdot N_A} \cdot \left(\frac{d\sigma}{d\Omega}\right)^{-1}_{ruth}, \tag{4.3}$$

Studying the backscattered protons in Sn N_p^i is given by the integral of all counts under the respective

peak and N_a is the aforementioned thickness $\rho\Delta x_{Sn}$ in atoms/cm^2. The results can be found in table 4.6

Table 4.6: Comparison between the incident proton flux calculated from the SIMNRA fit and from the experimental spectra. Also, the comparison between the total number of measured backscattered protons in Sn and fitted with SIMNRA

	$N_p^i \times 10^5$			ϕ_b^i [proton$\times 10^{11}$/s]		
RBS run	Measured	SIMNRA fit	Ratio	Measured	SIMNRA fit	Ratio
1	3.9	3.3	0.84	1.76 ± 0.06	1.46	0.84
2	2.6	2.1	0.83	1.94 ± 0.06	1.60	0.83
3	0.5	0.4	0.79	2.33 ± 0.08	1.81	0.79
4	3.1	2.5	0.81	2.12 ± 0.2	1.69	0.81
5	2.7	2.3	0.82	1.74 ± 0.06	1.41	0.82
6	2.7	2.3	0.85	1.74 ± 0.06	1.46	0.85
7	0.7	0.6	0.84	1.67 ± 0.06	1.38	0.84
8	0.9	0.7	0.81	2.28 ± 0.06	1.82	0.81
9	0.9	0.8	0.87	1.62 ± 0.08	1.38	0.87

There is a difference of about 20 % in the ratio between the incident proton flux calculated from SIMNRA and the calculated from the experiment. At first, we considered that maybe the target had lost thickness before the start of the irradiation. However, this did not look likely. We then considered that the problem might be from the fact that when we are integrating the experimental peak of Sn, we consider the curve created by the incomplete charge collection, but this factor is not present in the SIMNRA code. If we look at figure 4.20, we can see that the SIMNRA fit does not reconstruct the full detector response.

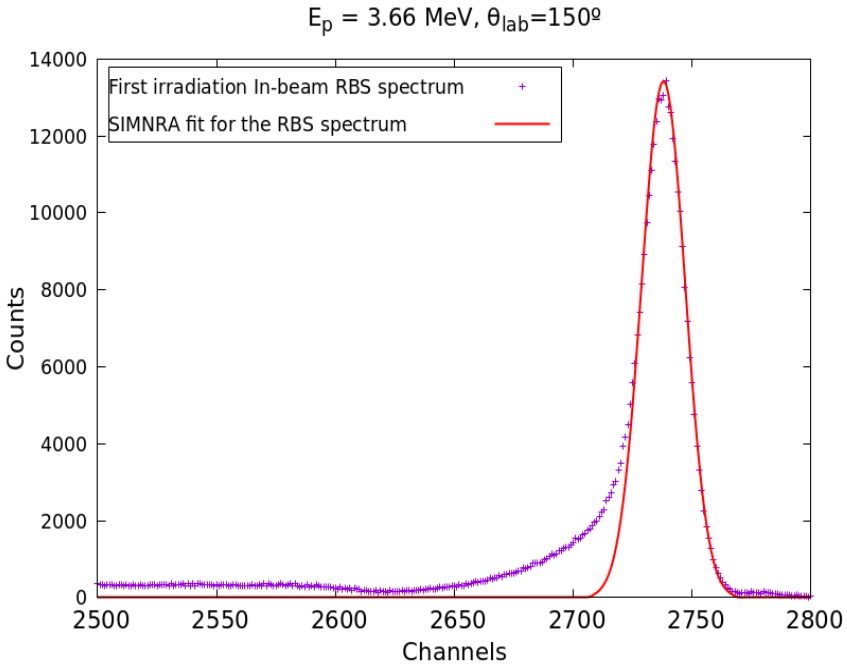

Figure 4.20: Fit of the first RBS spectrum for the first irradiation.

We decided to calculate the ratio between the integral of the experimental peak of Sn and the fitted one, getting the results presented on table 4.6.

We see now that both the ratio calculated for the incident proton flux and the integrals give the same factor, which means that the difference comes from the incomplete charge collection.

In this study, we did not consider the Al peak as a fitting parameter, as the cross-section value at the energy used has not yet been calculated, and we already saw before that the one SIMNRA uses by default is incorrect.

That being said, we are recreating the spectrum very well by assuming a constant thickness equal to the one measured with low-energy RBS with protons. The fact that the two methods were in line with each other provides the confidence to estimate the thickness of the targets evaporated on Cu backing, if the conditions were similar.

As we did not do a RBS study prior to the irradiation, we do not have a starting value for the thickness of the target nor the backing. Using the same detector resolution we used in the prior study, we found the thickness that better fitted the experimental points. From there, knowing that the beam energy spread would be higher in this case, we looked at the pair (thickness, beam energy spread) that would better fit both peaks. Doing this, we can see in figure 4.21, one of the spectra we obtained for the in-beam RBS with the target with Cu backing, giving as a thickness of 432 μg/cm^2 of Sn and of 81.7 μg/cm^2 of Cu, there is no way to calculate the uncertainty for this value as the fit with SIMNRA does not give an uncertainty, and we do not have any other measurement from which to compare.

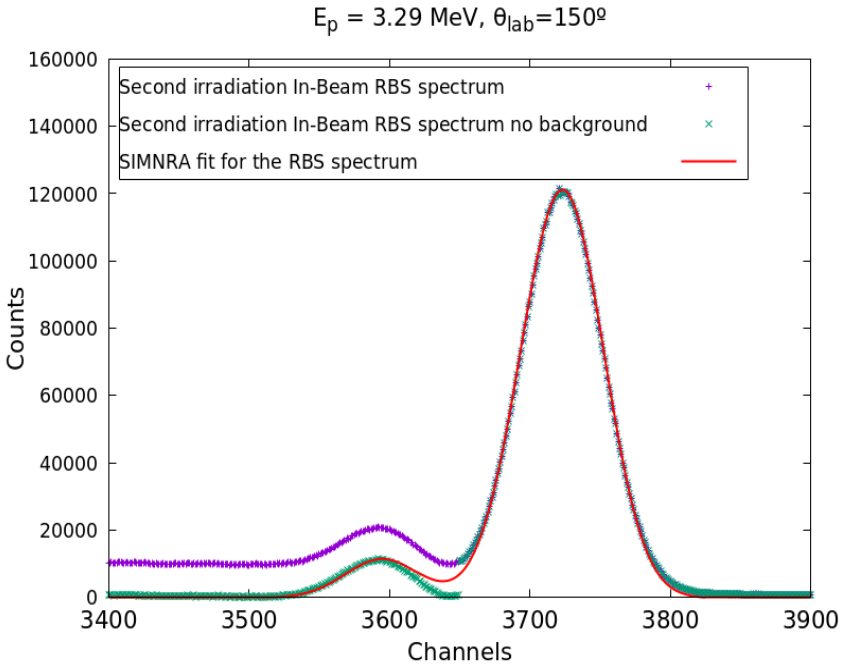

Figure 4.21: Fit of the seventh RBS spectrum for the second irradiation, correcting the background.

In this study, the effect of the incomplete charge collection is not as dominant as we can see in table 4.7.

With these results, we conclude that even though it seems possible to measure the thickness using the in-beam RBS spectra. However, without uncertainty this measurement does not have much of a significance. With the FWHM presented in table 4.7, the calculated beam energy spread will be $\sigma_{beam} = FWHM/2.355 \sim 17$ keV.

Current calculation using in-beam spectra

As we saw previously, the target thickness is constant during irradiation, so the area under the RBS peak is going to be proportional to the proton flux and the Rutherford differential cross-section, so we can

Table 4.7: Comparison between the incident proton flux calculated from the SIMNRA fit and from the experimental spectra.

		ϕ_b^i [proton $\times 10^{11}$ /s]		
RBS run	Energy spread [keV]	Measured	SIMNRA fit	Ratio
1	25	0.250 ± 0.005	0.245	0.98
2	36	3.55 ± 0.05	3.52	0.99
3	46	4.18 ± 0.03	4.15	0.99
4	46	4.39 ± 0.04	4.28	0.97
5	46	4.24 ± 0.04	4.15	0.98
6	46	4.53 ± 0.04	4.38	0.97
7	36	2.8 ± 0.1	2.8	1.00
8	46	4.42 ± 0.07	4.26	0.96

calculate the mean current for each acquired RBS spectrum. Knowing the incident proton flux from table 4.7 and using equations 2.3 and 2.4. The results can be seen in table 4.8.

Table 4.8: Current value calculated using the RBS spectrum acquired during the irradiation.

RBS spectrum	Time [s]	Calculated Current [nA]	ϕ_b^i [proton$\times 10^{11}$/s]
1	3290	4.02 ± 0.07	0.250 ± 0.005
2	4254	57.1 ± 0.8	3.55 ± 0.05
3	7660	67.4 ± 0.6	4.18 ± 0.03
4	7240	70.7 ± 0.6	4.39 ± 0.04
5	7204	68.2 ± 0.6	4.24 ± 0.04
6	7383	72.9 ± 0.6	4.53 ± 0.04
7	1295	45 ± 2	2.8 ± 0.1
8	4055	71 ± 1	4.42 ± 0.07

We can see that the current value is not constant during the irradiation. Moreover, the current values are not the same as the one we measured during the irradiation, this confirms that there is a problem with the charge collection in the chamber.

4.3 Acquisition of the decay spectra

The decay acquisition setup with two detectors facing each other with the target is shown in figure 4.22. The target was placed as close as possible to the detectors' windows, reducing the distance the particles have to travel, which decreased the angular dispersion and increased the geometrical efficiency. Since the targets are positioned in a holder that has a hole, particles leaving the target from the front and back can be detected with two detectors in opposite sides.

We used the XR-100SDD detector from Amptek and the SXD15M-150-500 detector from Canberra, each coupled to a PX5 interface also from Amptek that digitizes the signal to be read by the computer. The characterization of the detectors was addressed in chapter 3. The DPPMCA software from Amptek was used to control the hardware acquisition parameters and register the spectra.

The experimental setup, however, does not ensure that the targets from different activations are positioned at the same distance from the detector, which increases the target transverse and axial offset error.

Figure 4.22: Decay acquisition setup at FCUL with two detectors: the XR-100SDD (left side) and the SXD15M-150-500 (right side).

4.3.1 Decay acquisition method

There are two ways to analyze the data to obtain the number of isotopes created at the end of irradiation, N_D^{irr}), from the emission peak areas. One is to obtain a spectrum accumulated over a long period of time, say $t_{acqui} \sim 10 \times t_{1/2}$. From N_{peak} of this acquisition, we obtain the number of decays, N_{decay}, using equation 2.13 and from that the number of isotopes using equation 2.11. In the case of ^{119}Sb this implies an acquisition time of two weeks or more.

A more practical way is to follow the temporal evolution of the peak areas and make the fit of equation 2.10 to the data. This approach allows to track more closely the contribution of the other reaction products. To do this, we need to acquire over n intervals of time t_{acqui}/n and obtain for each spectrum the peak area. The number of intervals to be used and the total time of acquisition depends on the degree of activation of the target.

For a weak activation, we need to accumulate for longer periods of time to be able to apply the previous method. It is therefore better and more practical to fit the data using equation 2.11 to the number of decays instead of the source activity. The acquisition method is the same, acquire over n intervals of time t_{acqui}/n, but the way the data is plotted is different, as now each point is the sum of all peak areas measured before. In our study, we will focus on this approach as our expected signal is rather weak.

There were two acquisition periods, both of them starting exactly after arriving at FCUL with the irradiated targets. The acquisition was done in 30 minute intervals for a period of approximately 10 days, 240.67 ± 0.02 hours, for both irradiations. The analysis of the collected data will be done in chapter 5.

Chapter 5

Natural Sn analysis

In this work, we used natural Sn to develop and optimize the experimental methodologies and data analysis that will be used with targets of pure ^{118}Sn in the future. A major disadvantage of using X-ray emissions in the Activation Method is that they are characteristic of the atom. Hence, if the target consists of several stable isotopes of the same element, different products with the same characteristic X-ray emissions will be created during the irradiation. If these isotopes decay by electron capture with similar half-life, it will be almost impossible to differentiate between them, as the total number of decays will be described by an overlap of the different individual decays. Another disadvantage is that several reactions can lead to the production of the same isotope. For example, the (p,n) reaction on ^{119}Sn also produces ^{119}Sb, which can lead to an overestimation of the cross-section of the (p, γ) reaction. Even though it's not possible to eliminate completely these disadvantages, it is possible to estimate their effect on our analysis to correct them.

In table 5.1, we can find the abundances of several isotopes of Sn. By looking at the table, we can conclude that ^{118}Sn has the second highest abundance of all the isotopes in natural Sn, which will directly impact the reaction probability. The isotope with the highest abundance, ^{120}Sn, either creates ^{121}Sb, via (p, γ) reaction, which is a stable isotope, or creates ^{120}Sb, via the (p, n) reaction, which has a half-life much smaller than ^{119}Sb. Therefore, after 3 to 5 half-lives of this isotope, we can ignore the decay in the analysis and, even more so, in the case of ^{118}Sb produced by the capture reaction on ^{117}Sn. In addition, the (p, n) reaction in ^{120}Sn only opens at (3.463 ± 0.007) MeV and, hence, as long as the beam energy is below this value, no ^{120}Sb will be produced via this channel.

The only other reaction capable of producing ^{119}Sb is the (p,n) reaction on ^{119}Sn. However, the abundance of this isotope is about three times smaller than the abundance of ^{118}Sn and the cross-section for ^{118}Sn(p, γ) reaction, obtained with the TALYS code version 1.7 [40, 41] (see figure 5.1), using the standard parameters, is one order of magnitude larger than the cross-section for the ^{119}Sn(p,n) reaction in the energy range of interest. Thus, it's not expected a significant contribution from this channel when using natural Sn. However this theoretical calculation should be verified experimentally using targets with different isotopic distribution.

The use of natural Sn makes it possible to analyse the (p, γ) reaction on ^{116}Sn that produces ^{117}Sb. This radioactive product has a half-life very different from ^{119}Sb, allowing to separate the contribution of each one to the total decay. In this case, the total decay is $N_{decay} = N_{decay}(^{119}\text{Sb}) + N_{decay}(^{117}\text{Sb})$, where each term is given by equation 2.11. If we consider the half-lives as a fixed parameter taken from the literature, then $N_D(^{119}\text{Sb})$ and $N_D(^{117}\text{Sb})$ are the only free parameters that can be determined with a fit to the experimental data. This means that we are able not only to calculate the cross-section for $^{118}\text{Sn}(p, \gamma)^{119}\text{Sb}$ but also for $^{116}\text{Sn}(p, \gamma)^{117}\text{Sb}$. The latter has already been measured, as we mentioned

before in section 2.2.3, which means we can use it to validate our method.

Table 5.1: Table with the relative abundances of stable isotopes in natural Sn and their (p, γ) reaction products half-lifes.

Isotope	Abundance [%]	Reaction product	$t_{1/2}$
^{116}Sn	14.54 ± 0.09	^{117}Sb	2.80 ± 0.01 (h)
^{117}Sn	7.68 ± 0.09	^{118}Sb	3.6 ± 0.1 (min)
^{118}Sn	24.22 ± 0.09	^{119}Sb	38.2 ± 0.2 (h)
^{119}Sn	8.59 ± 0.09	^{120}Sb	15.89 ± 0.04 (min)
^{120}Sn	32.58 ± 0.09	^{121}Sb	stable

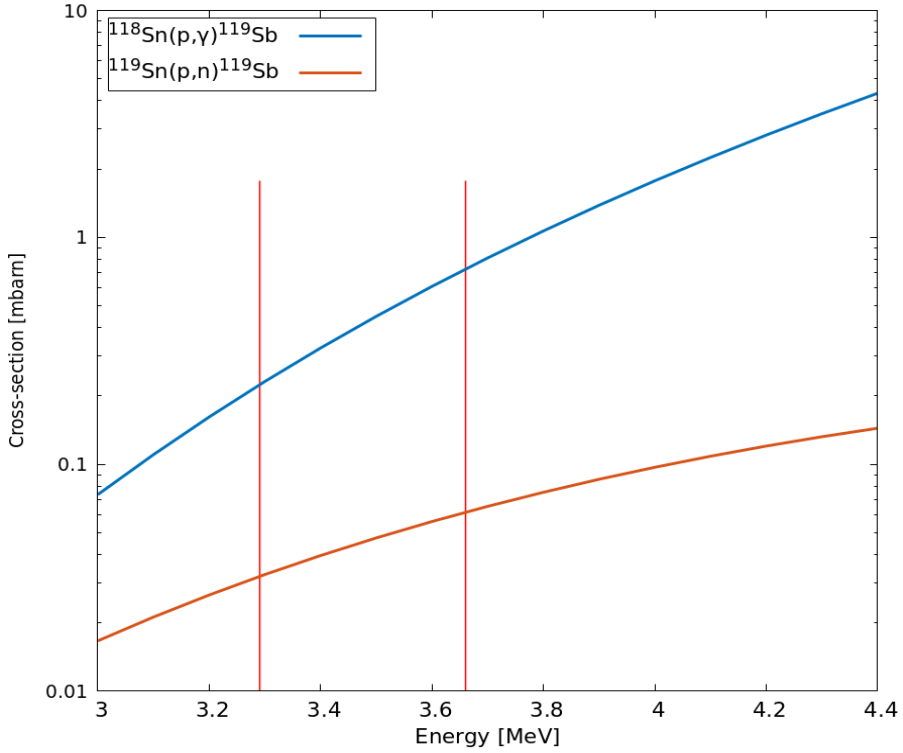

Figure 5.1: ^{119}Sn$(p, n)^{119}$Sb and ^{118}Sn$(p, \gamma)^{119}$Sb cross-sections obtained with TALYS. The red vertical lines represent the energies at which irradiations were performed in the framework of this Master Thesis

5.1 Decay acquisition study

5.1.1 Activation at E_p = 3.66 MeV

The first acquisition was done for the target with 45 μg/cm^2 thickness of Sn with an aluminium backing (see section 4.1.2) activated with protons of energy 3.66 MeV. The spectra were acquired only with the detector (XR-100SDD) facing the the target, since the other detector (SXD15M-150-500) facing the Al backing showed a very large dead time (99.9%). This was due to the very low activity of the irradiated target, further attenuated by the backing that considerably reduced the photons reaching the detector. In this regime, the dead time behaviour is random. This problem was solved in the second acquisition by completely removing the detection threshold.

The 10-day accumulated spectrum for the first acquisition is shown in figure 5.2. The top panel shows the full spectrum, where the ^{119}Sb γ emission peak and the Kα, Kβ_{13}, and Kβ_2 Sn lines are clearly separated. The lower panel shows the details of the energy region up to 10 keV, where the detector's efficiency is higher. In this region, one can identify the Lα and Lβ lines of Sn as well as the characteristic lines of elements present in the target holder, like iron and copper.

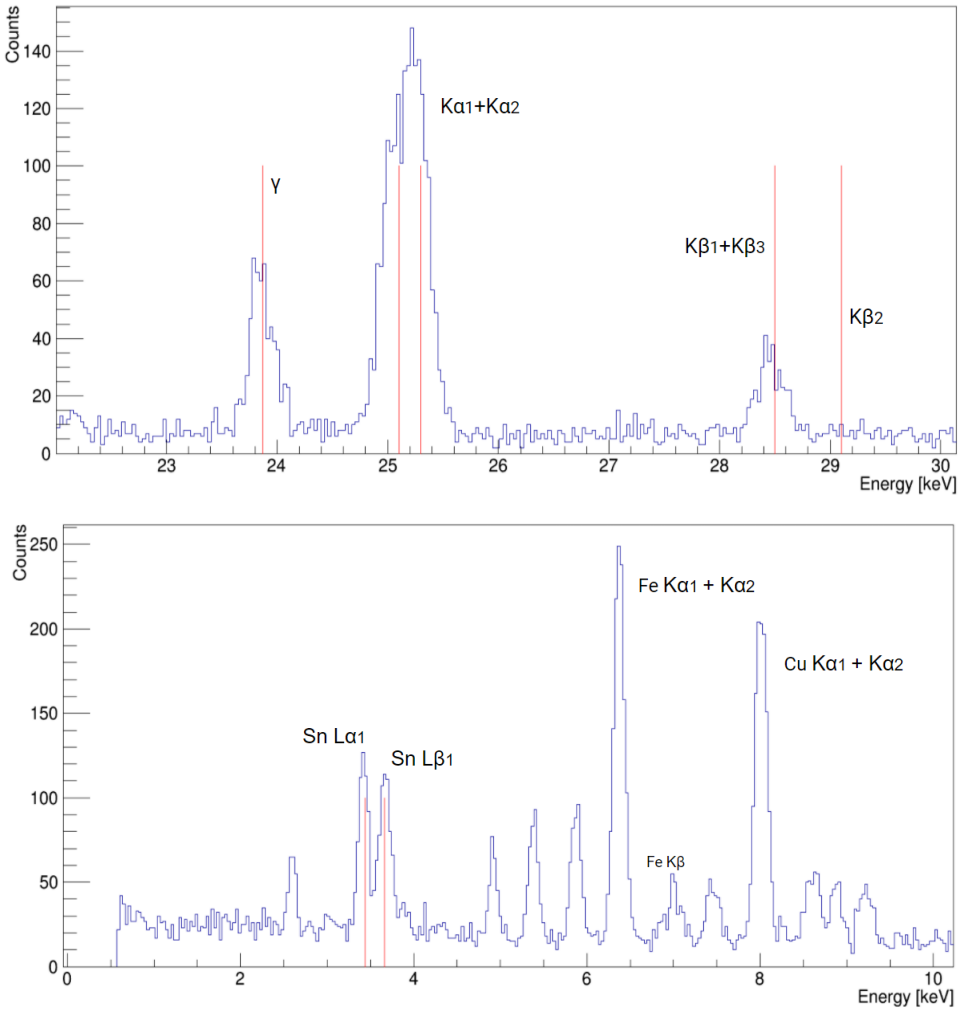

Figure 5.2: X-ray spectra acquired after the irradiation at E_p = 3.66 MeV. The upper panel shows the characteristic γ decay line of ^{119}Sb and the high-energy X-rays of Sn. The lower panel presents the low energy region of the spectrum, where the Sn characteristic Lα and Lβ lines are observed together with other X-rays emitted by other elements present in the setup.

The ability to resolve the Sn L-lines opens the possibility to use these emissions also in the analysis of the number of decays. The presence of the Sn L-lines in the spectrum results from two distinct mechanisms in the decay of ^{119}Sb: the electronic capture of L-shell electrons and the decay of the 23.9 keV state in ^{119}Sb by internal conversion of L-shell electrons. Since the probabilities for these processes are not tabulated for the ^{119}Sb decay and their calculation is outside the scope of this work, our analysis focused on γ-emission and the X-ray K-lines of ^{119}Sn.

Figure 5.3 shows the time evolution of the accumulated peak areas every 30 minutes for each of these emissions. Since the γ-emission is unique to the ^{119}Sb decay, it can be used to determine the decay constant $\lambda(^{119}\text{Sb})$ by fitting the data to

$$N^{\gamma}_{peak}(t) = N^{\gamma}_{peak}(^{119}\text{Sb}) \cdot \left[1 - e^{-\lambda(^{119}\text{Sb})t}\right], \tag{5.1}$$

and compare it with the value of $(3.02 \pm 0.02) \times 10^{-4}$ min^{-1} obtained using the values from table 5.1 and $\lambda = ln(2)/t_{1/2}$. The fitted value of $N^{\gamma}_{peak}(^{119}\text{Sb})$ will be used to validate the Activation Method with X-rays.

For the X-ray emissions, the total number of detected X-rays contains two contributions:

$$N^{X}_{peak}(t) = N^{X}_{peak}(^{117}\text{Sb}) \cdot \left[1 - e^{-\lambda(^{117}\text{Sb})t}\right] + N^{X}_{peak}(^{119}\text{Sb}) \cdot \left[1 - e^{-\lambda(^{119}\text{Sb})t}\right], \tag{5.2}$$

where $N^{X}_{peak}(^{117}\text{Sb})$ and $N^{X}_{peak}(^{119}\text{Sb})$ are the total number of detected X-rays from ^{117}Sb and ^{119}Sb, respectively. Fixing the values of $\lambda(^{117}\text{Sb}) = (0.193 \pm 0.005)$ min^{-1} from table 5.1 and of $\lambda(^{119}\text{Sb}) = (2.8 \pm 0.2) \times 10^{-4}$ min^{-1} from the γ-emission fit, we again used the fitting capabilities of gnuplot, to obtain the two maximum peak areas. However, the uncertainties presented by the fit were too low and to calculate the error from this fit made a C++ code to study how the χ^2_{norm} changed with the fitted parameters. We consider that the error would be given by the difference between the fitted parameter and the value of the parameter when the χ^2_{norm} changed by one unit.

All fitted parameters and corresponding uncertainties can be found in table 5.2

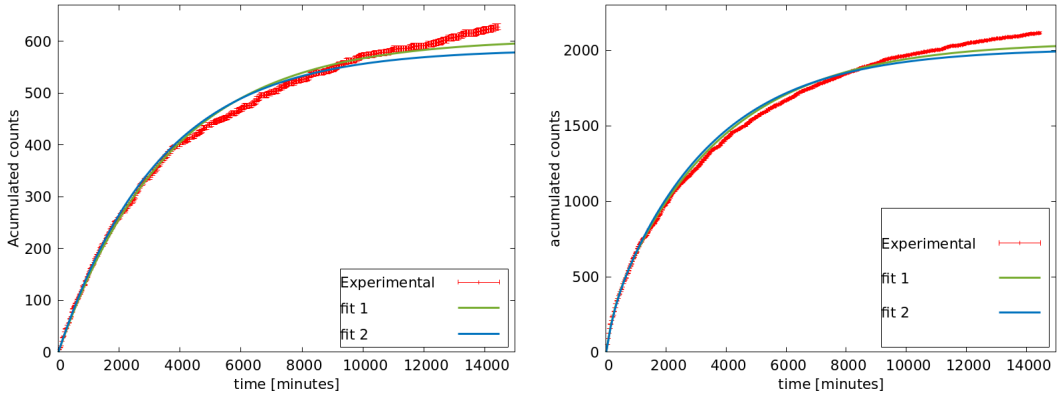

Figure 5.3: Accumulation curves obtained in the acquisition of the target activated at E$_p$ = 3.66 MeV for the γ-emission (left panel) and Kα line (right panel). Fit 1 corresponds to the fitted curve obtained with $\lambda(^{119}\text{Sb}) = (2.8 \pm 0.2) \times 10^{-4}$ min^{-1} as a free parameter and Fit 2 corresponds to fitted curve obtained with the fixed value of $\lambda(^{119}\text{Sb}) = (3.02 \pm 0.02) \times 10^{-4}$ min^{-1} calculated from table 5.1. The K-lines accumulation curves were fitted using the fixed value of $\lambda(^{117}\text{Sb}) = (4.13 \pm 0.01) \times 10^{-3}$ min^{-1} also calculated from table 5.1.

Table 5.2: Parameters obtained by fitting the accumulation curves. For details see text.

		N_{peak} (10^3)		
	λ (^{119}Sb) [10^{-4}·min^{-1}]	^{119}Sb γ	^{119}Sb Kα	^{117}Sb Kα
Fit 1	2.8 ± 0.2	0.61 ± 0.03	1.85 ± 0.03	0.21 ± 0.03
Fit 2	3.02 ± 0.02	0.58 ± 0.02	1.82 ± 0.05	0.19 ± 0.05

The fitted and the literature values of $\lambda(^{119}Sb)$ are very different. Indeed, the γ-emission accumulation curves using the fitted value and the literature value are very similar in the first 2000 minutes, but after that they start to diverge (see left panel of figure 5.3). This divergence can not be attributed to the presence of other radioisotopes, since that peak is characteristic of ^{119}Sb and there are no other peaks in this region. Furthermore, the same behaviour affects the Kα line accumulation curve, indicating that

might be a problem with the data acquisition or with the half-life of ^{119}Sb obtained from the literature. The analysis of the activation data at 3.29 MeV in section 5.1.2 confirmed the half-life literature value of ^{119}Sb, thus the discrepancy is due to data acquisition problems.

To further investigate these data, the measured γ-emission and Kα line intensity ratio was compared with tabulated values,

$$\text{Ratio} = \frac{I^{\text{K}\alpha}_{peak}}{I^{\gamma}_{peak}} = \frac{N^{\text{K}\alpha}_{peak}}{N^{\gamma}_{peak}} \cdot \frac{\epsilon_{\gamma}}{\epsilon_{\text{K}\alpha}} \tag{5.3}$$

The intensities per decay of the γ-emission and Kα line are shown in table 2.1.

The efficiency of the detector was simulated for an isotropic point source in vacuum (see section 3.2.2). However, a more realistic simulation of our setup needs to consider the source as being extended over the backing. Figure 5.4 compares the efficiency simulated for a point source with the efficiency simulated for a cylindrical Sn source with a 0.062 ± 0.014 μm thick Al backing (calculated from section 4.1.2). The simulation was done for the XR-100SDD detector considering that it was positioned at 5 mm from the source. The whole geometry was immersed in air.

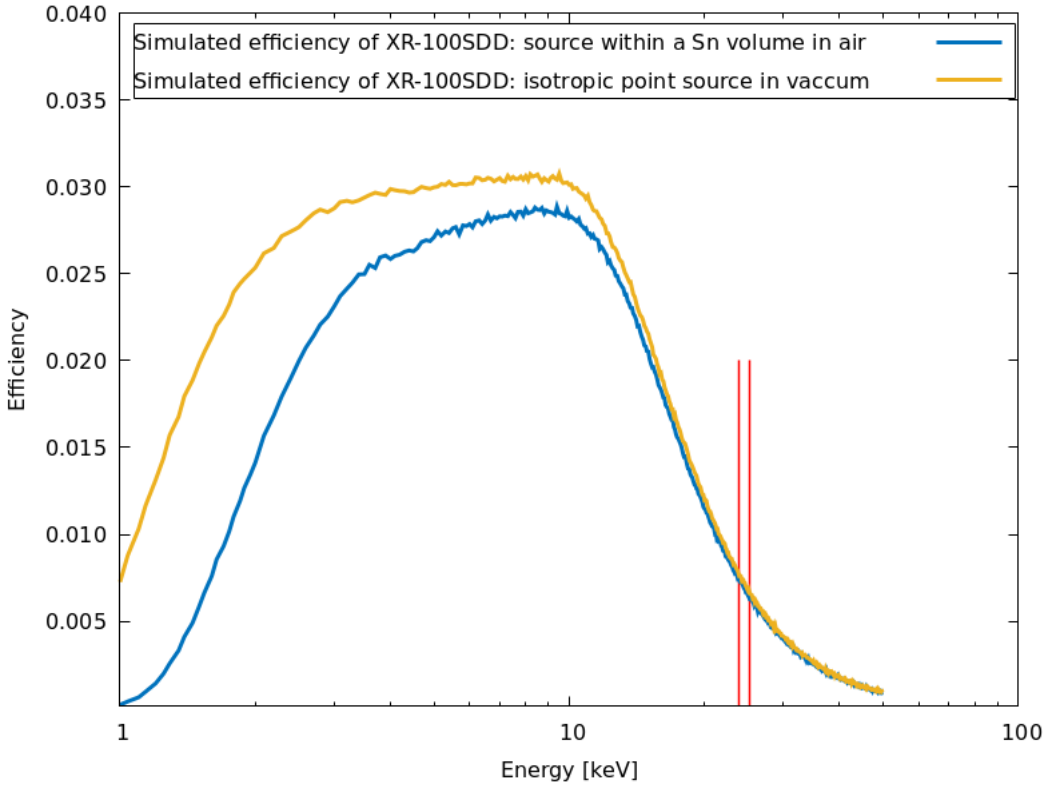

Figure 5.4: Efficiency curve of the XR-100SDD detector. Simulations were done considering an isotropic point source in vacuum (orange) and considering that the source is a cylindrical volume of the target in air. The red vertical lines are positioned at the γ-emission and Kα-line energies

The measured intensity ratios taking into account the corrected efficiencies are shown in table 5.3. Remarkably, the intensity ratio obtained using $\lambda(^{119}\text{Sb}) = (2.8 \pm 0.2) \times 10^{-4}$ min^{-1} is similar to the one obtained with the fixed value of $\lambda(^{119}\text{Sb}) = (3.02 \pm 0.02) \times 10^{-4}$ min^{-1} from the literature. However, the uncertainty in the method is dominated by the large uncertainty in the geometrical efficiency due to the relative positioning of the source and detectors in the acquisition setup. To decrease the overall uncertainty in this analysis, it would be desirable to build a better support to fix the source and the detectors.

Table 5.3: Corrected efficiencies for the target with aluminium backing and Kα/γ intensity ratio. Fit 1 and 2 correspond to the fitting described in figure 5.3. For details see text.

		Kα/γ		
$\epsilon_\gamma \times 10^{-3}$	$\epsilon_{K\alpha} \times 10^{-3}$	Fit 1	Fit 2	Tabulated
7.4 ± 0.2	6.3 ± 0.2	3.6 ± 0.3	3.6 ± 0.3	3.6 ± 0.1

5.1.2 Activation at Ep= 3.29 MeV

The second acquisition was done for the target with a 432 μg/cm^2 thickness of Sn with a copper backing (see section 4.1.2) activated with protons of energy 3.29 MeV. In this acquisition, it is possible to observe in figure 5.5 that the signal in our detectors was higher. This was expected as the thickness of the Sn target and the irradiation current was higher than for the first irradiation.

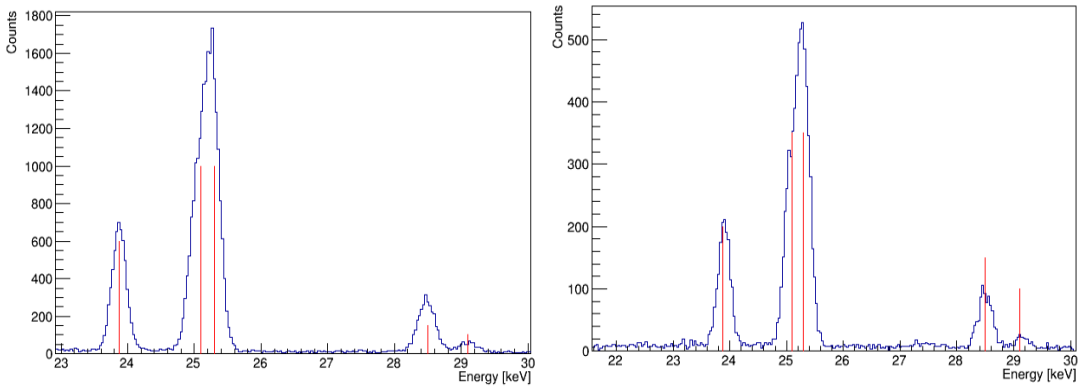

Figure 5.5: X-ray spectra acquired after the irradiation at E$_p$ = 3.29 MeV for the XR-100SDD (left) and SXD15M-150-500 (right) detectors.

The yields of the γ, Kα, and the Kβ_{13} peaks were determined for every spectrum, producing the accumulation curves shown in figure 5.6. Treating $\lambda(^{119}\text{Sb})$ as a free parameter, the parameters shown in 5.4 were obtained. The fit reproduces quite well the value of $\lambda(^{119}Sb)$ given in the literature, which indicates there was a data acquisition problem with the acquisition at higher proton energy first acquisition. Now the curves fit rather well the experimental points.

Table 5.4: Parameters obtained by fitting the accumulation curves for the second acquisition. The fit was done considering $\lambda(^{119}\text{Sb})$ as a free parameter and using the fixed value of $\lambda(^{117}\text{Sb}) = (4.13 \pm 0.01) \times 10^{-3}$ calculated from table 5.1.

		N_{peak} ($\times 10^3$)				
Detector	λ (^{119}Sb) [10^{-4}·min^{-1}]	γ	^{119}Sb Kα	^{117}Sb Kα	^{119}Sb Kβ_{13}	^{117}Sb Kβ_{13}
XR-100SDD	3.0± 0.1	6.11 ± 0.09	18.9 ± 0.2	3.4 ± 0.1	2.72 ± 0.05	0.40 ± 0.04
SXD15M-150-500	3.0± 0.1	1.72 ± 0.05	5.4 ± 0.1	0.8 ± 0.1	0.81 ± 0.01	0.06 ± 0.02

The corrected efficiency was simulated considering now the target with a copper backing. In this acquisition, the efficiency for the SXD15M-150-500 detector was also simulated, considering additionally 91.2 nm of copper thickness because this detector was facing the backing. The XR-100SDD detector was positioned at 3 mm of the target and the SXD15M-150-500 detector was positioned at 5 mm. The simulation results can be seen in figure 5.7. The pronounced drop in the efficiencies around the 3.9 keV energy, corresponds to the L_3 absorption edge in Sn [42]. This drop was not noticeable in the previous

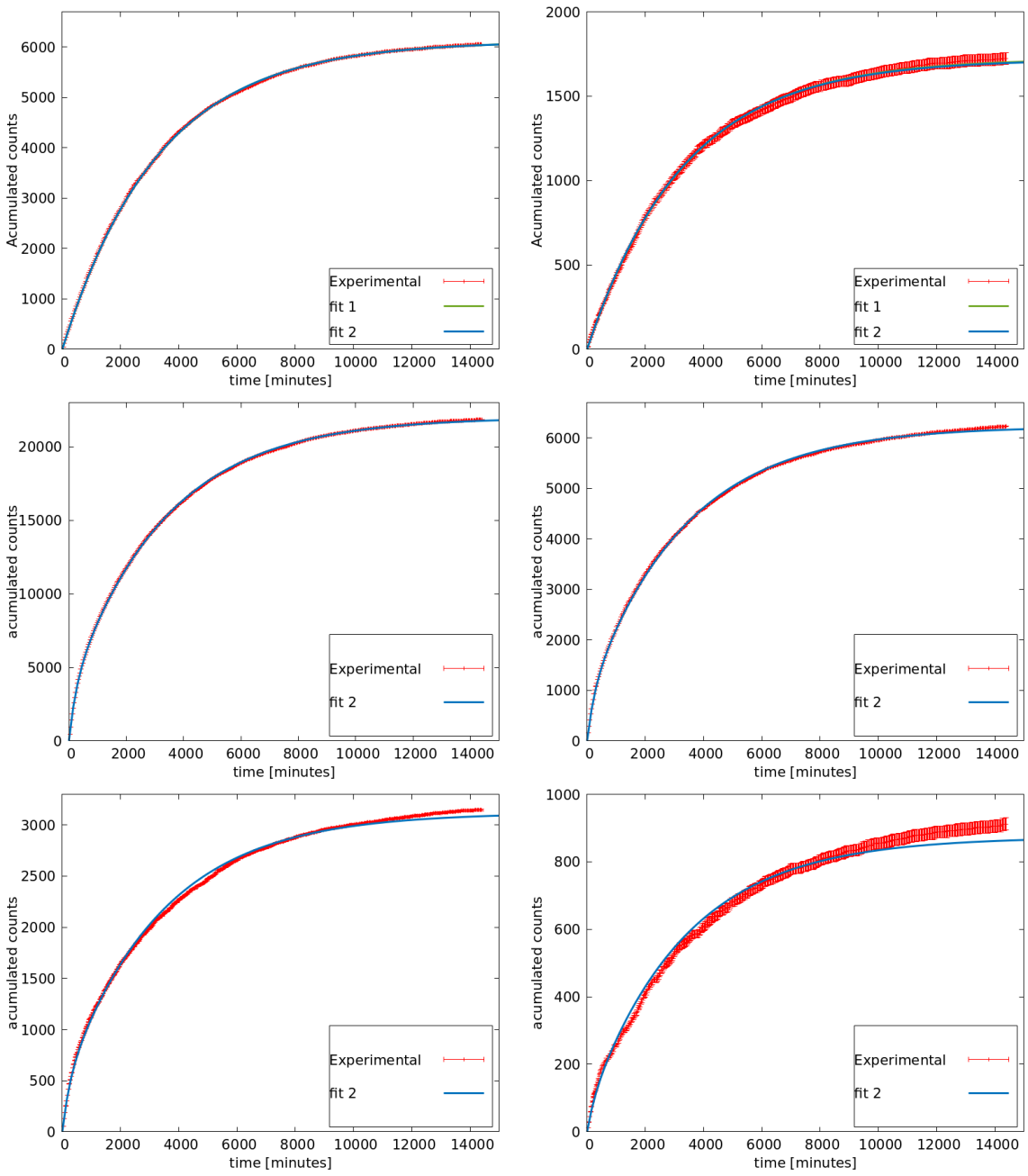

Figure 5.6: Accumulation curves for the second decay acquisition for both x-rays and γ peaks, Top (γ), middle (Kα) and bottom (Kβ_{13}). Plots on the left correspond to acquisitions with the XR-100SDD and on right SXD15M-150-500. The K-lines accumulation curves were fitted using the fixed value of $\lambda(^{117}\text{Sb}) = (4.13 \pm 0.01) \times 10^{-3}$ min^{-1} calculated from table 5.1.

simulations because the target was almost 10 times thinner than now.

In table 5.5, we present the simulated efficiencies used to calculate the ratios shown in n table 5.6.

Table 5.5: Corrected effciencies for the Sn target with copper backing.

Detector	$\epsilon_\gamma \times 10^{-3}$	$\epsilon_{\text{K}\alpha} \times 10^{-3}$	$\epsilon_{\text{K}\beta_{13}} \times 10^{-3}$
XR-100SDD	14 ± 1	12 ± 1	8.9 ± 0.5
SXD15M-150-500	6.5 ± 0.2	5.6 ± 0.2	4.0 ± 0.1

The ratio Kα/γ obtained in both detectors is the same and similar to the value given in literature. For

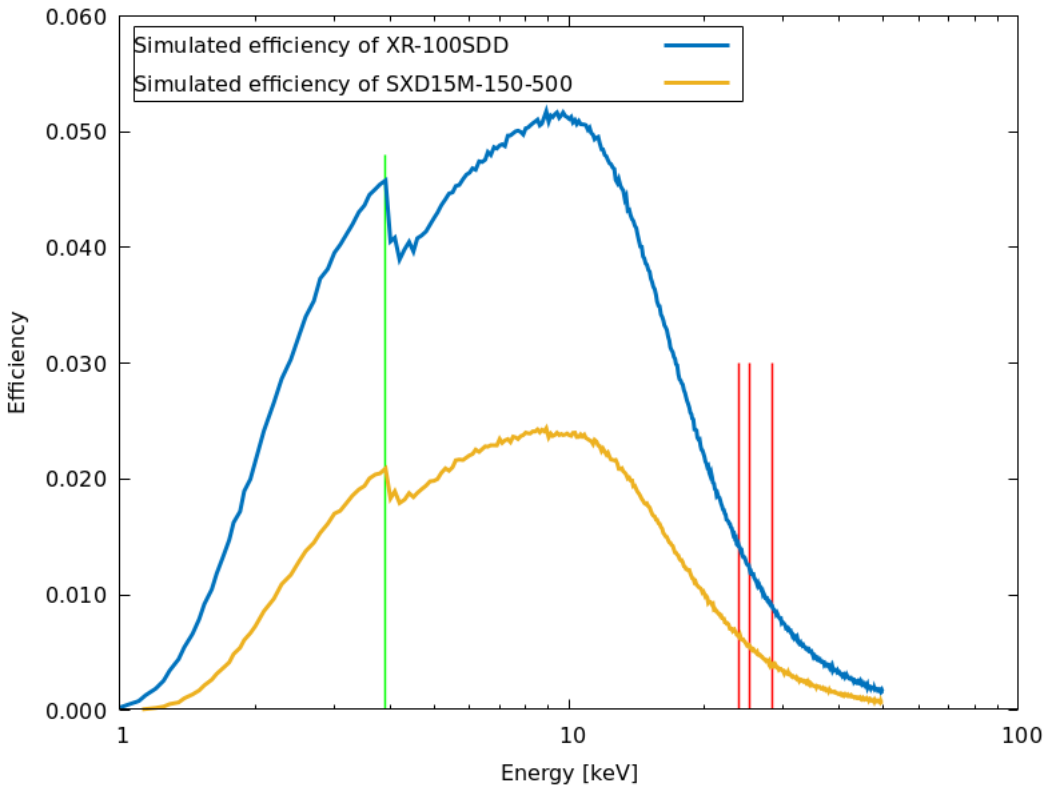

Figure 5.7: Efficiency curve for the detector XR-100SDD (orange) and for the detector SXD15M-150-500 (blue), considering that the source is a cylindrical volume of the target in air. The red vertical lines are positioned at the γ and x-ray energies, and the green line the energy of one of the auger electron emitted in Sn.

Table 5.6: Measured intensity ratios in the second acquisition and comparison with the literature.

	^{119}Sb			^{117}Sb
Source	Kα/γ	Kβ_{13}/γ	Kβ_{13}/Kα	Kβ_{13}/Kα
XR-100SDD	3.6 ± 0.3	0.7 ± 0.1	0.20 ± 0.02	0.18 ± 0.03
SXD15M-150-500	3.6 ± 0.2	0.77 ± 0.05	0.21 ± 0.01	0.10 ± 0.03
Literature	3.6 ± 0.1	0.63 ± 0.05	0.17 ± 0.05	0.20 ± 0.05

the ratios using $N_{peak}^{\mathrm{K}\beta_{13}}$

We see that they differ from the literature, specially for the SXD15M-150-500. This lead us to believe that maybe the intensity given in the literature for the Kβ_{13} x-rays could be incorrect. If we compare the intensities given by [28] and [43], they present different values for the x-ray intensities, which may imply that there is a problem with the literature. The atomic physics code that we used to recreate the experimental data can be used to verify the Kβ_{13}/kα, this study will be done in section 5.1.3. However, we will not be able to verify the relation with the γ, as it is provenient from the decay and not the atomic structure reorganization.

That being said, from this results it's possible to conclude that, in both acquisitions, after removing the contribution from the ^{117}Sb decay we are able to recreate the intensities we see in literature, which means that when using the x-ray yields, in specific the kα x-rays, to calculate the cross-section, we will obtain a value comparable to the one using the γ-ray yield, which was one of the main objectives of this work.

This can clearly be seen if we apply equation 2.13 and calculate N_{decay} for both yields, see table 5.7.

Table 5.7: Table with calculated N_{decays} for both acquisitions, calculated using γ and x-ray yields

E_p [MeV]	3.66		3.29	
Yields	Kα	γ	Kα	γ
$N_D^{irr} \times 10^6$	0.50 ± 0.02	0.50 ± 0.03	2.16 ± 0.09	2.2 ± 0.1

As a final remark of this study, consider that, for the second acquisition we acquired with both detectors, so the counts can be added together, however to do this the efficiency needs to be corrected first. however, the calculated efficiency corrects the counts from the detector solid angle to 4π, which means that we can not simply add the counts as we would be considering double the counts.

5.1.3 Synthetic spectrum simulation

The peaks of γ-emission and Kα lines are relatively well separated. However, to improve our analysis, we implemented an *ab initio* simulation of the detected X-ray emission spectrum. For this, the spectrum of all individual intensities between atomic states of one-hole electron configurations of Sn was used. These intensities were obtained from radiative (X-ray emitting) and radiationless (Auger emitting) transition amplitudes calculated through the atomic structure code MCDFGME [20, 44, 45] that implements the multi-configuration Dirac-Fock method (MCDF). The code computes the atomic wavefunctions by solving the relativistic Hamiltonian, including the lowest-order Breit interaction in the self-consistent method and higher-order Breit terms and QED effects as perturbations.

The transition intensities between two atomic states were obtained by

$$I_{if}^X = \frac{(2J_i+1)}{\sum_{J_i}(2J_i+1)} \cdot \frac{A_{if}^R}{\sum_{f'} A_{if}^R + \sum_{f''} A_{if''}^{NR}}, \tag{5.4}$$

where A_{if}^R is the radiative transition amplitude between an initial one-hole configuration state i and a final one-hole configuration state f, and A_{if}^{NR} is the radiationless transition amplitude between an initial one-hole configuration state i and a final two-holes configuration state f. The full spectrum (all emission lines) involves the calculation of 11784 radiative transition amplitudes and 153312 radiationless transition amplitudes. The factor $2J_i+1$, where J_i is the total angular momentum, accounts for the multiplicity of the initial atomic state. This definition of intensities considers that the initial ionization is statistically distributed among the atomic states. This is not strictly true, as the initial population of electron holes depends on the ionization process and energy (photoionization, electron impact ionization, electron capture, internal conversion, etc.).

Thus, a spectrum with 10325 transitions was generated (see figure 5.8), which was used as a source in the Monte Carlo simulation after binning. A ROOT routine was used in the simulation to randomly sample the energy distribution of the X-ray source, taking the spectrum intensities as probabilities of emission. Obviously, the MCDFGME code does not compute the γ-emission intensity. This was included *ad-hoc* by sampling another photon at the γ-emission energy with 16.5 % probability for each X-ray emitted in the decay of ^{119}Sb.

As mentioned, the intensities obtained with the MCDFGME code do not take into account the different mechanisms for creating the initial atomic holes. In this case, the probabilities of electronic capture and internal conversion (coefficients) for the different atomic shells. For the decay of ^{119}Sb, it was not possible to find in the literature these parameters, but from the tabulated relative intensities, it is possible to estimate the correction weight for the Kα transitions. By summing the intensity of the Kα lines and

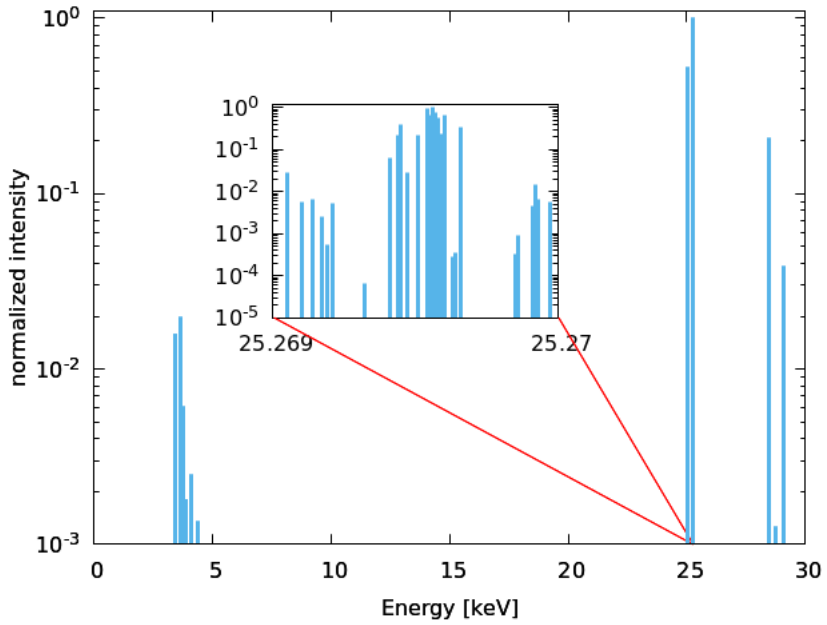

Figure 5.8: Histogram with normalized Sn x-ray emission intensities, showing the K- and L-lines. The insert shows in high-resolution the Kα_1 multiplet.

dividing by the total intensity in table 2.1, one gets $\sim (0.7 \pm 0.1)$ for that correction weight.

The uncorrected simulated spectrum is compared with the measured one in figure 5.9. From this simulation, one gets Kβ_{13}/K$\alpha = (0.207 \pm 0.009)$ which is similar to the value obtained experimentally of Kβ_{13}/K$\alpha = 0.20 \pm 0.02$. Since these lines belong to the same atomic shell, this ratio is independent of the initial ionization mechanism. For the simulated Kα/γ intensity ratio, one gets (4.8 ± 0.4) that, once corrected, gives K$\alpha/\gamma = (0.7 \pm 1) \times (4.8 \pm 0.4) = (3.5 \pm 0.6)$, which is very close to the measured value of K$\alpha/\gamma = 3.6 \pm 0.3$. These results give us confidence that our analysis of the experimental data is correct.

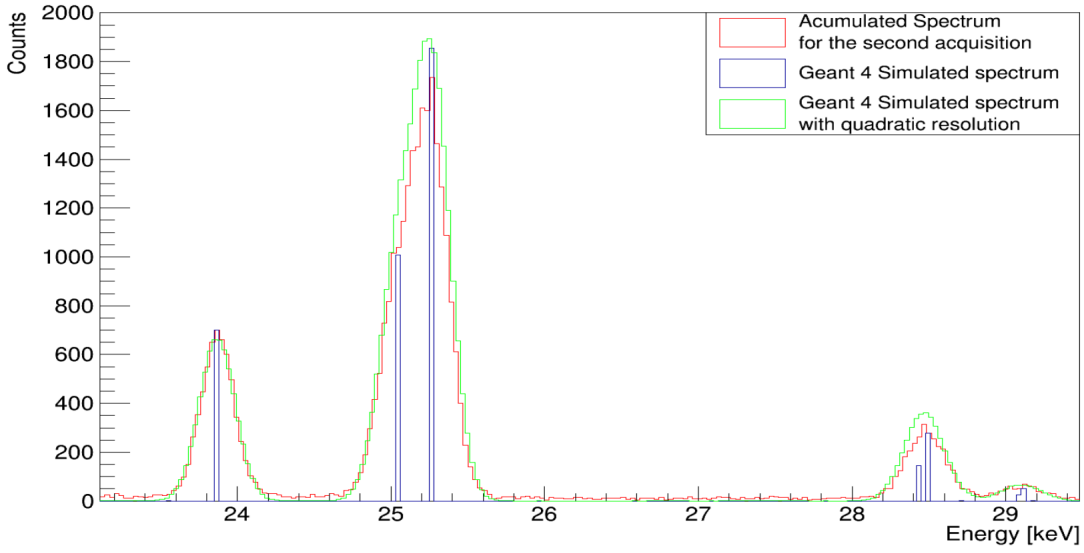

Figure 5.9: Comparison of the simulated and measured ^{119}Sb spectra. The plot shows the binned input spectrum from the MCDFGME calculations (blue) and the simulated spectrum (green) considering the detector's response function without correction weight (see text). The simulated spectrum was normalized to the γ-emission intensity.

5.2 Cross-section calculation

To finalize the study, the reaction cross-section was calculated from the γ-decay and Kα-decay yields of ^{119}Sb obtained in the previous section and from the in-beam RBS analysis.

5.2.1 Absolute method calculation

In section 2.2.3 was shown that the cross section can be obtained from the measured peak area using equation 2.14. This equation assumes a constant flux of protons on the target, however, this was not the case for both irradiations as mentioned in section 4.1.2.

Considering equation 2.9 which is the discrete version of equation 2.8, it is possible to obtain an expression for the cross-section when the flux is not constant. However, that equation presumes that we are able to find a reasonable n that would allow to divide the irradiation in equal intervals of time with constant flux. In the second irradiation this was not the case unless n is taken very large, making the equation and the error propagation complex. This problem can be solved by sequentially applying equation 2.7 for arbitrary time intervals, t_i, to obtain,

$$N_D = \frac{\sigma \cdot N_A}{\lambda} \left[\phi_b^n \left(1 - e^{-\lambda t_n}\right) + \sum_{i=1}^{n-1} \phi_b^i \left(1 - e^{-\lambda t_i}\right) \prod_{j=i+1}^{n} e^{-\lambda t_j} \right], \tag{5.5}$$

From this equation as well as from equations 2.12 and 2.13, the cross-section can be written as:

$$\sigma = \frac{N_{peak} \cdot \lambda \cdot e^{\lambda t_{trans}}}{N_A \cdot \eta \cdot \epsilon_D \left(1 - e^{-\lambda \cdot t_{acqui}}\right)} \left[\phi_b^n \left(1 - e^{-\lambda t_n}\right) + \sum_{i=1}^{n-1} \phi_b^i \left(1 - e^{-\lambda t_i}\right) \prod_{j=i+1}^{n} e^{-\lambda t_j} \right]^{-1} \tag{5.6}$$

This expression allows to use any time interval where the flux is constant, with no restriction on the size of that interval. One interesting study is to compare the cross-sections calculated assuming a mean flux over all irradiation periods and the one obtained considering discrete time intervals with constant flux. In this way, it is possible to understand how important it is to discretize the flux and how it affects the cross-section uncertainty.

The flux values are given in table 4.3 for the $E_p = 3.65$ MeV irradiation and table 4.8 for the $E_p = 3.29$ MeV irradiation. For the latter irradiation, the first interval was considered separately from the mean value, since the flux is very different from the others. Instead, the mean cross-section was calculated with two separated intervals, using equation 5.6, with the first interval corresponding to the much lower flux and the second corresponding to the average flux of the remaining values. Due to the fact that natural tin is being used, the thickness value N_A will be given by $\rho\Delta x_{118Sn} = w_A \cdot \rho\Delta x_{Sn}$ where w_A is the isotropic ratio of ^{118}Sn in natural tin. The values $\rho\Delta x_{Sn}$ for the Al backing and for the Cu backing can be found in sections 4.1.2 and 4.2.3 respectively. The results of the cross-section calculations can be seen in table 5.8.

The ^{118}Sn$(p,\gamma)^{119}$Sb cross-section obtained from the γ and Kα yields are very similar in both irradiations. Additionally, the values in both discrete and constant flux methods are very similar, although the latter seems to have a slightly higher uncertainty. This is not seen for the 3.29 MeV activation.

Table 5.8: Absolute method cross-sections obtained using the constant and discrete flux analysis.

	Reaction	^{118}Sn$(p,\gamma)^{119}$Sb		^{116}Sn$(p,\gamma)^{117}$Sb	
	E_p [MeV]	3.66 ± 0.01	3.29 ± 0.02	3.66 ± 0.01	3.29 ± 0.02
σ [mbarn] mean flux	γ	1.6 ± 0.4	0.28 ± 0.01		
	Kα	1.6 ± 0.4	0.28 ± 0.01	0.9 ± 0.2	0.21 ± 0.02
σ [mbarn] discrete flux	γ	1.6 ± 0.3	0.27 ± 0.01		
	Kα	1.6 ± 0.2	0.27 ± 0.01	0.9 ± 0.2	0.20 ± 0.02

5.2.2 Relative method calculation

The PIPS detectors inside the chamber, shown in figure 4.14, allowed not only for a continuous monitoring of the target. By measuring the backscattered ($\theta_{lab} = 150^o$) protons on the tin nuclei in the target, which are well characterized by the Rutherford cross section, it is possible to derive the (p,γ) reaction cross section independent of the total charge and of the number of atomic nuclei in the target.

Combining equations 2.8, 2.4, and 2.2, one gets

$$\sigma = \left(\frac{d\sigma}{d\Omega}\right)_{Ruth} \frac{4\pi N_D^{irr} \epsilon_p}{1 - e^{-\lambda t}} \frac{\lambda}{w_A r(\theta,\phi)}, \tag{5.7}$$

where the scattered proton rate at the detectors's angular position is given by equation 4.2. Since the Rutherford cross-section does not depend on the mass number, in equation 2.2 N_A will be given by $\rho\Delta x_{Sn}$, however, in equation 2.8 N_A will be given by $\rho\Delta x_{118Sn}$, due to the fact that the (p,γ) reaction can only occur in ^{118}Sn. This makes it that the term w_A appears in equation 5.7. Thus, the proton radiative cross-section for a constant incident flux reads,

$$\sigma = \left(\frac{d\sigma}{d\Omega}\right)_{Ruth} \frac{4\pi N_D^{irr} \epsilon_p}{1 - e^{-\lambda t}} \frac{\lambda t}{w_A N_p} \tag{5.8}$$

This equation shows that, in this approach, the cross-section can be calculated without dependence on the target thickness and on the impinging proton beam flux.

For a discrete flux, the number of scattered protons, N_p^i, can be measured in several time intervals, t_i, of constant flux. Thus, for each interval (see equation 4.3),

$$\phi_b^i = \frac{N_p^i}{4\pi\rho\Delta x_{Sn}\epsilon_p t_i} \cdot \left(\frac{d\sigma}{d\Omega}\right)_{Ruth}^{-1}. \tag{5.9}$$

Substituting this relation in 5.5, one gets for the discrete case,

$$\sigma = \frac{4\pi\epsilon_p N_D^{irr}}{w_A} \cdot \left(\frac{d\sigma}{d\Omega}\right)_{Ruth} \cdot \left[\frac{N_p^n}{\lambda t_n}\left(1 - e^{-\lambda t_n}\right) + \sum_{i=1}^{n-1} \frac{N_p^i}{\lambda t_i}\left(1 - e^{-\lambda t_i}\right) \prod_{j=i+1}^{n} e^{-\lambda t_j}\right]^{-1}. \tag{5.10}$$

Table 5.9 shows the results obtained with the relative method when considering the calculations for discrete time intervals and constant mean flux. For both analysis with the γ-emission and Kα line peaks these differences are negligible. For the $E_p = 3.66$ MeV irradiation, there is a significant difference between the relative and absolute methods. This is expected, since the latter depends on the uncertainties in the target thickness and beam flux that were large for this irradiation. The advantage of the relative method is that these dependencies cancel out. For the $E_p = 3.29$ MeV irradiation, the results from both methods agree between each other. This was expected, since in the absolute method the flux was

calculated from the RBS spectra used in the analysis with the relative method.

Table 5.9: Relative method cross-sections obtained using the discrete and constant mean fluxes analysis.

	Reaction	^{118}Sn$(p,\gamma)^{119}$Sb		^{116}Sn$(p,\gamma)^{117}$Sb	
	E_p [MeV]	3.66 ± 0.01	3.29 ± 0.02	3.66 ± 0.01	3.29 ± 0.02
Cross-section [mbarn] mean flux	γ	1.3 ± 0.1	0.27 ± 0.02		
	Kα	1.31 ± 0.06	0.27 ± 0.01	0.7 ± 0.1	0.21 ± 0.02
Cross-section [mbarn] discrete flux	γ	1.3 ± 0.1	0.27 ± 0.02		
	Kα	1.31 ± 0.08	0.27 ± 0.01	0.7 ± 0.1	0.20 ± 0.01

Figure 5.10 shows the comparison of the ^{118}Sn$(p,\gamma)^{119}$Sb and ^{116}Sn$(p,\gamma)^{117}$Sb reaction cross-sections calculated with the TALYS code, which are of the same order of magnitude of our results. For the latter reaction, the experimental values obtained by N. Özkan et al. [26] and M. Famiano et al. [27] are also shown. Our results agree quite well with them, indicating that they are consistent with these measurements.

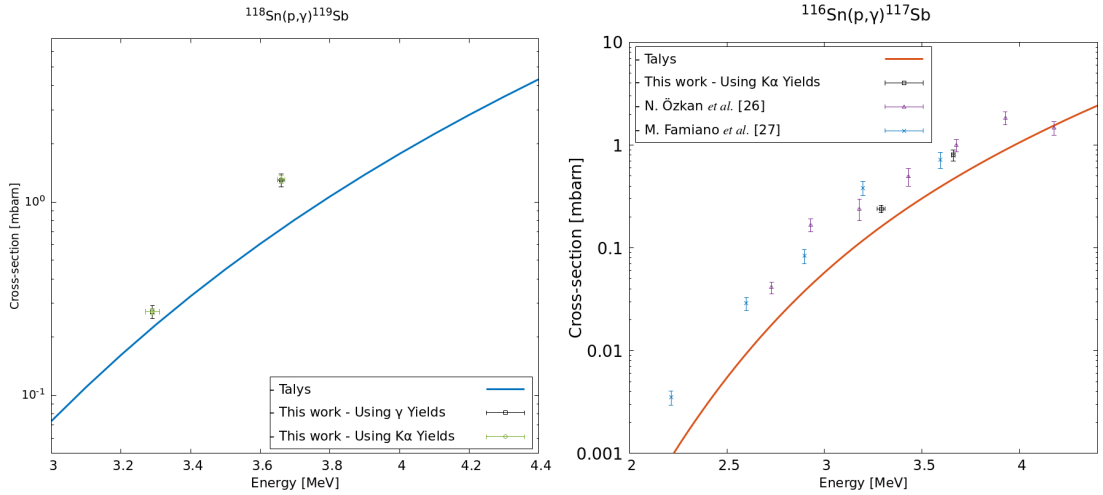

Figure 5.10: Comparison of ^{118}Sn$(p,\gamma)^{119}$Sb (left) and ^{116}Sn$(p,\gamma)^{117}$Sb (right) reaction cross-sections obtained in this work by the Activation Method with calculated cross-sections with the TALYS code. Cross-sections for the ^{116}Sn$(p,\gamma)^{117}$Sb are also compared with data from [26] and [27].

Chapter 6

Conclusions

The main goal of this work was to validate the use of X-ray yields to determine the ^{118}Sn$(p,\gamma)^{119}$Sb reaction cross-section. This was done by comparing the cross-sections obtained from the analysis of the γ-emission and the X-ray K-lines associated to the decay of ^{119}Sb. This validation is very important because in some reactions, the radioactive products only decay via electron capture, without subsequent gamma emission or with a low intensity. In these cases, the measurement of X-ray yields is the only viable way to determine the cross-section through the Activation Method.

Several targets of natural tin of various thicknesses were produced in house with different backings. This study with natural tin was very important to test the methodology to produce in the future works targets with highly enriched ^{118}Sn. Thin targets (of approximately 45 μg/cm^2) were evaporated on an aluminum backing and thicker targets (of approximately 432 μg/cm^2) were evaporated on to a copper backing. By changing the amount of tin in the boat, it was possible to control the thickness. The results are promising, since we were able to produce homogeneous targets of various thicknesses.

The produced targets were characterized with two different methods. Rutherford Backscattering Spectrometry (RBS) provided results with the highest precision. Complementarily, radioactive α sources were used to estimate the target thicknesses via the Energy-Loss Transmission method. With this method, it was not possible to measure thicknesses with high precision, however, it showed some promising results as we were able to measure an energy loss in very thin targets and was essential to understand where improvements were needed.

The thin tin target was activated with a proton beam of 3.66 MeV and the thicker tin target was exposed to a proton beam of 3.29 MeV. In both cases the activation was successful, the beam was stable for about 11 hours, and the target thickness remained constant. However, in the activation at 3.65 MeV, there was a problem with the beam alignment, which decreased the flux arriving at the target. In addition, in the activation with the proton beam at 3.29 MeV, there was a problem with the flux measurement. Some improvements have been made regarding the beam alignment, however, significant work needs to be done to understand and fix the charge collection in the chamber before performing new activations.

The X-rays and photons emitted after the activation were measured by two SDD detectors, placed in close geometry. The response functions of the detectors were fully characterized by means of Monte Carlo simulations, and the data acquisition and analysis was fully automatized. The main improvement needed to be done is in the target positioning, which will be done in the future with the construction of a support that allows a closer control of the geometry throughout all acquisitions.

The use of natural tin produced interesting results, some of them that we were not expecting. For instance, the accumulated spectra exhibits not only the K-lines analysed in this work, but also the Lα and Lβ lines of tin. The lines are very well defined, since they are positioned at an energy where the detector

has a higher efficiency and sufficient resolution, making it an interesting study to do in the future. The analysis of the X-ray spectrum can be supported by detailed theoretical calculations of the emission lines intensities. In this work, we presented an emission spectrum of the Sn K-lines from MCDF method calculations. In future works, we intend to extend these calculations to the L-lines, taking into account the electron capture probabilities and internal conversion coefficients for the different atomic shell in the ^{119}Sb decay.

The contribution of ^{117}Sb, produced in the proton capture reaction on ^{116}Sn, was deconvoluted from the reaction of interest in the accumulated spectra. This resulted in Kα/γ intensity ratios from the decay of ^{119}Sb of 3.6 ± 0.3 (at both proton beam energies), which is in agreement with the literature value of 3.6 ± 0.1.

The cross-sections for both ^{118}Sn$(p,\gamma)^{119}$Sb and ^{116}Sn$(p,\gamma)^{117}$Sb reactions were calculated using two methods: the absolute method and the relative method. In the absolute method, it is necessary to know precisely the incident proton flux and the target thickness, while in the relative method, the number of backscattered protons was measured, eliminating the dependence on these two parameters.

In the absolute method, the difference between the cross-sections obtained using the Kα-line and the γ-emission yields was negligible for both analysis, obtaining, respectively, 1.6 ± 0.3 mbarn and 1.6 ± 0.2 mbarn at E$_p$ = 3.66 MeV , and 0.27 ± 0.01 mbarn and 0.27 ± 0.01 mbarn at E$_p$ = 3.29 MeV. For the ^{116}Sn$(p,\gamma)^{117}$Sb reaction, the Kα-line intensity was measured, from which the cross-sections of 0.9 ± 0.2 mbarn at E$_p$ = 3.66 MeV and 0.20 ± 0.02 mbarn at E$_p$ = 3.29 MeV were calculated. The results using a mean constant incident flux of protons, give similar values with larger uncertainties than the ones calculated for the discrete flux observed experimentally.

Applying the relative method, the cross-sections obtained from Kα-line and the γ-emission yields also gave negligible differences as well as between the discrete and constant mean flux calculations. However, there is a difference of about 16-18 % between the calculated values with absolute and relative methods at 3.66 MeV. This difference can be justified by the fact that the relative method cancels out any dependencies in the incident proton flux and thickness. These two parameters were particularly affected by measurement uncertainties at this energy.

The cross-section values obtained using either methods are in the same order of magnitude as the ones given by TALYS code calculations. Furthermore, the ^{116}Sn$(p,\gamma)^{117}$Sb reaction cross-sections obtained trough the relative method are in good agreement with the experimental values obtained by N. Özkan et al. [26] and M. Famiano et al. [27].

These results show that the relative method is more robust to errors in the flux and thickness measurements, resulting in lower uncertainties than the absolute method. The absolute and relative methods are not exclusive, since it is always possible to apply both methods in the same irradiation as long as the in-beam RBS spectra are measured.

The next steps in this work should be to activate an highly enriched target of ^{118}Sn. In this study, several improvements were already proposed, namely, correcting the charge collection inside the reaction chamber, the production of a support for the activated target during the acquisition of the decay, and improve the thickness measurement system by energy loss in the target. Target activation should also be performed for more energy points in order to extract the energy dependence of the cross-section and the corresponding astrophysical S-factor.

References

[1] G. Wallerstein *et al.*, "Synthesis of the elements in stars: forty years of progress," *Rev. Mod. Phys.*, vol. 69, no. 4, p. 995, 1997.

[2] A. G. W. Cameron, "Nuclear reactions in stars and nucleogenesis," *Publ. Astron. Soc. Pac.*, vol. 69, no. 408, pp. 201–222, 1957.

[3] E. M. Burbidge *et al.*, "Synthesis of the elements in stars," *Rev. Mod. Phys.*, vol. 29, no. 4, p. 547, 1957.

[4] M. Arnould and S. Goriely, "The p-process of stellar nucleosynthesis: astrophysics and nuclear physics status," *Phys Rep*, vol. 384, no. 1-2, pp. 1–84, 2003.

[5] C. Travaglio, F. Röpke, R. Gallino, and W. Hillebrandt, "Type ia supernovae as sites of the p-process: two-dimensional models coupled to nucleosynthesis," *Astrophys. J.*, vol. 739, no. 2, p. 93, 2011.

[6] H. Schatz *et al.*, "End point of the rp process on accreting neutron stars," *Phys. Rev. Letters*, vol. 86, no. 16, p. 3471, 2001.

[7] C. Fröhlich *et al.*, "Neutrino-induced nucleosynthesis of A> 64 nuclei: the ν p process," *Phys. Rev. Letters*, vol. 96, no. 14, p. 142502, 2006.

[8] F. K. Thielemann *et al.*, "Neutron star mergers and nucleosynthesis of heavy elements," *Annu. Rev. Nucl. Part. S.*, vol. 67, pp. 253–274, 2017.

[9] W. Rapp *et al.*, "Sensitivity of p-process nucleosynthesis to nuclear reaction rates in a 25 M_{Solar} supernova model," *The AstroPhys. J.*, vol. 653, no. 1, p. 474, 2006.

[10] M. Aliotta *et al.*, "Storage ring at HIE-ISOLDE: Technical design report," *Eur. Phys. J. Spec. Top.*, vol. 207, no. CERN-INTC-2012-027, pp. 1–117, 2012.

[11] N. Özkan *et al.*, "Astrophysical S factor for α-capture on Sn 112 in the p-process energy range," *Phys. Rev. C*, vol. 75, no. 2, p. 025801, 2007.

[12] D. E. Khulelidze *et al.*, "Excitation functions of the (α, γ) and (α, n) reactions of tin isotopes," *Sov. Phys., JETP-USSR*, vol. 20, p. 259, 1965.

[13] F. Chloupek *et al.*, "Measurements of proton radiative capture cross sections relevant to the astrophysical rp-and γ-processes," *Nucl. Phys. A*, vol. 652, no. 4, pp. 391–405, 1999.

[14] Atomic Mass Data Center, *[Online] Available:* `http://amdc.impcas.ac.cn/`, accessed in february, 2020.

[15] G. G. Kiss *et al.*, "Determining reaction cross sections via characteristic x-ray detection: α-induced reactions on ^{169}Tm for the astrophysical γ-process," *Phys. Lett. B*, vol. 695, no. 5, pp. 419–423, 2011.

[16] G. G. Kiss *et al.*, "Ge 70 (p, γ) As 71 and Ge 76 (p, n) As 76 cross sections for the astrophysical p process: Sensitivity of the optical proton potential at low energies," *Phys. Rev. C*, vol. 76, no. 5, p. 055807, 2007.

[17] S. A. et al., "Geant4—a simulation toolkit," *Nucl. Instrum. Meth. A*, vol. 506, no. 3, pp. 250 – 303, 2003.

[18] J. Allison and et al., "Geant4 developments and applications," *IEEE T. on Nucl. Sci.*, vol. 53, no. 1, pp. 270–278, 2006.

[19] J. Allison and et al., "Recent developments in geant4," *Nucl. Instrum. Meth. A*, vol. 835, pp. 186 – 225, 2016.

[20] J. P. Desclaux, "A multiconfiguration relativistic DIRAC-FOCK program," *Comput. Phys. Commun.*, vol. 9, pp. 31–45, jan 1975.

[21] K. S. Krane, D. Halliday, *et al.* Introductory nuclear physics. New York: John Wiley & Sons, 1987.

[22] A. Di Leva *et al.*, "Underground study of the ^{17}O(p, γ) ^{18}F reaction relevant for explosive hydrogen burning," *Phys. Rev. C*, vol. 89, no. 1, p. 015803, 2014.

[23] D. A. Hutcheon *et al.*, "The DRAGON facility for nuclear astrophysics at TRIUMF-ISAC: design, construction and operation," *Nucl. Instrum. A*, vol. 498, no. 1-3, pp. 190–210, 2003.

[24] G. Gyürky, Z. Fülöp, F. Käppeler, G. Kiss, and A. Wallner, "The activation method for cross section measurements in nuclear astrophysics," *Eur Phys J A*, vol. 55, no. 3, pp. 1–31, 2019.

[25] M. J. Berger, J. S. Coursey, M. A. Zucker, and J. Chang, "ESTAR, PSTAR, and ASTAR: Computer programs for calculating stopping-power and range tables for electrons, protons, and helium ions (version 1.2.3)," *[Online] Available: `http://physics.nist.gov/Star` accessed in february, 2020.*

[26] N. Özkan *et al.*, "Cross section measurements of the ^{102}Pd (p,γ)^{103}Ag, ^{116}Sn(p, γ) ^{117}Sb, and ^{112}Sn(α,γ)^{116}Te reactions relevant to the astrophysical rp-and γ-processes," *Nucl. Phys. A*, vol. 710, no. 3-4, pp. 469–485, 2002.

[27] M. A. Famiano *et al.*, "Measurement of the (p, γ) cross sections of ^{46}Ti, ^{64}Zn, ^{114}Sn, and ^{116}Sn at astrophysically relevant energies," *Nucl. Phys. A*, vol. 802, no. 1-4, pp. 26–44, 2008.

[28] National Nuclear Data Center, Chart of Nuclides, *[Online] Available: `https://www.nndc.bnl.gov/nudat2/`*, accessed in february, 2020.

[29] Amptek, *Silicon Drift Detector (SDD) XR-100SDD/ X-123SDD [online] available:`https://www.amptek.com/-/media/ametekamptek/documents/products/xr-100sdd-silicon-drift-detector-sdd-specifications.pdf?dmc=1&la=en&revision=118878c2-f716-4b16-a744-1ce91094b2b0`*, accessed in Jan 2020.

[30] Mirion Technologies, *SXD15M-150-500 X-PIPS^{TM} Detector (SDD) [online] available: https://mirion.s3.amazonaws.com/cms4_mirion/files/pdf/spec-sheets/sxd15m-150-500-x-pips-detector-sdd.pdf?1588005724*, accessed in Jan 2020.

[31] Amptek *[Online] Available: https://www.amptek.com/, accessed in Jan. 2020.*

[32] U. Fano, "Ionization yield of radiations. ii. the fluctuations of the number of ions," *Phys. Rev.*, vol. 72, no. 1, p. 26, 1947.

[33] Kurt J. Lesker Company, *Material Deposition Chart [Online] Available: https://www.lesker.com/newweb/deposition_materials/materialdepositionchart.cfm?pgid=0#t*, accessed in June, 2020.

[34] L. Yaffe, "Preparation of thin films, sources, and targets," *Annual review of nuclear science*, vol. 12, no. 1, pp. 153–188, 1962.

[35] MAX-PLANCK-INSTITUT FÜR PLASMAPHYSIK GARCHING BEI MÜNCHEN, *SIMNRA User's Guide*, April 1997.

[36] M. Mayer, "SIMNRA, a simulation program for the analysis of NRA, RBS and ERDA," in *AIP Conf. Proc.*, vol. 475, pp. 541–544, American Institute of Physics, 1999.

[37] M. Chiari, L. Giuntini, P. Mando, and N. Taccetti, "Proton elastic scattering cross-section on aluminium from 0.8 to 3 mev," *Nucl. Instrum. Meth. B*, vol. 174, no. 3, pp. 259–266, 2001.

[38] CTN/IST *[Online] Available: http://www.ctn.tecnico.ulisboa.pt/facilities/pt_lab_ion_beam.htm, accessed in Nov. 2020.*

[39] H. Silva, "Elastic scattering of protons and oxygen ions from light nuclei," Ph.D. dissertation, FCT/UNL, Lisbon, 2018. accessed july, 2020. [online], avaiable: https://run.unl.pt/handle/10362/57403.

[40] A. Koning, D. Rochman, J.-C. Sublet, N. Dzysiuk, M. Fleming, and S. Van Der Marck, "TENDL: complete nuclear data library for innovative nuclear science and technology," *Nucl. Data Sheets*, vol. 155, pp. 1–55, 2019.

[41] A. J. Koning and D. Rochman, "Modern nuclear data evaluation with the TALYS code system," *Nucl. Data Sheets*, vol. 113, no. 12, pp. 2841–2934, 2012.

[42] M. J. Berger, J. H. Hubbell, S. M. Seltzer, J. Chang, J. S. Coursey, R. Sukumar, D. S. Zucker, and K. Olsen, "XCOM: Photon cross section database (version 1.5)," *[Online] Available: http://physics.nist.gov/xcom accessed in february, 2020.*

[43] S. Y. F. Chu, L. P. Ekström, and R. B. Firestone, "Table of radioactive isotopes, ^{119}Sb decay radiation," *[Online] Available: http://nucleardata.nuclear.lu.se/toi/nuclide.asp?iZA=510119 accessed in february, 2020.*

[44] P. Indelicato and J. P. Desclaux, "Multiconfiguration Dirac-Fock calculations of transition energies with QED corrections in three-electron ions," *Phys. Rev. A*, vol. 42, pp. 5139–5149, nov 1990.

[45] P. Indelicato, "Projection operators in multiconfiguration dirac-fock calculations: Application to the ground state of heliumlike ions," *Phys. Rev. A*, vol. 51, pp. 1132–1145, Feb 1995.